THESIS FOR THE DEGREE OF DOCTOR OF PHILOSOPHY

Operando Analysis of Materials and Processes in Next Generation Batteries

Analytical Methods Revealing the Operating Mechanisms of Next Generation Battery Chemistries

Matthew J. Sadd

Department of Physics

CHALMERS UNIVERSITY OF TECHNOLOGY

Gothenburg, Sweden 2021

Operando Analysis of Materials and Processes in Next Generation Batteries
Analytical Methods Revealing the Operating Mechanisms of Next Generation Battery Chemistries
Matthew J. Sadd
ISBN 978-91-7905-608-7

Doktorsavhandlingar vid Chalmers tekniska högskola
Ny serie nr 5074
ISSN 0346-718X

Department of Physics
Chalmers University of Technology
SE-412 96 Gothenburg
Sweden
Telephone + 46 (0)31-772 1000

Chalmers Reproservice
Gothenburg, Sweden 2021

Abstract

With the rise in popularity of electric vehicles and electromobility solutions, there is a higher demand for high energy density batteries. Accompanying this increased demand, there is also increased pressure for lower costs, longer durability, and the use of more sustainable materials. Going beyond the constraints imposed by the Li-ion battery, Next Generation Batteries, encompassing a host of technologies and chemistries, have the potential to provide higher energy densities while using more sustainable materials and at a lower cost.

When exploring Next Generation Battery technologies, novel materials and complex reactions are introduced, underpinning the working mechanisms of energy storage. A clear understanding of materials and processes during operation needs to be established to move these technologies closer to realisation. To achieve this goal, investigations using *operando* characterisation techniques, measurements made during battery charge and discharge, provide a unique tool to advance the understanding of how a given battery technology works.

This thesis explores the use of *operando* analysis methods to reveal the inner workings of three key next generation battery technologies; Na-ion anodes and how the electrode structure can be tuned to facilitate Na^+ intercalation, how Lithium-Sulfur cathodes evolve during cell cycling and the subsequent conversion of polysulfide species, and finally the structures observed when using Lithium-metal as an anode for high-capacity batteries. The focus is to determine structural changes to electrode materials using X-ray Tomographic Microscopy and chemical changes using Raman Spectroscopy to reveal mechanisms controlling the performance in terms of capacity, rate capability or cycling stability. Though *operando* measurements present an exciting opportunity to monitor real-time processes, they need to be grounded in reality. Thus this thesis explores supporting work, such as *ex situ* measurements, electrochemical evaluations, and traditional characterisation methods used in battery research, all used to determine the complex and dynamic processes that dictate how batteries perform.

List of Papers

I Real-time imaging of Na^+ reversible intercalation in "Janus" graphene stacks for battery applications

J. Sun, M. Sadd, P. Edenborg, H. Grönbeck, P.H. Thiesen, Z. Xia, V. Quintano, R. Qiu, A. Matic and V. Palermo
Science Advances 7 (2021) 1–12 https://doi.org/10.1126/sciadv.abf0812.

II Rational Design of Low Cost and High Energy Lithium Batteries through Tailored Fluorine-free Electrolyte and Nanostructured S/C Composite

M. Agostini, D.H. Lim, M. Sadd, J.Y. Hwang, S. Brutti, J.W. Heo, J.H. Ahn, Y.K. Sun and A. Matic,
ChemSusChem 11 (2018) 2981–2986. https://doi.org/10.1002/cssc.201801017.

III Polysulfide Speciation and Migration in Catholyte Lithium-Sulfur Cells

M. Sadd, M. Agostini, S. Xiong, and A. Matic
Accepted ChemPhysChem.

IV Diffusion Limited Dissolution-Precipitation Processes in Lithium-Sulfur Cells

M. Sadd, S. De Angelis, S. Colding-Jørgensen, D. Blanchard, R. Johnsen, S. Sanna, E. Borisova, A. Matic and J. Bowen,
Under Review

V Designing a Safe Electrolyte Enabling Long-Life Li/S Batteries

M. Agostini, M. Sadd, S. Xiong, C. Cavallo, J. Heo, J.H. Ahn, and A. Matic
ChemSusChem 12 (2019) 4176-4184. https://doi.org/10.1002/cssc.201901770.

VI Insight into the Critical Role of Exchange Current Density on Electrodeposition Behavior of Lithium Metal

Y. Liu, X. Xu, M. Sadd, O.O. Kapitanova, V.A. Krivchenko, J. Ban, J. Wang, X. Jiao, Z. Song, J. Song, S. Xiong, and A. Matic
Advanced Science 2003301 (2021) 1–11. https://doi.org/10.1002/advs.202003301

VII Visualizing microstructure evolution of lithium plating and stripping by operando X-ray tomographic microscopy

M. Sadd, S. Xiong, J. Bowen, F. Marone and A. Matic
manuscript

Papers Not Included in the Thesis

I Stabilizing the Performance of High-Capacity Sulfur Composite Electrodes by a New Gel Polymer Electrolyte Configuration

M. Agostini, D.H. Lim, M. Sadd, C. Fasciani, M.A. Navarra, S. Panero, S. Brutti, A. Matic, B. Scrosati
ChemSusChem. 10 (2017) 3490–3496. https://doi.org/10.1002/cssc.201700977.

II Enhanced ionic conductivity and interface stability of hybrid solid-state polymer electrolyte for rechargeable lithium metal batteries

Q. Liu, Y. Liu, X. Jiao, Z. Song, M. Sadd, X. Xu, A. Matic, S. Xiong, J. Song
Energy Storage Mater. 23 (2019) 105–111. https://doi.org/10.1016/j.ensm.2019.05.023.

III Enhancement of Functional Properties of Liquid Electrolytes for Lithium-Ion Batteries by Addition of Pyrrolidinium-Based Ionic Liquids with Long Alkyl-Chains

A. Celeste, L. Silvestri, M. Agostini, M. Sadd, S. Palumbo, J.K. Panda, A. Matic, V. Pellegrini, S. Brutti
Batteries and Supercaps. 3 (2020) 1059–1068. https://doi.org/10.1002/batt.202000070.

IV Effect of the Niobium Doping Concentration on the Charge Storage Mechanism of Mesoporous Anatase Beads as an Anode for High-Rate Li-Ion Batteries

C. Cavallo, G. Calcagno, R.P. De Carvalho, M. Sadd, B. Gonano, C.M. Araujo, A.E.C. Palmqvist, A. Matic
ACS Appl. Energy Mater. (2021). https://doi.org/10.1021/acsaem.0c02157.

V Review - Reference Electrodes in Li-Ion and Next Generation Batteries: Correct Potential Assessment

E.C. Cengiz, J. Rizell, M. Sadd, A. Matic, N. Mozhzhukhina
J. Electrochem. Soc. (2021). https://doi.org/10.1149/1945-7111/ac429b.

Contribution Report

I Real-time imaging of Na+ reversible intercalation in “Janus” graphene stacks for battery applications

- I designed the *operando* experiment, determining how to configure the commercial EL-cell to be used for Raman and ellipsometry measurements on the novel 8-layer ‘Janus’ graphene. I performed *operando* Raman analysis on all materials discussed in the paper, treating, and interpreting both the Raman and complementing electrochemical data. I discussed and assisted in the preparation of the manuscript, and subsequent responses to reviewers.

II Rational Design of Low Cost and High Energy Lithium Batteries through Tailored Fluorine-free Electrolyte and Nanostructured S/C Composite

- I assisted with electrochemical experiments and analysis of materials in the paper, and jointly discussed and worked on the synthesis of the results and writing of the manuscript.

III Polysulfide Migration and Conversion in Catholyte Lithium-Sulfur Cells

- I prepared all materials, performed the *operando* Raman analysis, performed all electrochemical analysis, discussed results with co-authors, and wrote the original manuscript and subsequent finalisation.

IV Diffusion Limited Dissolution-Precipitation Processes in Lithium-Sulfur Cells

- I proposed and prepared materials for the experiment, from slurry to be used in the *operando* cell, to preparing *ex situ* samples. I was involved in the synchrotron experiment and discussed with the authors various forms of data analysis to be performed on the synchrotron tomography data. I discussed and synthesised the results with co-authors and prepared the original manuscript and subsequent finalisation.

V Designing a Safe Electrolyte Enabling Long-Life Li/S batteries

- I prepared the electrolytes, performed Raman analysis, assisted with conductivity, viscosity, electrochemical analysis, discussion, and preparation of the manuscript. I authored the section on Raman analysis.

VI Insight into the Critical Role of Exchange Current Density on Electrodeposition Behavior of Lithium Metal

- I assisted with the preparation of electrolytes and performed density, viscosity, and conductivity experiments to provide the input data needed for the phase field modelling. I discussed the theory and implications/conclusions from the modelling and the took part in writing the manuscript with co-authors of the paper.

VII Visualizing microstructure evolution of lithium plating and stripping by operando X-ray tomographic microscopy

- I proposed and prepared materials for the experiment, designed and prepared the *operando* cells. I planned and led the synchrotron experiment and performed all data analysis on the synchrotron tomography data. I discussed results with co-authors and prepared the original manuscript and subsequent finalisation.

Table of Contents

1 Introduction

Batteries surround us, powering our phones and laptops, and are becoming ever more prevalent in the electrification of the transport sector. A decade ago, only seven mass-market electric vehicles existed from manufacturers such as Nissan and Renault. Today, there are over 50 different electric car models available worldwide, from major car manufacturers such as Ford, BMW, and Audi, just to name a few. However, electrification efforts do not end at electric passenger cars; as the transport sector pushes to become ever greener, a range of electric buses, trucks and even electric planes are under development. This plethora of electric technologies all need one major component, a way to store electric energy efficiently, which batteries can provide.

However, as we see the widespread adoption of batteries in electric vehicles, several challenges need to be addressed: the battery's cost, specific energy, materials supply, and chemistry sustainability. While there are technological alternatives to batteries, such as hydrogen fuel cells and supercapacitors, such alternative technologies also have their flaws. Analysis from Volkswagen says that the well-to-wheel efficiency for battery electric vehicles (BEVS) is between 70-90%, while the well-to-wheel efficiency for fuel cell vehicles (FCVs) is 25-35%.[1] The ability to aid a transition to greener transport, the increased well-to-wheel efficiency, and the ever-increasing specific energy of batteries place them as the dominant technology.

The current gold standard of secondary batteries is the Li-ion battery, first commercialised by Sony in 1991.[2] "Li-ion" itself is an umbrella term representing a range of cathode and anode chemistries, all relying on the 'rocking chair' mechanism with Li^+ moving between the anode and cathode where they are inserted and intercalated into the active electrode materials.[3] In the three decades since Li-ion was first commercialised, the price per cell has decreased by over 97%, while the specific energy has increased from 80 Wh kg^{-1} to 250 Wh kg^{-1}.[4] This progress stems from continuous research and development, with chemical changes to increase voltage and capacity, and persistent engineering changing the design and internal structure of batteries.

As more technologies emerge requiring electric energy storage, we will see an increased demand for batteries and increased demand for the raw materials needed for production. Presently, such materials are already under the spotlight, with companies that produce batteries

coming under international scrutiny due to the use of cobalt. Moving into the future, an increase in the available energy density of batteries is required, while simultaneously, we must ensure the utilisation of sustainable materials to meet these requirements. We need to look towards new technologies.

One path forward in increasing energy density is to change the electrochemical processes that underpin how energy is stored. Such changes to the battery chemistries could result in much higher theoretical specific energies, meaning batteries can be made lighter, made from fewer materials, and potentially made at a lower cost. These Next Generation Battery (NGB) technologies [5] can use different alkali or alkali earth ions, such as is the case with Na-ion batteries, promising a far more sustainable technology. Alternatively, chemistries that continue to use Li with a change to the electrochemical processes, such as Li-sulfur and Li-metal, hold the promise of a nearly 10-fold increase in theoretical specific energy, based on the weight of active materials.

However, these NGBs, like any new technology, are plagued with obstacles towards practical realisation, and the knowledge base surrounding their operation is still developing. Since Li-ion has been in the spotlight for over 30 years, a considerable knowledge base has been built up around the technology, providing information on the use of tuned electrolytes,[6] the effect of cycling on the electrode structure,[7] intimate understanding of the electrochemical reactions at each electrode, and how Li^+ interacts with the materials. This in-depth understanding has led to the Li-ion's meteoric rise and development. To put NGBs on the same path, we need novel and comprehensive forms of analysis to push progress in their discovery and utilisation by exploring physical and chemical processes inside the battery.

These physical and chemical changes to the materials used in NGBs have a pivotal role on their performance. This thesis addresses the challenges associated with the materials and processes used in selecting NGBs and how we can study them. In the case of Na-ion batteries, which can provide a sustainable alternative to Li-ion, Na^+ cannot intercalate into graphite, the hallmark anode material of the Li-ion technology. However, tailoring graphitic structures can enable efficient storage of Na^+, yet the interaction between ions and material needs to be understood to develop tailored approaches further. Moving to conversion chemistry to reach higher capacities, a system investigated is the Li-sulfur batter. However, the dissolution, migration, and precipitation of polysulfide species during cycling has hindered the system from realising

its full potential. A lack of understanding surrounds the conversion, interaction, and mobility of polysulfides inside the battery limits the ability to develop the technology. Furthermore, the sulfur cathode must be combined with a high-capacity anode where Li-metal would be the electrode of choice to achieve high-capacity batteries. Instead of the reversible intercalation of Li^+ into the graphite, Li-metal anodes rely on stripping and plating of Li from the electrode surface. This process must be reversible, form dense and homogenous microstructures, with acute attention paid to the interaction between Li-metal and the electrolyte used.

To understand these complex interactions, analytical methods must be used to probe the materials and processes to build a deeper understanding of the physical and chemical interactions inside NGBs. This thesis addresses *operando* methodologies to investigate battery processes during operation. From a multitude of technologies that can be used, Raman spectroscopy and X-ray tomographic microscopy proved to be ideal methods to analyse the selected NGB materials. Raman spectroscopy provides detailed chemical information by providing insights into the interaction between graphitic materials and Na^+ and monitoring the evolution of chemical species present in a battery's electrolyte. While x-ray tomographic microscopy can follow physical changes to electrode morphologies in real time. With high resolution imaging, changes to electrode structures have been shown and quantitively compared to battery performance.

2 Batteries

2.1 History and Explanation of Cell Components

A battery is a device that can store energy electrochemically; this means that energy is stored as electrochemical reactions. This energy can then be delivered in the form of electricity when the battery discharges, and conversely, electricity can be used to recharge the battery. Typically, a battery consists of multiple electrochemical cells placed in parallel to one another to increase capacity or held in series to increase voltage. The word's history can be traced back to 18th Century North America and Benjamin Franklin, where 'battery' was used to describe a grouping of Leyden Jars, an early form of capacitor. He took his inspiration from artillery, where a battery described a grouping of cannons working together. For this thesis, the word battery will describe a single electrochemical cell, consisting of only one anode and one cathode. However, the word battery is used today covers various technologies, each suited to a given purpose.

Alessandro Volta is credited with inventing the first electrochemical battery in the 19th century. This battery, known as the voltaic pile,[8] relied on zinc and copper plates separated by brine-soaked paper sheets (Figure 1), and this combination of materials provided a small current. These core components we now know as the anode, cathode, electrolyte, and separator. We refer to their combination as a galvanic cell, capable of producing current through spontaneous reduction/oxidation (redox) reactions. We also refer to this configuration of the anode and cathode as a full cell, where the properties of the battery are the combined result of the processes at both electrodes.

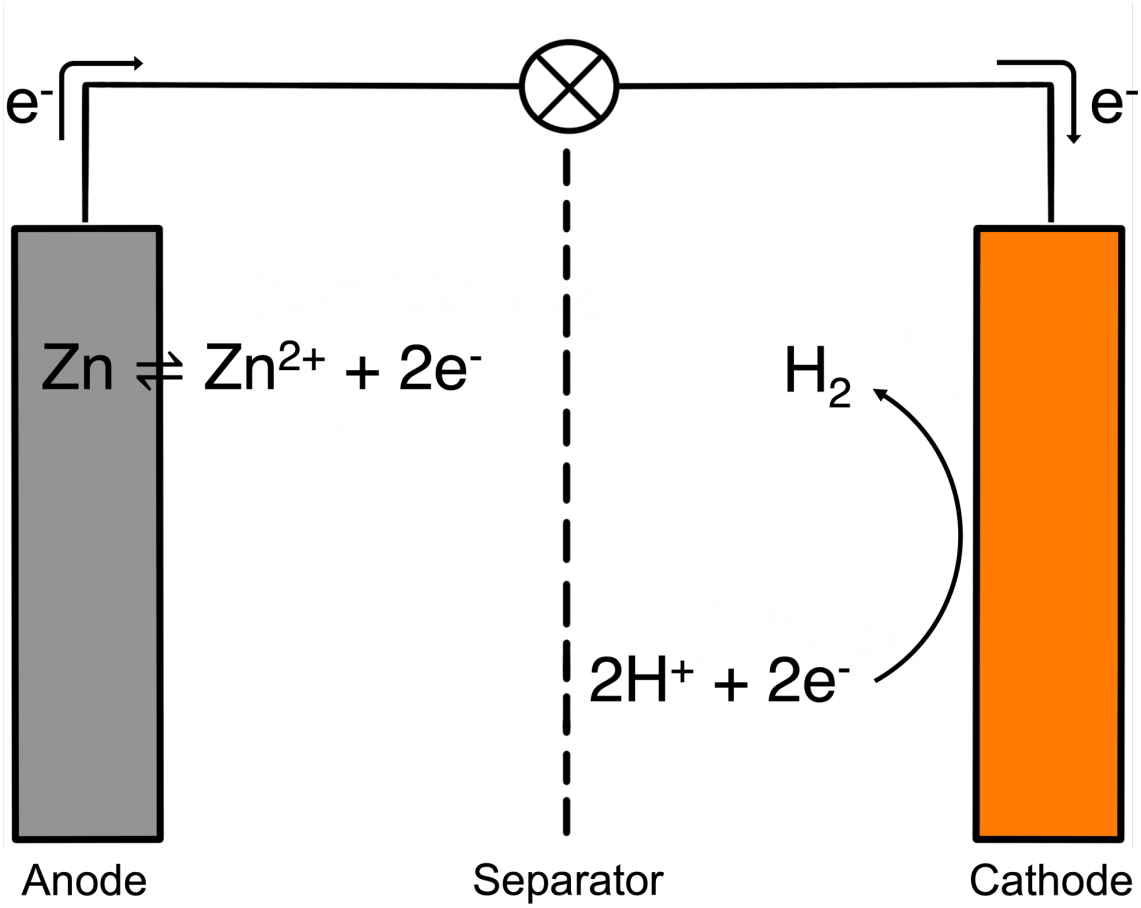

Figure 1 Schematic of cell components of the Volta pile and reactions during discharge. On the left is a zinc anode with oxidation during discharge, and on the right is the copper cathode with reduction during discharge.

The anode in the Volta pile was made of zinc metal. During the discharge of the cell, the zinc is oxidised, thereby losing 2 electrons. The generated zinc ion enters the electrolyte, while the 2 electrons travel to the cathode via the external electric circuit.

Oxidation $$Zn \rightleftharpoons Zn^{2+} + 2e^{-} \quad (1)$$

The cathode was copper, Cu, however during the discharge of the voltaic pile, hydrogen gas was formed at the copper surface. In this case, hydrogen ions from the brine/electrolyte gain electrons from the external circuit and are reduced to hydrogen gas. Here copper itself is not formally oxidised or reduced but instead acts as a surface for the hydrogen ions to interact with and gain electrons.

Reduction $$2H^{+} + 2e^{-} \rightleftharpoons H_2 \quad (2)$$

Alessandro Volta's pile utilised paper to separate the anode and cathode and prevent short-circuit, and no current would pass through our external circuit. In the Volta pile, the electrolyte was brine soaked in a paper separator. Brine is ionically conductive due to its salt content, and it is electronically insulating. Today, we expect electrolytes to meet more requirements, such as also having a wide voltage stability window, and suitable viscosity.

The voltaic pile is an early example of what is referred to as a primary cell, which can only be discharged once since the formation of hydrogen gas (2) cannot be reversed. Eventually, the system will either deplete the source of hydrogen ions or zinc metal and at this point, the cell will have reached the end of its usable life. Though primary cells have their uses, this thesis concerns secondary cells, that can be discharged and charged multiple times.

2.2 Electrochemical Principles of Operation

From the examples of the voltaic pile, we have gained fundamental definitions and concepts. needed when describing batteries and their electrochemistry. The first is oxidation, the process of losing electrons, and the associated raising of a species oxidation state. Conversely, we have reduction, which is the process of gaining electrons, and thus reduction of a species oxidation state.

Reduction $$O^+ + ne^- \rightleftharpoons R \quad (3)$$

Oxidation $$R \rightleftharpoons O^+ + ne^- \quad (4)$$

In a galvanic cell (a cell capable of spontaneous discharge), oxidation occurs at the anode, and reduction occurs at the cathode. This is the convention used in the naming of electrode materials.

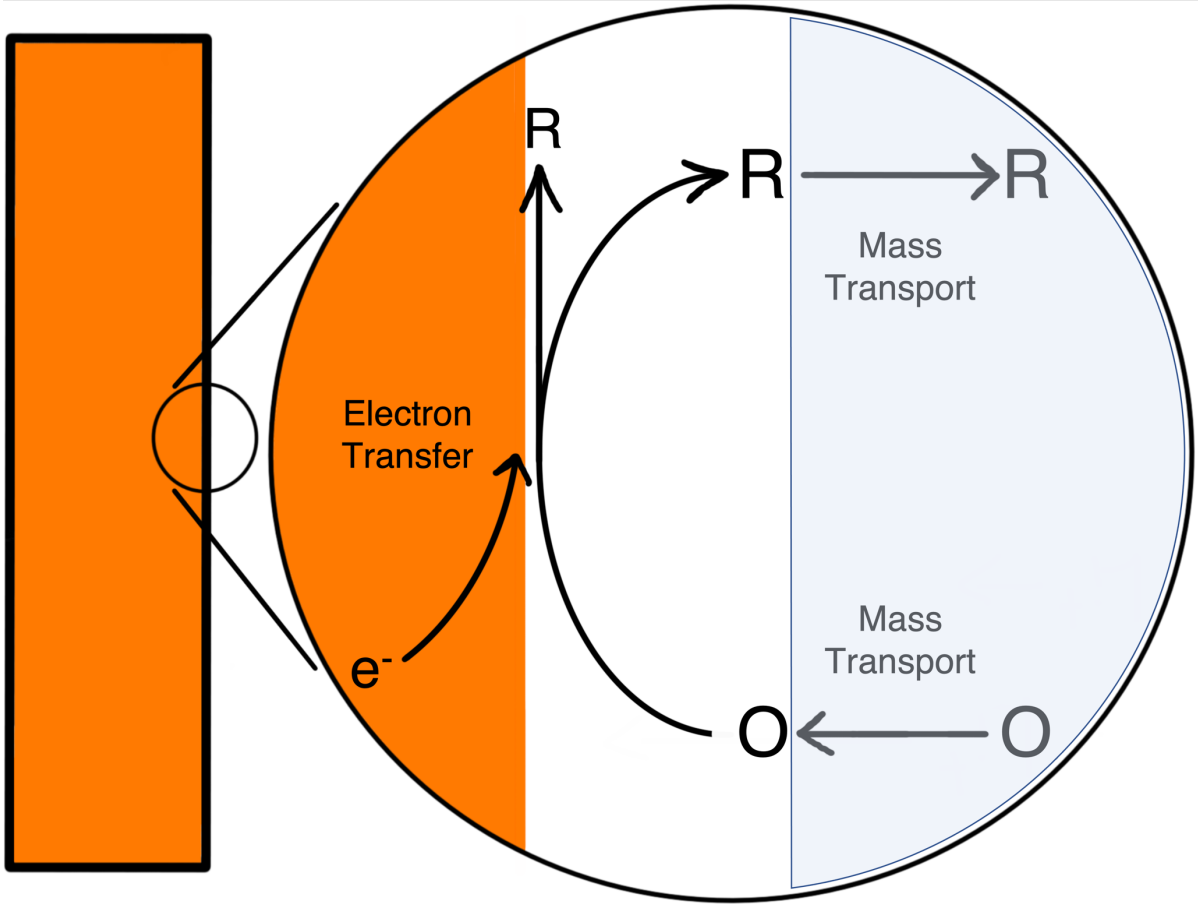

Figure 2 Schematic of the process of mass transport and electron transfer at the electrode surface.

The processes of reduction and oxidation occurs at the electrodes. In the case of reduction, the species to be reduced, **O**, needs to move from the bulk electrolyte to within proximity of the electrode surface, i.e., mass transport is required. Mass transport represents a series of transport mechanisms, such as convection, migration, and most importantly, diffusion. The diffusion of ions through a solution can be described by Fick's first law, demonstrating the dependency of a concentration gradient for ion transport, where the flux of species is given by:

$$J = -D\frac{dc}{dx} \tag{5}$$

J is the flux of ions, D the diffusivity, and $\frac{dc}{dx}$ is the concentration gradient. At the electrode, the species undergoes the process of electron transfer and gains an electron. species **O** is reduced to **R**. What happens to the species after this point varies with battery technology. It can enter the electrolyte solution, or it can stay at the electrode.

The electrochemical reactions define the battery's voltage as each electrode has its own 'electrode potential', based on the spontaneous redox reactions at the electrode surfaces. These redox reactions have a redox potential, a metric that describes the tendency of a chemical species to be reduced and thus its affinity for gaining electrons. The higher the redox potential, the greater the affinity of gaining electrons. In the electrochemical cell, the voltage observed is the difference between the electrode potentials

$$E^\circ_{cell} = E^\circ_{cathode} - E^\circ_{anode} \tag{6}$$

and the cell potential is related to the Gibbs free energy of the redox reactions of the cell:[9]

$$\Delta G^\circ = -nFE^\circ \tag{7}$$

where n is the number of electrons transferred, and F is Faraday's constant. This set of equations shows greater the voltage, the more significant the free energy change. After establishing the relationship between Gibbs free energy and cell potential, the relationship between cell potential and the products and reactants of the redox reaction can be determined:

$$\Delta G^\circ = \Delta G^\circ_{products} - \Delta G^\circ_{reactants} \tag{8}$$

In the case of the voltaic pile, the overall cell reaction during discharge can be written as:

$$Zn + 2H^+ \rightleftharpoons H_2 + Zn^{2+} \quad (9)$$

As such, the Gibbs free energy of the galvanic discharge can be written as:

$$\Delta G^\circ = [\Delta G^\circ(H_2) + \Delta G^\circ(Zn^{2+})] - [\Delta G^\circ(Zn) + \Delta G^\circ(2H^+)] \quad (10)$$

The standard redox potential of the Zn anode is -0.76 V vs SHE, and the standard reduction potential of H_2 formation at the Cu anode is 0 V vs SHE. Thus, the overall cell potential is 0.76 V vs SHE under standard conditions (concentration 1M, pressure 1 bar), using equation (7) the Gibbs free energy can be written as $\Delta G^\circ = -nF(0.76\ V)$. Therefore, we see that a positive cell voltage produces a value for ΔG° that is negative, thus demonstrating a positive cell voltage indicates a thermodynamic driving force behind cell discharge.

However, these equations and values are derived from them, are based on reduction potentials, measured under standard conditions. To describe the potentials observed in cells under non-standard conditions, the following expression is used to describe the cell voltage:[9]

$$E = E^\circ + \frac{2.3RT}{nF}\log\frac{[\mathrm{O}]}{[\mathrm{R}]} \quad (11)$$

Equation (11), known as the Nernst equation, is arguably one of the essential equations used in electrochemistry, linking the concentrations of oxidised and reduced species to cell potential, but only under equilibrium conditions. However, cell operation is a dynamic process, with the concentrations of species constantly changing. Thus, equilibria are not always established.

At the electrode surface there will always be redox reactions taking place. At equilibrium the magnitude of the reduction and oxidation reactions will be equal cancelling each other out. For a zinc anode this would be mean the oxidation to make Zn^{2+}, and the reduction back to Zn would be equal. This is known as the exchange current density,[9] and its value changes depending on the nature electrolyte and ion concentration.[10]

$$j = j_a + j_c = 0 \tag{12}$$

An additional crucial metric is the current a battery produces during cell discharge. By measuring current and integrating with respect to time, we obtain the capacity, describing the charge that the battery can store. Each active material has a theoretical specific capacity, an absolute maximum capacity the material has for energy storage, based on molecular weight and the number of electrons transferred during electrochemical reactions:

$$Q = \frac{nF}{m} \tag{13}$$

where *n* is the number of electrons transferred, *F* is the Faraday's constant, and m is the molar mass of the active material. Taking the example of the Volta pile, and considering the anode reaction of equation (1), the theoretical specific capacity of Zn can be calculated as:

$$Q_{Zn} = \frac{2 \times 96485\ C\ mol^{-1}}{65.38\ g\ mol^{-1}} = 819.87\ mAh\ g^{-1} \tag{14}$$

The experimentally measured capacity is often normalised by the mass of active material in the cell to determine the specific capacity or by the electrode area, giving areal capacity (Figure 3).

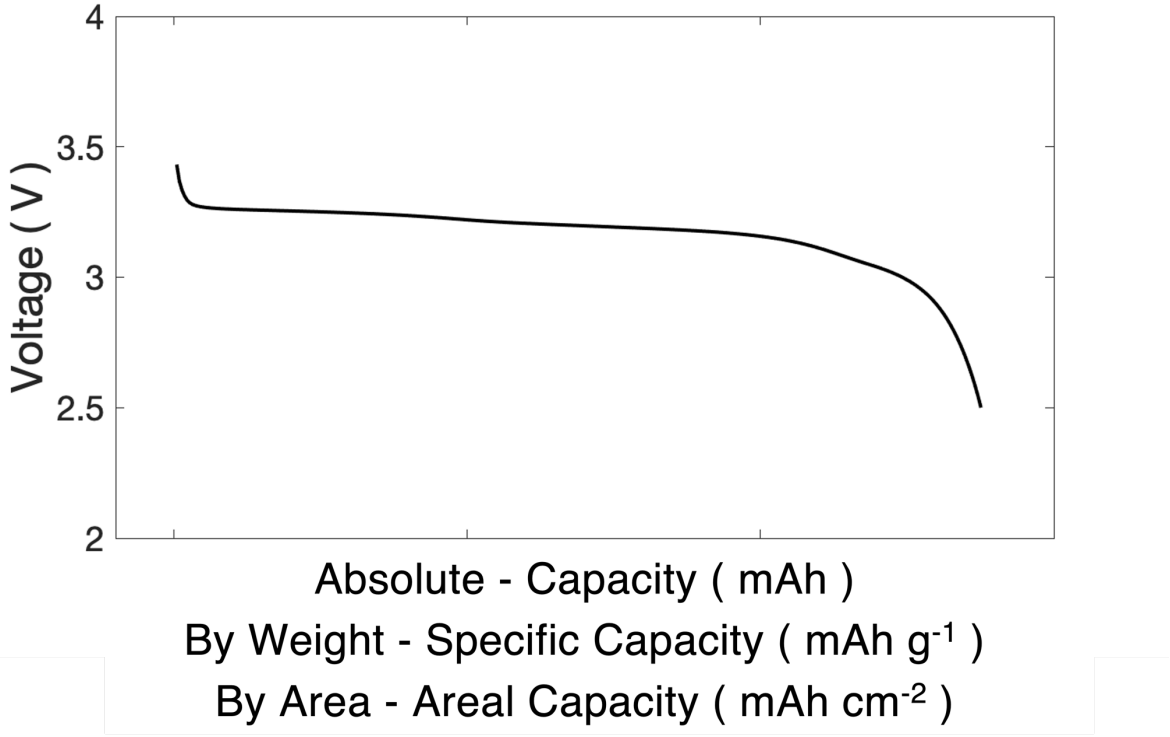

Figure 3 Typical Li-ion discharge voltage profile, with voltage plotted against capacity, showing the interchangeability of capacity, specific capacity, and areal capacity.

Another important metric of a battery is the coulombic efficiency. It is the ratio between the charge and discharge capacities, i.e., a measure of a battery's reversibility. To demonstrate the importance of understanding coulombic efficiency, we can take an example from the EU Strategic Agenda for Battery Research, which states a goal of achieving 80% capacity retention after 1000 cycles,[11] resulting in the following calculation:

$$\left(0.8^{\left(\frac{1}{1000}\right)}\right) * 100 = 99.98\% \tag{15}$$

To determine the coulombic efficiency (CE) we use the values of Q_{dis} and Q_{cha} (Figure 4):

$$CE = \frac{Q_{dis}}{Q_{cha}} * 100 \tag{16}$$

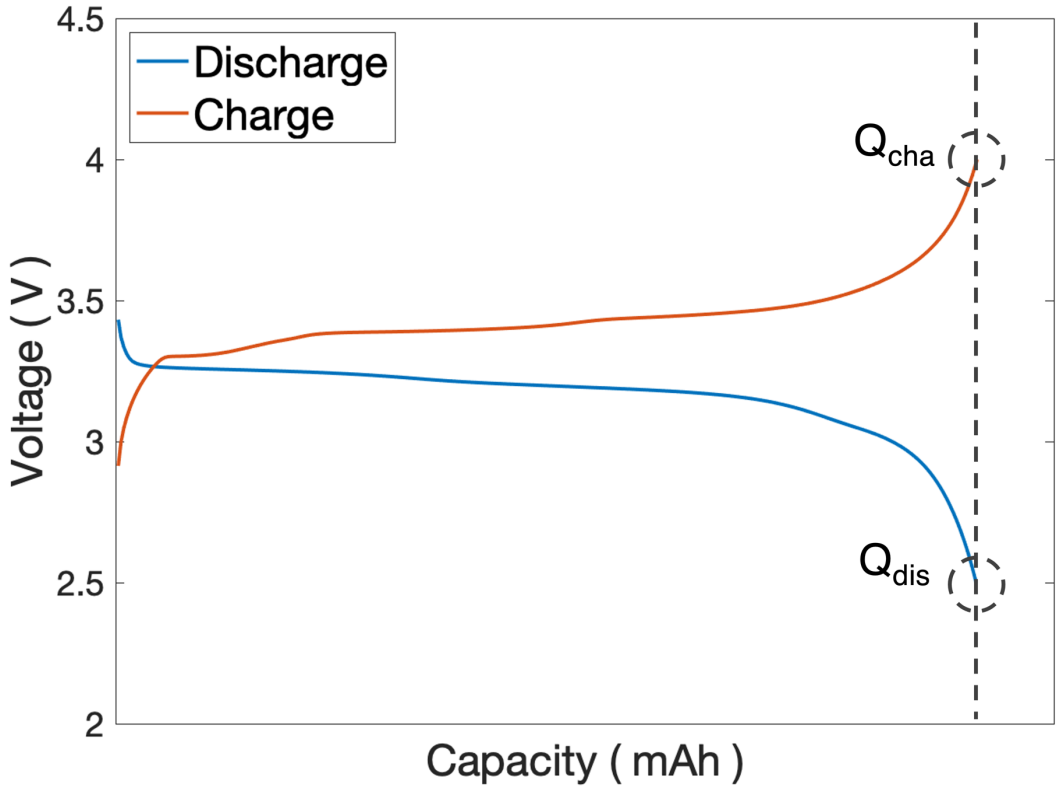

Figure 4 Voltage profile, demonstrating the relationship between charge and discharge capacities, and coulombic efficiency.

Using the formula for coulombic efficiency, we can measure the overall efficiency of a battery, considering the reactions taking place at both the anode and cathode. Alternatively, a half cell configuration can be used to isolate the reactions of a single electrode and determine the coulombic efficiency of that single process.

From the discharge profile one can determine the energy that the battery can store. The energy of the battery can be determined as the integral of voltage profile

$$\text{Energy} = \int_0^t V \cdot I dt \tag{17}$$

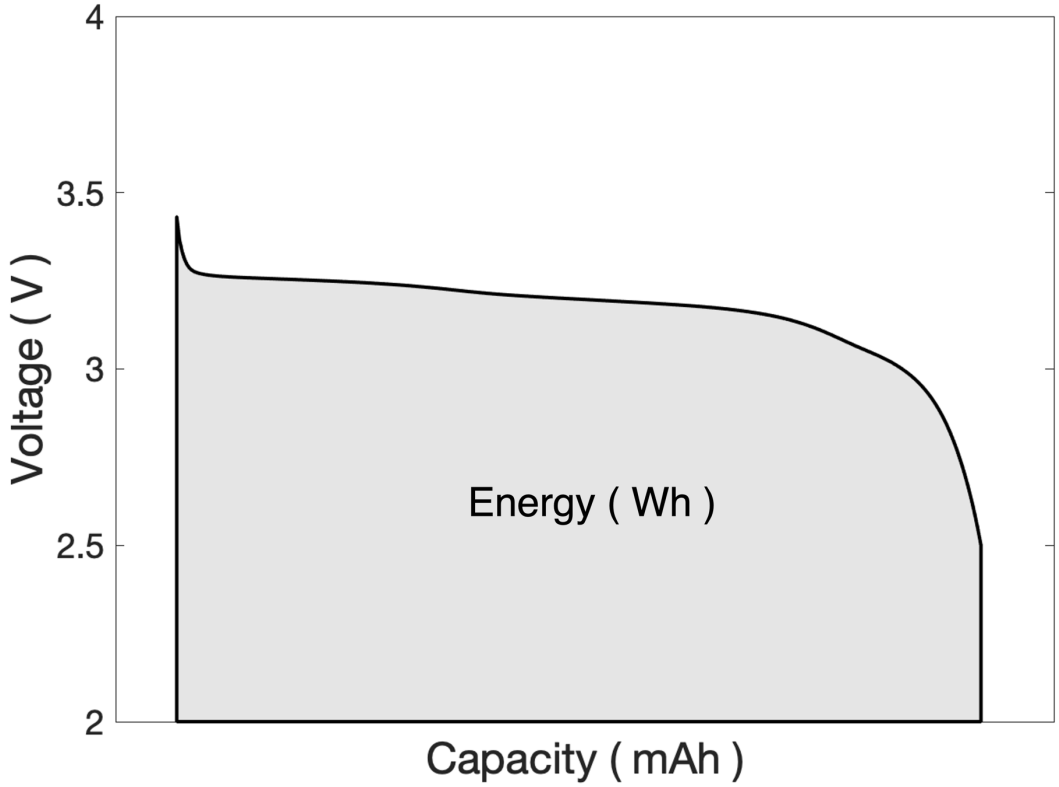

Figure 5 Relationship between voltage, capacity, and energy for a lithium-sulfur cell.

In battery research energy is often referred to as the specific energy (Wh kg^{-1}) or as energy density (Wh L^{-1}). Specific energy, or energy density, can be determined on many levels, from the active materials level, where the specific energy often high, to the pack level. At the electrode level components such as conductive additive and binder needs to be considered, and at the cell level current collectors, electrolyte, and separators must be considered. Finally, at the pack level all components in the care counted. Thus, there are many opportunities to increase specific energy or energy density, by engineering of materials to reduce weight and size, or by altering chemistries and increasing the energy content of active materials, as well as through cell and pack design.

2.3 Lithium Batteries

The most famous example of a rechargeable battery nowadays is the lithium-ion (Li-ion) battery. It has enabled an evolution in energy storage, we find Li-ion batteries in our mobile phones, laptops, and in nearly all battery powered electric vehicles. Since its commercialisation by Sony in 1991,[2] the early work carried out on the lithium-ion battery has gone on to see Akira Yoshino, M. Stanley Whittingham, and John B. Goodenough receive the 2019 Noble Prize in Chemistry.[12,13] The key to the Lithium-ion battery's success is based upon its 'rocking chair' type mechanism, where lithium ions (Li^+) are moved between the anode and cathode, and inserted between layers in the electrode material.[14,15]

What initially made lithium such an interesting material for energy storage originates from its location on the periodic table. Sitting up in the top left corner of it has a low atomic mass, giving lithium an incredibly high specific capacity. Lithium has a high tendency to shed the electron sitting in its outer shell, giving it one of the lowest reduction potentials, -3.04 V vs SHE. Combining these two factors makes lithium an ideal material to use in batteries.

The original concept for a lithium battery, introduced by M. Stanley Whittingham, used a layered sulfide material as a cathode.[16] However, this configuration was considered unsuitable due to stability issues of the cathode material, and the instability of using Li-metal as the anode material. Due to lithium's low reduction potential, it is also highly reactive and unstable towards the electrolytes used at the time. The stability issues associated with the use of Li-metal as an anode were solved by replacing metallic lithium with graphite.[17] The use of graphite would still allow the cell to deliver a high voltage, whilst side stepping the some of the safety issues that arise from the use of metallic lithium.

The first commercial Li-ion batteries from Sony had a specific energy of 80 Wh/kg, since then significant progress has been made, with one of the most popular suppliers (LG Chem) now offering cells with a specific energy of 265 Wh/kg,[18] and more recently CATL reporting to have cells that reached 304 Wh/kg.[19]

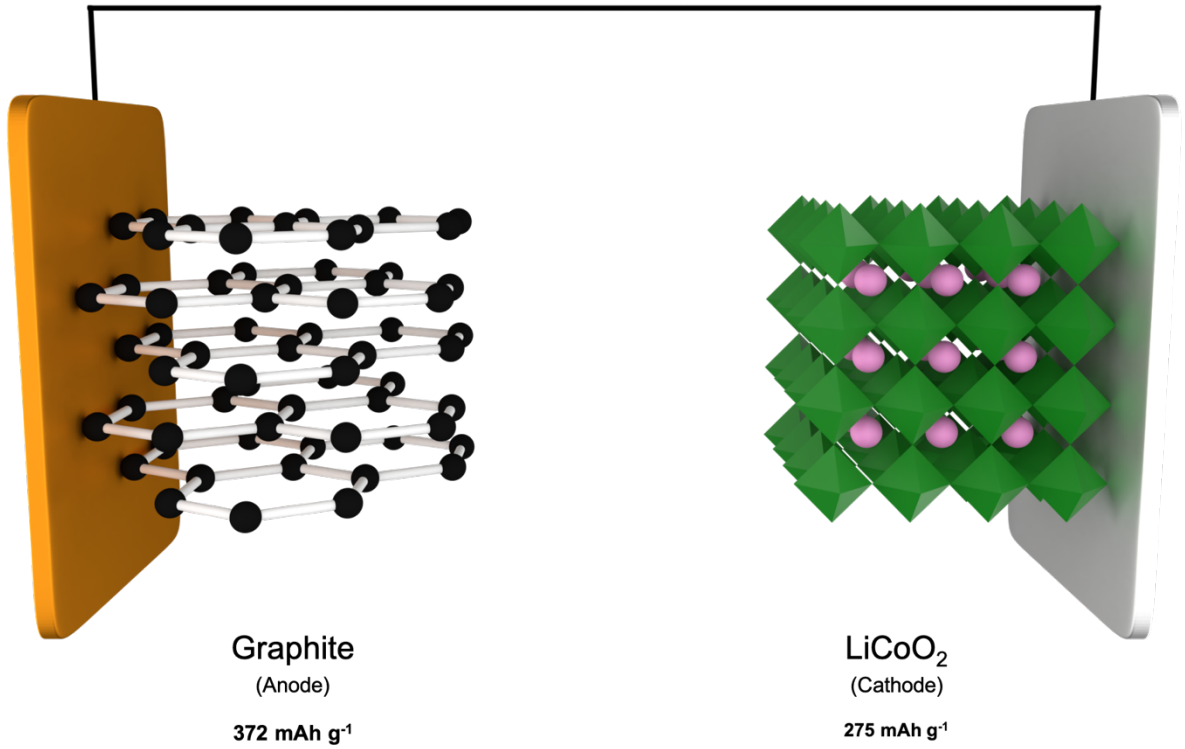

Figure 6 Schematic of a Li-ion battery, demonstrating the layered structure of the graphite anode and the crystal structure of an insertion type cathode.

When we talk about Li-ion, it is an umbrella term that represents a multitude of cathode chemistries such as $LiFePO_4$, $LiMn_2O_2$, and $LiNi_xMn_yCo_zO_2$, just to name a few, often coupled with a graphite anode. All these chemistries carry various unique characteristics, considering cyclability, capacity, operating voltage, and safety. However, one concept that they all have in common is that they all rely on intercalation and insertion processes, where Li^+ ions are inserted into a host structure. With graphite as the anode, the following reaction takes place:

$$Li^+ + e^- + C_6 \rightleftharpoons LiC_6 \tag{18}$$

The reduction potential of this reaction is below the stability window of commonly used electrolytes, causing the electrolyte to breakdown in contact with the graphite. The breakdown is in fact crucial to stabilising the graphite anode and enabling stable cycling through the formation of a solid electrolyte interphase (SEI).[20] The SEI is a layer that forms on the surface of the graphite, forming an additional phase in contact with the electrolyte. It has been extensively studied, with early models of the SEI being proposed by *Peled et al.*,[21,22] Further analysis to determine the SEI composition was carried out in the decades following, discovering

that it is a nanometre thick layer (10-30nm)[23] composed of electrolyte decomposition products.[24–26]

At the cathode the following takes place when using $LiCoO_2$ as active material:

$$LiCoO_2 \rightleftharpoons Li^+ + e^- + CoO_2 \tag{19}$$

Combing the anode and cathode reactions gives the full cell reaction:

$$LiCoO_2 + C_6 \rightleftharpoons LiC_6 + CoO_2 \tag{20}$$

These reactions impose a physical constraint in terms of specific capacity, and as such a limit in specific energy i.e., how much energy can be stored in the materials in terms of their weights. Figure 5 has previously shown how energy can be determined as the integral of time and voltage as a function of capacity. Increasing either one of these two values will increase the energy the battery can store demonstrating a need for batteries that can operate safely at higher voltages, or batteries that demonstrate a significant increase in specific capacity.

3 Next Generation Batteries

For the Li-ion battery, we have come close to the limits of how much energy the system can store. As the demand for batteries with higher specific energies increases (> 400 Wh kg^{-1}) we need to look beyond the current standard and consider alternative chemistries or technologies, so called 'Next Generation Batteries' (NGBs).The term Next Generation Battery encompasses a whole range of technologies, from sodium-ion (Na-ion) which can provide a sustainable alternative to the current dominant technology, to Li-metal and Li-Sulfur (Li-S) which theoretically boasts a huge increase in energy density. These are just a few technologies, and Table 1 shows the properties of some common NBG technologies.

With next generation battery technologies, the aim is to increase metrics such as capacity, safety, and sustainability. This requires a search for novel electrode materials, electrolytes, and cell chemistries, such as the use of alternative ions. Potential candidate ions to be used in batteries are Na and K which have low reduction potentials close to that of Li, -2.71 V and -2.93 V respectively, and as such these chemistries are receiving increased attention by the research community.[27,28] Other candidate ions include, Mg, Ca, and Al, as noted in Table 1. To address the issues of safety, cost, and increased capacity, Lithium-Sulfur and Sodium-Sulfur chemistries have considerable potential. Both Li-S and Na-S take advantage of the high-capacity sulfur cathode, to take full advantage of this high-capacity cathode the cell would need a high-capacity anode. Despite the Na-metal anode having a slightly lower capacity of 1166 $mAhg^{-1}$ than its Li-metal counterpart, which has implications when the cell is balanced, a sodium based battery carries the advantage of the active material abundance. However there are issues of high Na-metal reactivity and poor room temperature performance of Na-S cells.[29]

Technology	Advantages
Na-ion	Similar to Li-ion[30], low cost of Na[31], abundance of Na[31]
Li-S	High energy density[32], low cost of S[33], abundance of S[34]
Li-O_2	High energy density[32], abundance of O_2
Na-S	High energy density, low cost of materials, abundance of materials[31,35]
Mg	High energy density[36], abundance
Ca	Low cost, high abundance[37]
Al	High energy density[38], abundance

Table 1 Summary of Next Generation Battery Technologies.

3.1 Sodium-Ion

Sodium based batteries are already starting to see commercial production, with CATL (the same company that has produced the 304 Wh/kg Li-ion battery) announcing that they will bring to market a 160 Wh/kg Na-ion battery.[39] One of the major advantages of the sodium ion chemistry, is its analogy to Li-ion,[30,40] allowing a smooth transition from current Li-ion production lines to their Na-based counterparts. Despite the clear advantages and drive to produce Na-ion batteries, their development can't reach the levels of the Li-ion battery since the common graphite anode is unsuitable for use with Na-ion cathodes, as a consequence of the poor Na intercalation capacity, only 35 mAh g^{-1}.[41] Originally, the poor performance of Na intercalation in graphite was thought to be because of the increased ionic radii of Na^+, and as such it was not able to fit between graphite layers.[42,43] However, this reasoning has been disproven since both K^+,[44] and solvated Na^+ [45–47] can be intercalated between graphite layers.

The origin of the poor intercalation capacity arises from the interactions between sodium and graphite.[48] This highlights the need to investigate alternative materials for use as an anode in Na-ion batteries. The current most common anode for Na-ion is hard carbon, a material with a complex microstructure. Instead of being composed of regularly spaced and stacked graphene sheets, there are domains of randomly spaced and randomly orientated graphene sheets. This results in a more complex storage mechanism and a theoretical capacity of ~280 mAh g^{-1} (compared to the 372 mAh g^{-1} capacity of graphite).[49]

To move the Na-ion technology forward, the storage mechanism needs to be understood. It has been demonstrated that the use of co-intercalant solvents, such as DME, stabilises the interaction between Na^+ and the graphite.[45,47,50] However, such an approach often leads to exfoliation and destruction of the graphite layers, leading to a drop off in the capacity achieved. One approach that provides a unique solution and enable to the reversible intercalation of Na^+ is graphene. Graphene refers to a single atom layer thick sheet of hexagonally arranged carbons, the difference between graphene and graphite is that graphite is made up of many graphene layers. An advantage of graphene, specifically chemical vapour deposition (CVD) graphene, is that it can be tailored and stacked on a layer by layer basis. With CVD graphene being grown as a single layer, there is an opportunity to perform chemical modification.[51] Depending on the type of chemical modification, there is scope to modify the properties of the graphene surface and tune the interaction between Na^+ and the graphene. However, such modifications

present challenges, the CVD graphene is grown and then modified on a layer by layer basis, with each layer possessing an area of only a few square millimetres. This resulting mass of the material is measured in nanograms, and due to the nature of graphene, it also has large surface area. Despite only small amounts of materials being produced, the unique ability to be tuned presents an opportunity to study fundamental interactions between the graphitic material and Na^+.

3.2 Lithium Sulfur

The Li-S reaction has a theoretical specific capacity of 1672 mAh g^{-1} and high specific energy, on the active materials level. This chemistry has the potential for the realisation of high specific energies on the cell level that surpass that of current Li-ion batteries.[52,53] Beyond improvements in specific energy, there are further factors that make the Li-S a promising successor to Li-ion, including the abundance, low cost and low-toxicity of raw materials, and potential improved cell safety.[54]

In a Li-S cell, sulfur is used in its elemental form, S_8, this is a material that is 10th in a ranking of elemental abundances,[55] it can be found worldwide making it accessible,[56] and often is the side product from established chemical processes, making it a very low cost material.[33] When you combine this with other elements to be used in the Li-S cell, such as carbon black, there is the potential to create a cell that has a considerably lower cost, on the materials level, than current Li-ion cells.[52] Furthermore, sulfur containing electrodes are considered to be less toxic,[33] an advantageous property considering the possible implementation of large scale applications.

The large theoretical specific capacity is derived from the following reaction:

$$S + 2Li^+ + 2e^- \rightleftharpoons Li_2S \tag{21}$$

From this reaction a theoretical specific capacity for the active material, sulfur, can be calculated to $1672\ \text{mAh g}^{-1}$, far surpassing the theoretical values for the active materials of Li-ion batteries ($\sim 275\ \text{mAh g}^{-1}$).

Having spoken in of the advantages of the Li-S chemistry, one must also consider the series of challenges which are preventing the implementation of this technology. These challenges stem from the complex chemistry that occurs in the Li-S cell, differing from that of the currently used Li-ion and Na-ion batteries. The cell's reaction mechanism can be broken down into a series of conversion reactions of sulfur.[57]

$$S_8 + 2e^- + 2Li^+ \rightarrow Li_2S_8 \quad (22)$$

$$Li_2S_8 + 2e^- + 2Li^+ \rightarrow Li_2S_{8-n} + Li_2S_n \quad (23)$$

$$Li_2S_n + (2n-2)2e^- + (2n-2)Li^+ \rightarrow Li_2S_{8-n} + nLi_2S \quad (24)$$

These ideal reactions all contribute to the total capacity of the cell and occur at different stages of the discharge. The voltage profile shown in Figure 7 is typical when using a liquid electrolyte. The profile can be broken into three main regions and determined by corresponding processes.

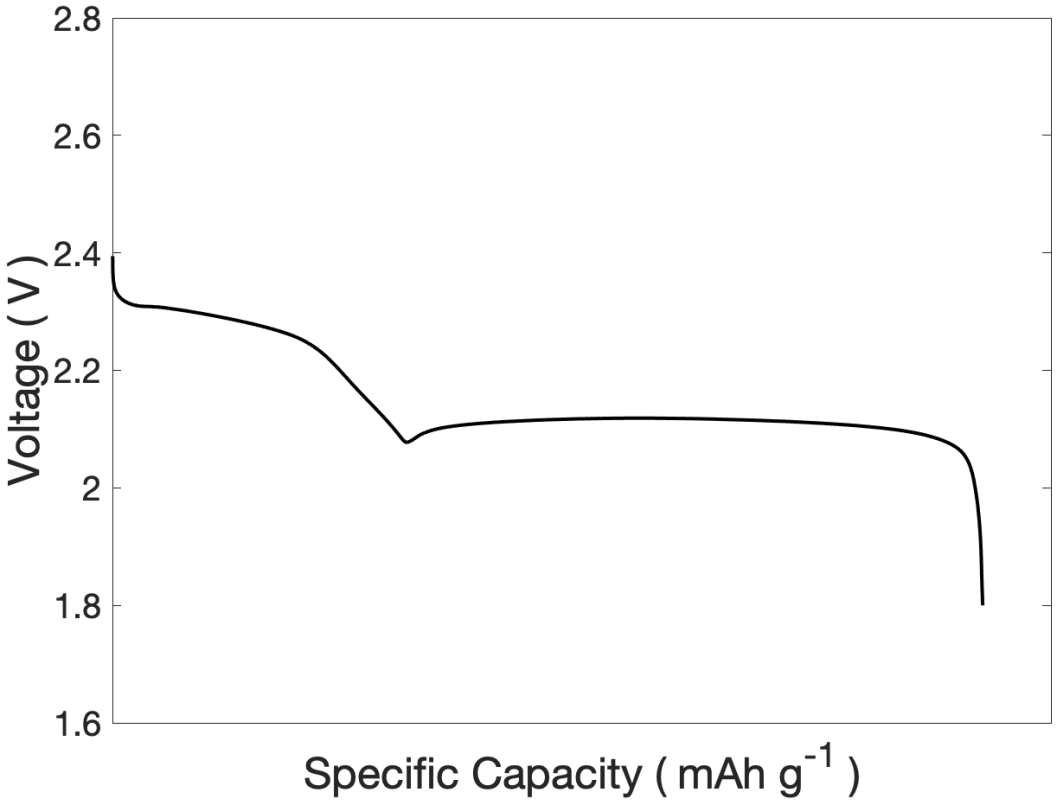

Figure 7 Voltage profile showing the characteristic plateaus observed at ~2.4 V and ~2.1 V respectively in a liquid electrolyte Li-S cell.

At the start of discharge the conversion of elemental solid sulfur (S_8) to soluble long chain polysulfides (Li_2S_8), (22), occurs and is a solid to liquid phase transition since elemental sulfur has a low solubility in commonly used electrolytes where Li_2S_8 is usually highly soluble. Subsequently the conversion of the soluble long chain polysulfides to short chain polysulfides

occurs, (23), and is a liquid-liquid transition. Finally, the conversion of short polysulfide chains (Li_2S_n) to insoluble lithium sulphide (Li_2S) occurs, (24), this is a liquid to solid phase transition. It is these phase transitions determine the characteristic shape of the voltage profile with liquid electrolytes.

Equation (22) represents the process at the plateau close to 2.4 V in Figure 7, and the plateau represents the equilibrium established as soldi elemental sulfur dissolves and forms soluble long chain species. Equation (23) related to the slope moving from 2.4 V-2.1 V, where a complex series of both electrochemical and chemical conversions of the soluble species takes place.[57,58] These soluble polysulfide species are able to freely diffuse through a cell's electrolyte, driven by concentration gradients, and their concentrations will affect the extent of these reactions. The next step in the voltage profile is the 2.1 V plateau, representing equation (24). What is notable about the 2.1 V plateau is the drop in the cell potential at the start of the 2.1 V plateau, which represents the supersaturation of the electrolyte and the energy needed to nucleate the solid Li_2S product on the electrode surface.[59–61] For efficient conversion to Li_2S, it is crucial that the polysulfide species diffuse back to the cathode to be converted to Li_2S, impeding this process will limit cell capacity. The then deposited Li_2S, just like sulfur, is an electronic insulator and forms a porous layer that restricts the diffusion of polysulfide species effectively blocking the electrode surface.[62] After some time the blocking of the electrode surface will prevent further deposition of discharge products, thereby significantly limiting the cell's capacity.[63]

This dissolution-precipitation conversion process is common to liquid electrolyte cells. However, as a consequence of this conversion mechanism, high-energy density Li-S cells seem to only reach 60-70% of their theoretical capacity.[64] This can stem from underutilisation of the active material, i.e. not all elemental sulfur being converted, the loss of sulfur to the electrolyte, and finally polysulfide deposition on the Li-metal surface.

Polysulfide Migration and Shuttle

All Li-S cells with the dissolution-precipitation reaction show the movement of Li_2S_n species. This movement of polysulfide species in unavoidable due to the soluble nature of species and their diffusivity in liquid electrolytes, allowing them to diffuse out of the cathode, through the separator and reach the anode. This movement is often linked to the poor performance of Li-S cells with the previously mentioned loss of material, where polysulfides diffuse out of the cathode and into the bulk electrolyte, often these polysulfide species are unable to diffuse back to the cathode and as such are lost. Furthermore, polysulfide species are able to diffuse all the way to the anode where they can irreversibly react with the Li-metal surface, once more reducing the active content of the cell. However, Li-S cells can also suffer from poor coulombic efficiencies, through a process known as the polysulfide shuttle mechanism.

The shuttle occurs during charge when polysulfides are oxidised to form soluble long chain species which diffuse to the Li anode, where they gain electrons from the Li, reducing the polysulfide species to short chains, and then diffuse back to the cathode where they are once more oxidised (Figure *8*). This means that polysulfide species can be reduced without accepting an electron from the cathode, essentially creating an internal short circuit, and in doing so reducing the efficiency of the cell.

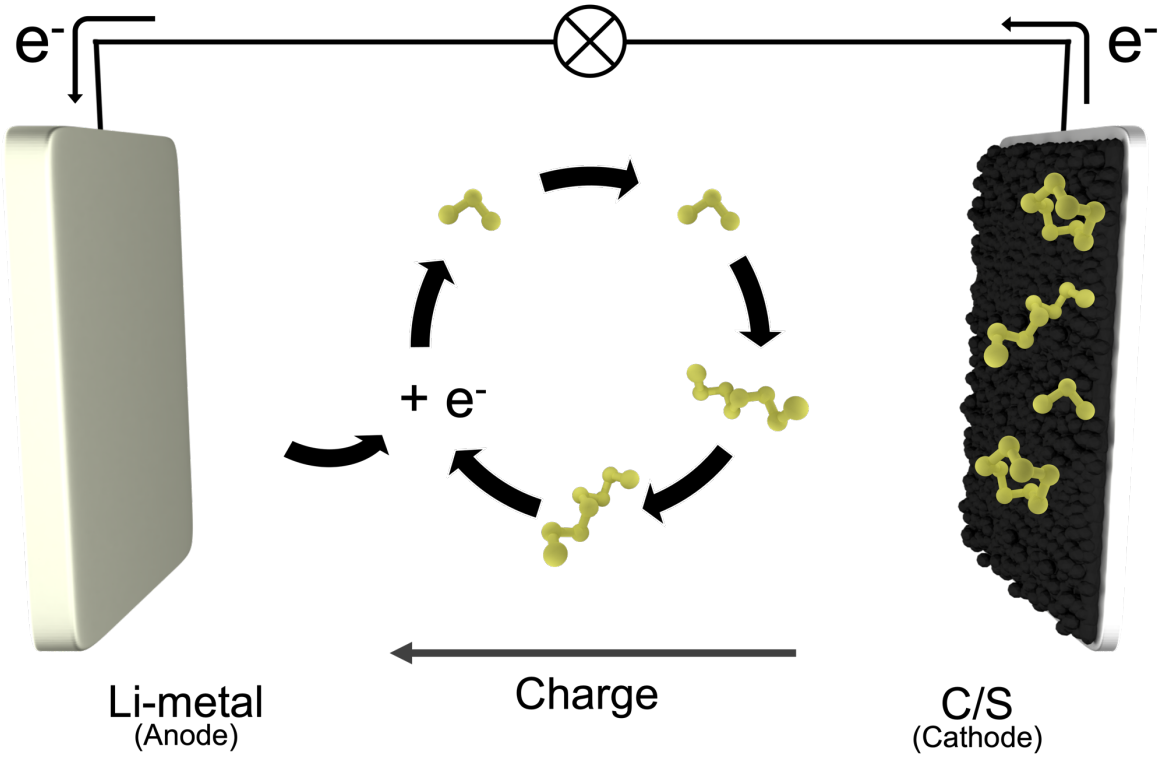

Figure 8 Schematic of Li-S cell with a Li-metal anode and carbon/sulfur (C/S) composite cathode. The cycle shown in the centre is a demonstration of the polysulfide shuttle effect.

There are strategies that address the polysulfide dissolution and migration, such as confinement within hosts,[65–68] preventing polysulfide species from leaving the cathode matrix and thus limiting their diffusion from the cathode. Physical interlayers have been used to block polysulfide movement,[69,70] allow the polysulfide species to dissolve and diffuse freely within the cathode matrix, but unable to diffuse into the separator and bulk electrolyte.

One notable way to prevent polysulfide diffusion has been with the use of solid-state electrolytes and all solid-state batteries. In a voltage profile of an all solid-state cell no plateaus are observed, instead only a decaying voltage suggesting that no phase change occurs (Figure 9). There is very little information on the specifics of the mechanisms in all solid-state cells. A recent study showed that the solid-state conversion of S_8 to Li_2S occurs via an Li_2S_4 intermediate,[71] however this work was performed in a solvate ionic liquid electrolyte to induce a so-called ‘quasi-solid-state’ mechanism. As such the true discharge mechanism for all solid-state Li-S cells is still relatively unknown, however, sulfide based solid electrolytes have been shown to enable specific capacities of 1600 $mAhg^{-1}$ at room temperature.[72,73] Solid electrolytes carry many advantages over traditional liquid type electrolytes, such having a wider

electrochemical stability window, greater thermal stability, and reduced flammability.[74] However, most importantly, a consequence of the all solid-state battery is that polysulfide species are confined to the cathode, if they are at all formed. In the solid-state, any polysulfides that are formed would be unable to migrate from the cathode to the anode as they are physically blocked, thus preventing the parasitic shuttle mechanism.[75]

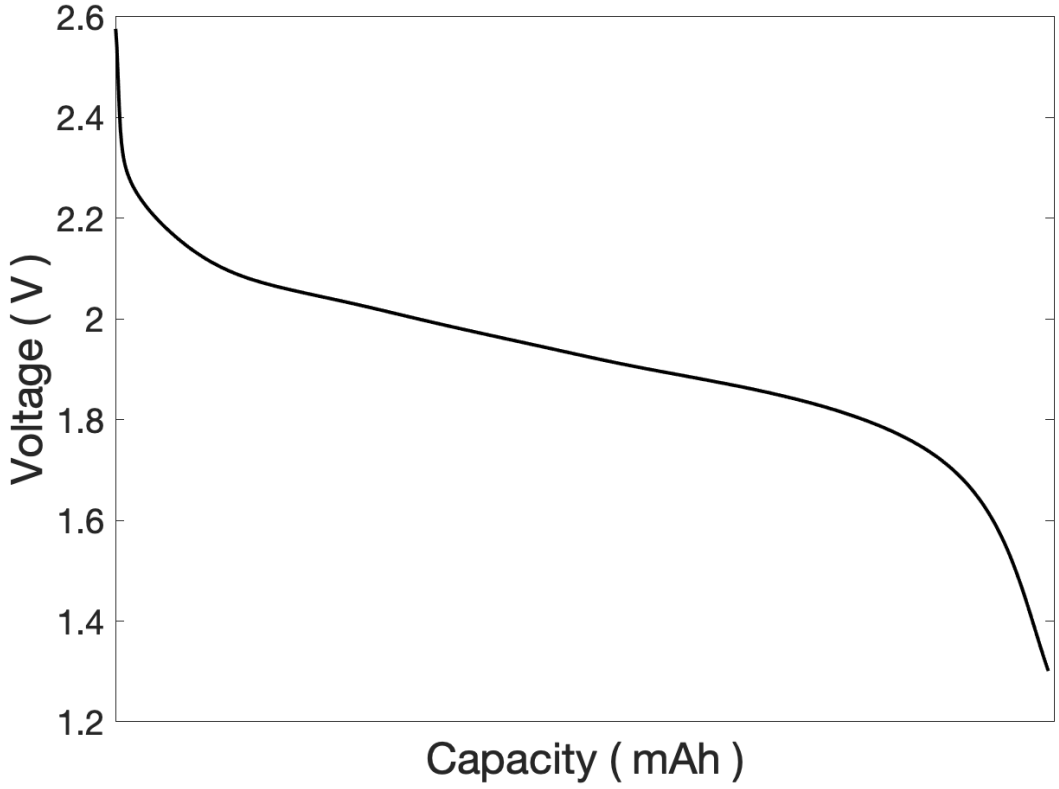

Figure 9 Voltage profile for an all solid-state Li-S cell using a LiI-Li_3PS_4 solid-state electrolyte.

Other methods mainly focus on the passivation of the Li-metal anode, the most common form of passivation is the use of lithium nitrate ($LiNO_3$) as an additive in the electrolyte. $LiNO_3$ breaks down and forms a protective layer that continues to allow the conduction of Li^+, while at the same time protects the metal from shuttling species.[76,77] However, the solid-electrolyte interphase (SEI) formed with $LiNO_3$ breaks down continuously with unwanted side reactions during cycling and thus needs to be replenished. The constant replenishment of the SEI consumes $LiNO_3$ eventually leading to cell failure. For this reason $LiNO_3$ is referred to as a sacrificial salt, and in cells that rely on the use of this additive, there is an intrinsic link between its concentration in the electrolyte, the volume of electrolyte used, and the cell lifetime.[78]

Cathode

For the Li-S cell to operate effectively, the cathode is composite of sulfur and a conductive matrix, since sulfur by itself is an insulator.[79] Most sulfur cathodes are a mixture of sulfur in its elemental form, conductive carbon such as SuperP or Ketjen Black, and finally a conductive binder such as PVDF (structure shown in Figure 10).

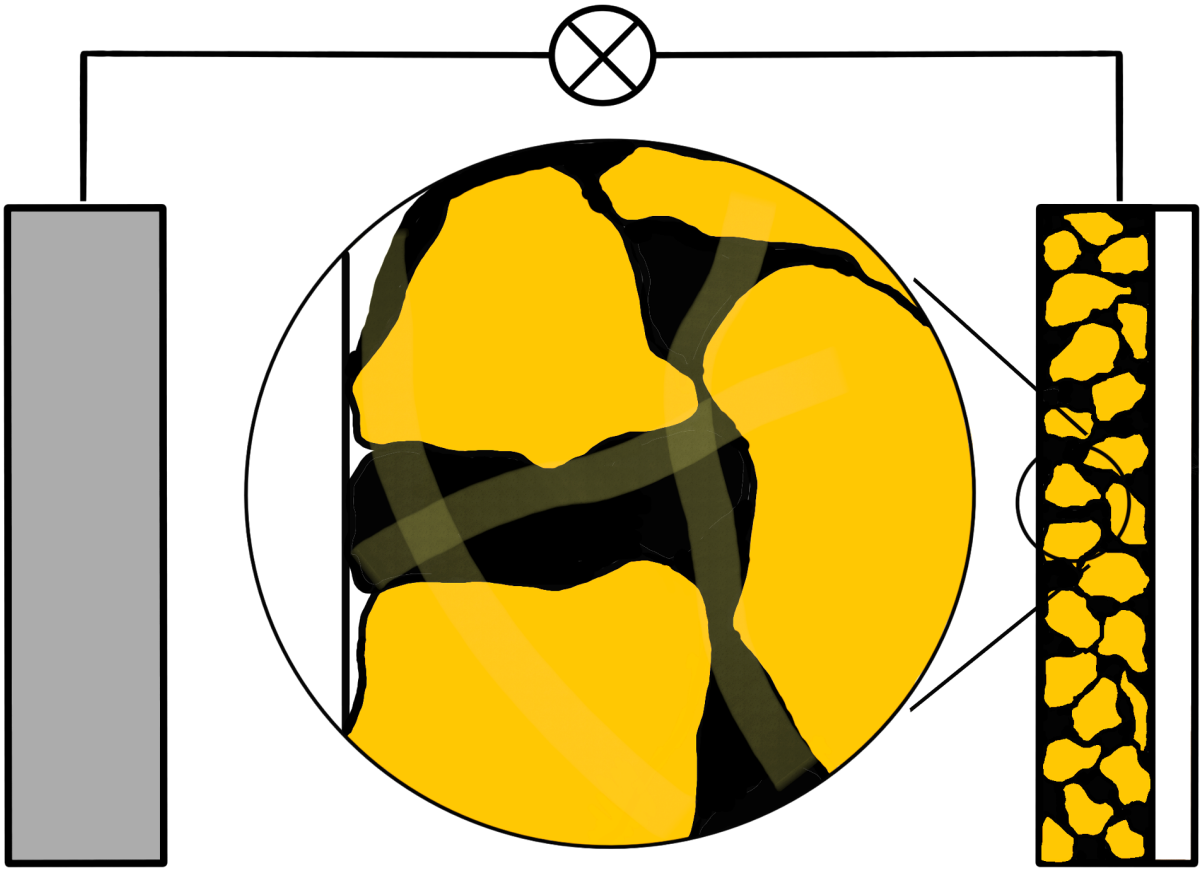

Figure 10 Schematic of an Li-S cell with a lithium anode (left) and sulfur cathode (right). The sulfur electrode is a composite of sulfur sitting in a matrix of carbon and conductive binder, all coated on an aluminium foil current collector.

The Li-S cathode was first seen in a 1962 application,[80] with very little work performed on the cathode until in 2009 when nanostructured cathodes that behaved as polysulfide reservoirs, confined the soluble polysulfide species within nanopores, enabling high efficiency and long lifetime Li-S cells.[81] This confinement of species tackles a challenge of the Li-S cathode, which is the dissolution of the cathode. Further challenges faced are low specific energies on the cathode level, consequent of the addition of conductive carbon and binder, lowering the active material loading.

When designing cathodes for a Li-S cells, one must also consider the issue of volume expansion. The conversion of S to Li_2S induces an 80% volume expansion[57] which must be accommodated within the cathode structure, while simultaneously the cathode must have enough surface area and pore volume to accommodate the deposition of Li_2S during discharge, in an attempt to achieve the cell's full capacity.

To tackle the dissolution of the sulfur cathode, methods have been developed to encapsulate the sulfur and subsequently formed polysulfide species within TiO_2 shells, in a so-called 'yolk-shell' nanoarchitecture.[68] This method confident produce a cell with a high coulombic efficiency and ability to cycle for over 1000 cycles. There have been recent efforts to create Li-S cells that are binder-free and use self-standing carbon supports, in an effort to reduce materials in the cells that do not contribute to the electrochemical performance, to raise the specific energy.[52,82] These free standing architectures can impregnated with sulfur and have been shown to reach specific energies on the cell level of over 400 Wh kg^{-1}.[52]

Electrolyte

The choice of electrolyte composition has a direct impact on the performance of the Li-S cell, as a consequence of the reaction pathways they induce.[83] The most notable of liquid electrolytes are the glymes such as dimethoxyethane (DME) and tetra ethylene glycol dimethyl ether (TEGDME). These glymes favour the dissolution of sulfur and cells with this type of electrolyte typically follow the dissolution-precipitation type reaction mechanism discussed previously (Equations (22)-(24)). Other types of electrolytes are catholytes (where the cell's active material is dissolved in the electrolyte), [84] ionic liquids,[85,86] solvated ionic liquids,[87] and various solid electrolytes.[88] All of which have their own advantages and flaws.

A favoured glyme based electrolyte is a binary mixture of the glyme 1,2-dimethoxyethane with 1,3-dioxolane, and the addition of salts. A commonly used salt for Li-S cells is lithium bis(trifluoromethanesulfonyl)imide (LiTFSI), a concentration of 1 M is used to reach an ionic conductivity of 10^{-2} S cm^{-1}. The use of ethers and glymes leads to the previously mentioned dissolution-precipitation reaction. When dissolution of sulfur takes place and soluble polysulfides are formed, not only do electrochemical reactions takes place, but also chemical

reactions, such as the disproportionation of polysulfide species. One example of a common disproportionation reaction in dissolving electrolytes is the formation of the tri-sulfur radical:

$$S_6^{2-} \leftrightarrow S_3^{*-} \tag{25}$$

S_3^{*-} is seen as a reaction intermediate and its presence can be linked with the stability of the species in a given electrolyte, and that stabilising these redox active polysulfide species is crucial to high performance Li-S cells.[89,90] Hence the dissolution of sulfur is paramount to provide acceptable reaction kinetics at room temperature and to reach a high utilisation of the active material.

For liquid type Li-S electrolytes, there are electrolytes with high polysulfide solubility characterised by a high donor number, low polysulfide solubility electrolytes with a low donor number, and non-dissolving electrolytes. The polysulfide solubility in an electrolyte has been directly related to cell performance, due to the morphology of the final deposition product. The high donor number electrolytes such as DME form particle like Li_2S deposits, where as the low donor number electrolytes, such as dimethyl sulfoxide, lead to a film-like Li_2S deposit. However, the high donor number electrolytes suffer from instability against Li-metal with the formation of a poor SEI.[90]

In addition to dissolving electrolytes there are non-dissolving electrolytes, an example of which are solvate ionic liquids, where the electrolyte is an equimolar mixture of TEGDME and LiTFSI, leaving no free glyme molecules.[91] Just as in the example of the quasi-solid-state electrolyte,[71] the solvate ionic liquid forces sulfur reactions in the solid-state, and results in cell with stable cycling and high coulombic efficiency, but usually low active material utiliastion.

Catholyte

A catholyte is an electrolyte with the active material dissolved in it, cathode + electrolyte = catholyte. Mixing Li and S in a stoichiometric ratio in a solvent will form a polysulfide solution, the solution at this point turns a characteristic crimson colour (Figure 11). Catholytes carry several advantages, such as enabling high active material utilisation.[52] However, one of the main advantages of a catholyte is that the dissolved polysulfides can be both a source of active material, while also acting as the Li-salt.[53] A catholyte can also be used in conjunction with a regular carbon-sulfur composite cathode, in this case the catholyte buffers the dissolution of sulfur, while also increasing the cell energy density.[53,84] A further approach commonly combines the catholyte with a sulfur-free cathode and has the ability to overcome issues such as cathode mechanical failure and enable the cells to reach high areal capacities,[82,92]

Figure 11 Image of catholyte, 5%wt Li_2S_8 in TEGDME with 0.4. M $LiNO_3$.

For catholyte based Li-S cells, a range of specific capacities have been reported, but the main advantage is high sulfur loading. Agostini *et al.*[93] and Cavallo *et al.*[82] reported a sulfur loading of 3.2 mg cm^{-2}, Lim *et al.*[92] reported a sulfur loading of 6.5 mg cm^{-2}, and He *et al.*[94] reported loadings reaching 10 mg cm^{-2}. When compared to work by Pang *et al.* (4.6 mg cm^{-2}),[95] and Chung *et al*. (12 mg cm^{-2}, 46 mg cm^{-2}),[96] one sees a huge increase in loadings, while the authors claim to maintain a low electrolyte to sulfur ratio.[97] However these latter C/S cathodes require the use of materials such as cobalt and titanium disulphide which act as polysulfide 'absorbers', trapping polysulfides in the cathode structure. In stark contrast, the efforts by Cavallo *et al.,* and Lim *et al.* make use of carbon-based materials such as carbon nanofibers and reduced graphene oxide aerogels in combination with LiTFSI-free electrolytes. However, many of these catholyte cells still suffer from specific capacities not reaching their full potential, with poor rate capability and low active material utilisation.

3.3 Lithium Metal

Lithium metal was first used an anode material for secondary batteries back in the 1970s, and was considered an ideal candidate due to its high specific capacity (3862 mAh g^{-1}).[16] A further advantage of Li-metal as an anode is that it has one of the lowest reduction potentials (-3.04 V vs. SHE). Combining the theoretical capacity with low reduction potential gives the Li anode the ability to reach a high energy density,[98] and this high energy density on the electrode level makes it an ideal candidate to couple with sulfur or oxygen chemistries in an attempt to reach a high energy density batteries.

.

When moving to Li-metal, we now focus on the processes of Li plating and stripping, as opposed to intercalation and deintercalation, where Lithium ions undergo the process of electron transfer and electrocrystallization on the surface of a given substrate.[10] When charging and discharging a Li-metal battery, the following redox reaction takes place at the anode:

$$Li \rightleftharpoons Li^{+} + e^{-} \tag{26}$$

Figure 12 shows a typical stripping/deposition voltage profile of Li. During deposition there are several processes that we must consider. We have already spoken of electrocrystallization, and this relies on the process of nucleation. In Figure 12, the region characterise by the voltage spike (a) is the Li nucleation regime. In this region, the overpotential is the sum of the charge transfer overpotential, diffusion overpotential, and surface overpotential. Following the nucleation regime, we see the Li growth regime (b). In this region the overpotential is due to the mass transport of Li from the bulk electrolyte and through the SEI.[99] Thus, we now see the basic mechanisms that define Li growth, and it manifests in the voltage profiles seen for the stripping/deposition processes, and what is off acute importance is the diffusion of Li, the interaction between Li and the deposition surface, and the mass transport of Li through the SEI.

Despite the clear advantages of using Li-metal as an anode material, it suffers from a low coulombic efficiency, and its use presents safety hazards. Both of these critical issues arise from the growth of Li-metal dendrites during the plating (deposition) process, which are structures that form due to the uncontrolled growth. Dendrite structures have the ability to pierce the battery's separator, causing a short circuit and potential thermal runaway of the battery. Such growth has often led to cells catching fire and having to be recalled, [100,101] hence why carbon anodes were eventually for Li-ion batteries.

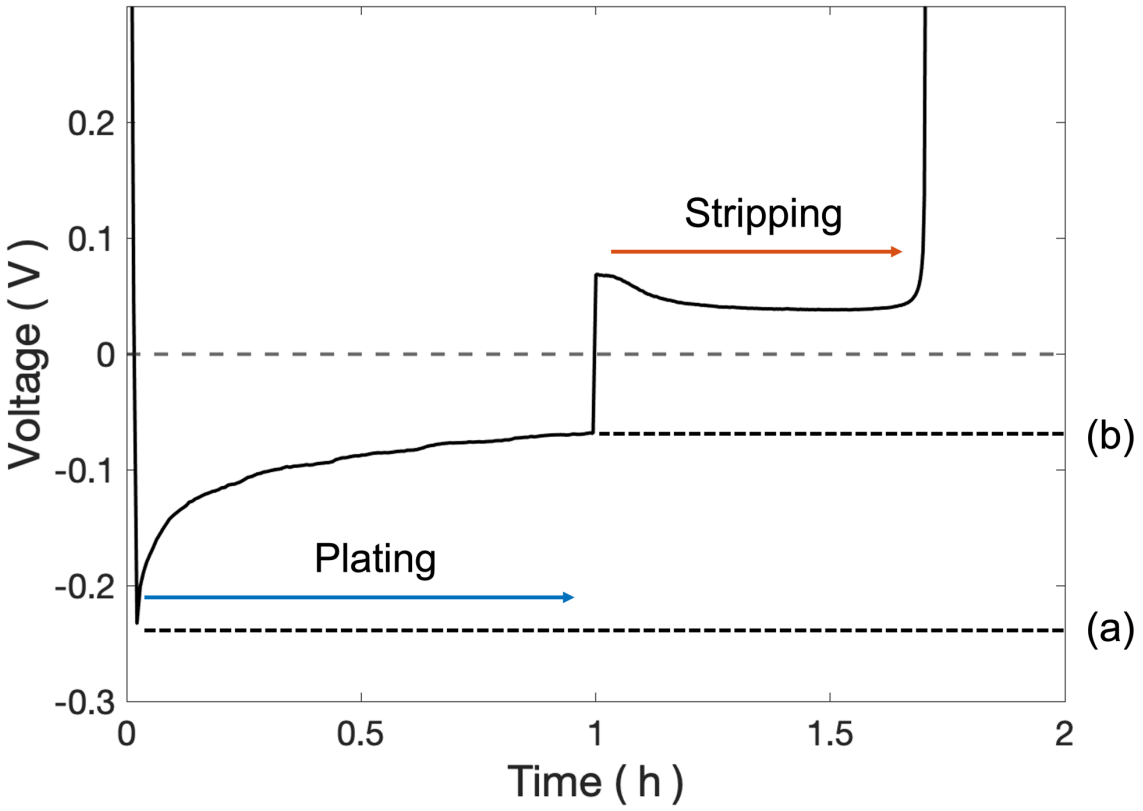

Figure 12 Characteristic voltage profile of the plating (blue) and stripping (orange) process seen in Li/Cu half cells. a) Demonstrates the over-voltage representing nucleation of Li-metal b) The overvoltage of the steady-state deposition of Li-growth.

The growth of dendrites in Li-metal batteries is a consequence of the stripping and deposition of Li, as demonstrated by equation (26). Here Li-metal is both deposited (plated) and stripped directly to and from the Li-metal surface. One of the major factors leading to dendrite growth is the transport of Li^+ through the electrolyte. The three mechanisms of mass transport (diffusion, migration, and convection) have already been discussed, however in batteries, diffusion and migration are the dominating processes.[102] An even flux of Li^+ ions is crucial

to the formation of a dense, and dendrite free Li deposit. Looking beyond the effect of mass transport on dendrite growth, a further influential factor that dictates the growth of Li-metal, and these dendrites, is the solid electrolyte interphase (SEI).

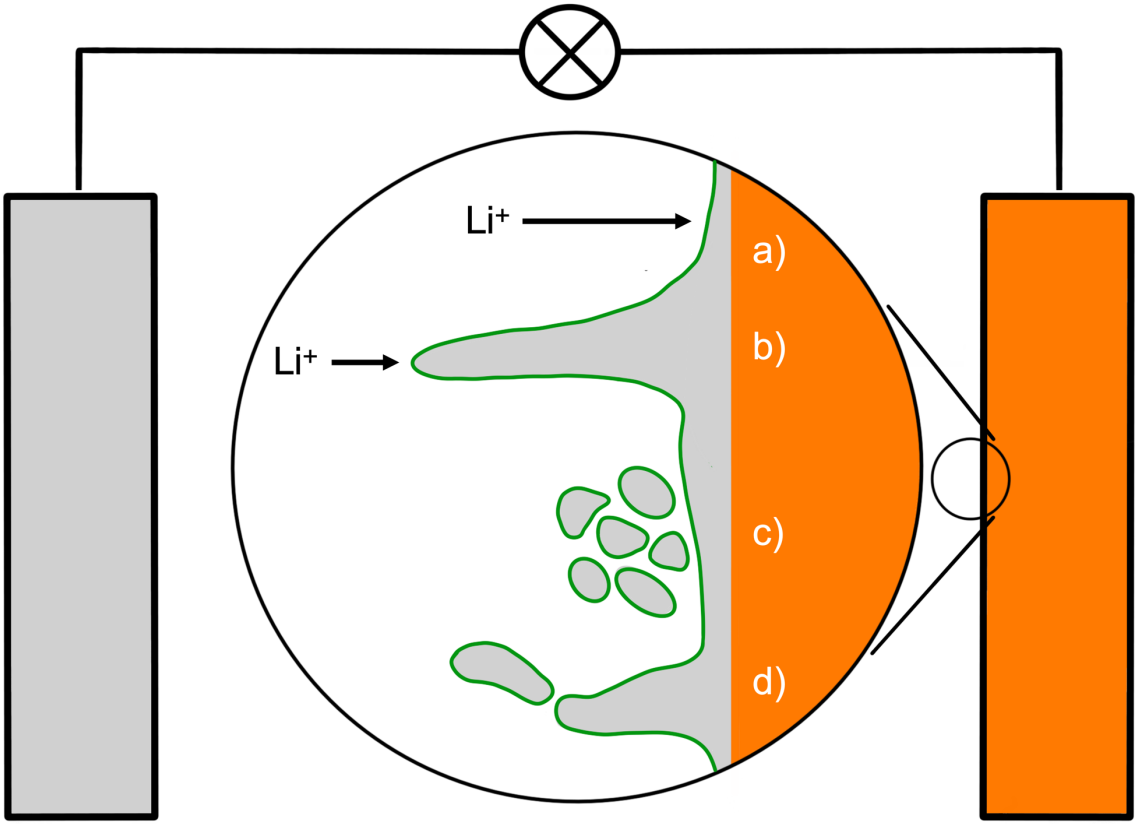

Figure 13 Illustration of various forms of Li metal deposition, in this case on a Cu substrate. a) Ideal Li deposition. b) Deposition leading to dendrite formation. c) 'Dead' Li morphologies. d) Formation of dead Li due to the SEI growing round Li-metal and disconnecting from the bulk.

This SEI layer must have several properties to enable effective plating and stripping of Li-metal. First and foremost, it must be electronically isolating, this prevents electron transfer with the electrolyte, the subsequent parasitic side reactions, and potential loss of Li. Second, the SEI must be ionically conductive, allowing Li^+ ions to pass through and plate on the bulk Li surface. Finally, the SEI must be mechanically stable, so that it can resist volume and morphological changes.[23] If part of the SEI were to break, a region of increased Li^+ transport would be created, and this too would lead to the formation of dendrites from this defect. In solid electrolytes, it has been shown that to suppress Li dendrite growth a shear modulus twice that of Li metal is needed,[103,104] thus it must be considered that the strength of the strength of the SEI will itself play a role on the suppression of dendrite growth.

An example of an electrolyte additive that has been identified as a good component for forming a stable SEI on Li-metal is $LiNO_3$.[105] It has been found that $LiNO_3$ breaks down on the surface of the Li-metal forming inorganic LiN_xO_y species, and organic ROLi.[105,106] Recent reports have shown that the addition of $LiNO_3$, enables reversible and long-term stripping and plating of Li-metal, and achieve coulombic efficiencies of 98.8%.[107] The interaction of Li-metal with $LiNO_3$ containing electrolytes has already been established, showing that $LiNO_3$ enables the formation of a compact and homogenous layer when Li-metal is immersed in the electrolyte.[106] However, these results do not comment on how $LiNO_3$ affects Li-metal deposition upon cell cycling, and what type of Li microstructure is formed.

However, in the case of the Li-metal batteries, the SEI formed often leads to the formation of dead Li, Li structures that become surrounded by the non-conductive SEI, and eventually become disconnected from the bulk Li-metal.[108–111] This formation of dead Li leads to an overall loss of Li, thus a poor coulombic efficiency, and eventually the source of Li would become depleted. Therefore, to realise Li-metal as an anode material, the formation of 'dead' Li must be addressed to ensure batteries retain their capacity by achieving high coulombic efficiencies. Reports have quantified the amounts of this so-called 'dead lithium',[108] and attempted to determine how dead lithium is formed, with both cryo-TEM [108] and optical microscopy suggesting the formation is the direct consequence of a tortuous, whisker like morphology.

An advancement that is heavily reliant on highly reversible Li-metal stripping and plating is a concept known as the anode-free Li-metal battery.[88,112] In this concept the Li-metal foil that normally takes the role of the anode is replaced with a Cu substrate, all Li in this case would originate from the cathode (NMC [88] or Li_2S [113] cathodes, for example), and the Li would be deposited as Li-metal on the Cu surface. Such a concept relies on the smooth and dendrite free deposition of Li, for both safety reasons and to ensure ultra-high coulombic efficiencies, needed due to the lack of excess Li. The use of Cu as substrate for Li-metal deposition functions in a similar fashion as the Cu electrode did in the voltaic pile, where the Cu is not formally oxidised or reduced, but instead acts a surface where redox reactions of species in the electrolyte proceed. In this case, the Cu is a surface with Li is deposited (plated) and stripped.

3.4 Operando Measurements

3.4.1 What is an *operando* measurement

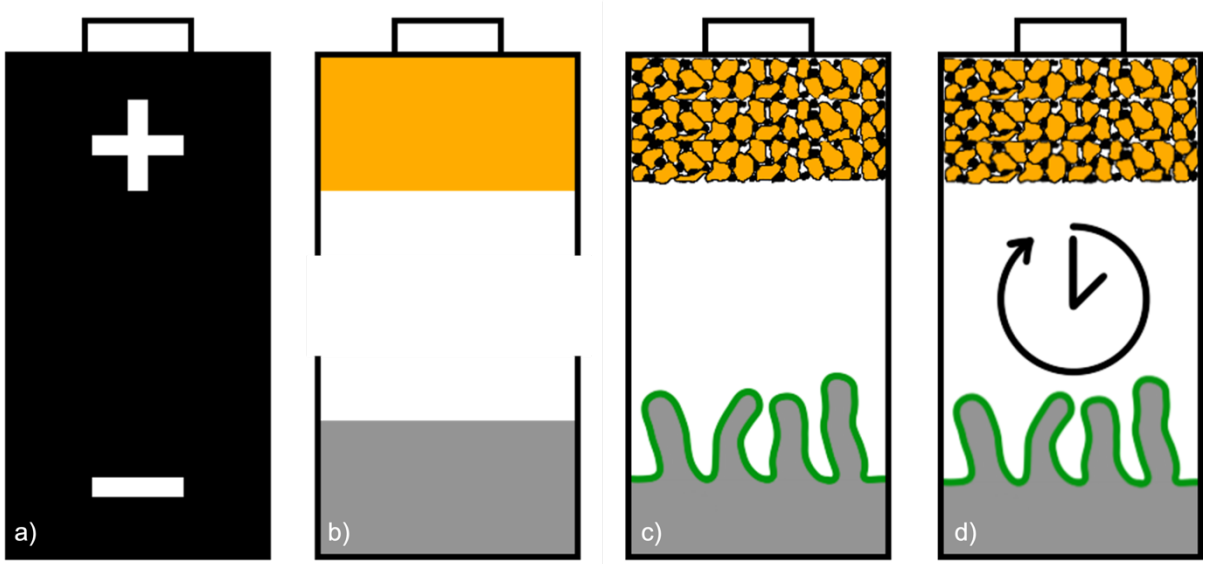

Figure 14 a) Observing the battery as a black box. b) Taking the battery apart to observe and analyse the electrodes, *ex situ*. c) Measuring the electrodes in their undisturbed environments for *in situ* analysis. d) Making measurements on the battery while the battery is in operation, *operando*.

Batteries are systems operating with processes spanning multiple length scales, from the Å and nm scale of ion transport and surface reactions, to the mm length scale of electrode coatings and their mechanical degradation. Not only are batteries multiple length scale systems, but the processes take place on multiple timescales, from the short times associated with processes such as electron transfer to long times associated with the decay in performance seen over multiple cycles. Thus, to effectively probe these evolutions, analytical techniques with compatible spatial and temporal resolutions are required.

Several forms of analysis can be utilised to understand the fundamental 'mechanisms' that determine a batteries operation. **a)** We can treat batteries like a black box. In terms of analysis, we can apply an input of current or voltage and collect the feedback of voltage or current. These are the most basic performance markers for batteries, and they can be determined by analysing a battery using a galvanostat/potentiostat. These measurements provide essential indictors such as capacity, voltage, rate capability, coulombic efficiency, power, impedance, and lifetime. Not to be overlooked, these electrochemical techniques are crucial for evaluating the performance

of new battery materials. **b)** We can disassemble the battery after cycling and inspect the internal cell components, observing any physical or chemical changes that may impact the battery's performance. Such analysis is referred to as *ex situ*. **c)** To avoid damaging samples during disassembly, we can use methods where we cycle, stop, and inspect internal components without disassembly, leaving the internal environment undisturbed. Subsequently, the cycles can continue, and a new measurement taken. This is defined as *in situ* measurements. **d)** Finally, we can make measurements while the battery is being charged and discharged, monitoring changes inside the battery as they happen. These measurements are referred to as *operando*.

Currently *operando* measurements draw a high degree of attention, which arises from the novelty of the information that can be gained from such measurements. An aspect that *operando* measurements can provide is the ability to continuously probe the same region in space of a sample, gaining a real-time insight to physical or chemical processes. Due to the nature of an operando experiment, the sample is not moved, this means both the electrochemical measurements and the analytical measurement are undisturbed. By continuously probing the same region, correlative studies can be made. Such correlative studies would include investigating a change of species concentration in an electrolyte as a function of state of charge,[114] or even following the evolution of a single particle during cell cycling.[115]

3.4.2 *Operando* Measurement Considerations

There are a huge range of *operando* studies that have been performed to analyse the chemical and physical processes inside next generation battery cells. For Li-S cells, significant work has gone into looking at the behaviour of sulfur and polysulfide species during charge and discharge with a wide variety of techniques. X-ray tomographic microscopy that has been used to show the dissolution of sulfur, changes of particle size, and changes to the carbon binder domain during discharge.[116–124] While x-ray diffraction that has shown the presence of solid α- and β-sulfur, and Li_2S at different points during discharge.[114,124–126] These are all techniques that are able to elucidate physical changes to materials and changes to solid phases, but not directly provide chemical information.

Techniques that are able to reveal chemical changes in the liquid phase include Raman spectroscopy,[114,127–131] UV-vis spectroscopy,[89,132,133] X-ray absorption spectroscopy,[134] and Electron Paramagnetic Resonance spectroscopy.[135] These techniques have been used to track the speciation of sulfur in a cell's electrolyte, or in the electrode, providing detailed insights to the chemical reaction pathways. Gathering such information is key when researching new technologies as it provides a deep understanding of the mechanism which can be used to build physical models,[58] or guide the design of novel materials.

When discussing *operando* methods, one can frame them in terms of spatial and temporal resolutions. Some techniques are limited by their spatial resolution, with EPR and UV-vis probing the bulk electrolyte in custom cells (Figure 15b), unable to determine what reactions or species that are specific to certain regions in the cell. In contrast, confocal Raman spectroscopy can provide information from a confined area (Figure 15c), useful for probing reactions at the anode or cathode, but is limited in terms of tracking interactions across the entire electrolyte volume. By only measuring bulk solutions, or by measuring at one point in the cell, and we can only observe one part of a complex puzzle.

Not only do these cells affect the spatial resolution, but their design can have an influence on cell chemistry. In the case of Li-S cells, key attention is paid to the ratio between electrolyte and sulfur (E/S ratio) which has been shown to alter performance.[136] Examples of the Raman for *operando* measurements show E/S ratios of 60 μL mg^{-1},[127] with more recent efforts

achieving 16-18 μL mg^{-1}-.[130] The work presented in Paper III achieves a similar E/S ratio of 21 μL mg^{-1}. Whereas in the example of the X-ray tomography studies E/S ratios of 5 μL mg^{-1} were achieved.[116] Furthermore the rate at which Li-S cells are cycled has a huge impact on the cell performance, with examples spoken above using cycling rates of C/60, C/20, C/20, and C/5 respectively. It can be seen that the example of the XTM experiment achieved the lowest E/S ratio, while simultaneously cycling the cell at the highest rate, there are several reasons for this, from electrolyte composition to electrode structure and separator used. However, the cell design itself may lend itself to such impressive performance.

The variances in cell design, from the materials to the casing, mean that experiments use a wide range of parameters for cycling, such as cut-off voltages and cycling rates. These differences lead to a wide range of cell performances, and often makes comparison between experiments challenging, and conclusion drawn are often only revealing fundamental processes.

As the methods used to analyse NGBs develop, acute attention should be applied to experiment designs that enable comparison between experiments. This can come in the form of multimodal experiments, where a single cell is simultaneously measured using different techniques such as x-ray absorption tomography and x-ray diffraction computed tomography, in a multi-modal set up providing direct comparison between the results. An alternative approach is the BIGMAP project which aims to create a framework promoting researchers to use a unified set of materials and cycling parameters, enabling comparisons between experiments.[137]

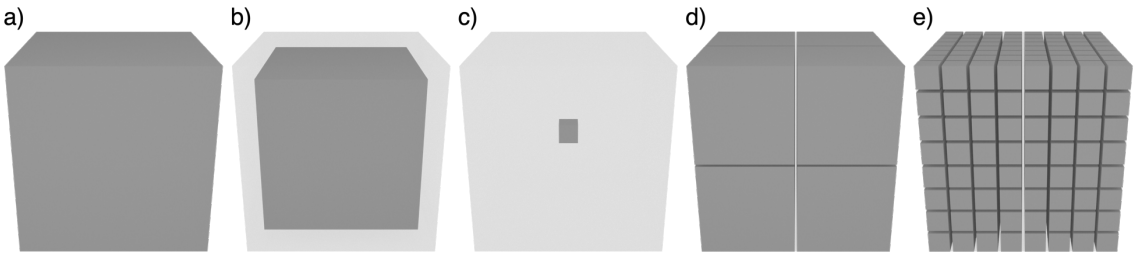

Figure 15 Visualisation of spatial resolution. a) A hypothetical volume to be probed. b) Representation of bulk measurement, where a single measurement represents a large portion of the total volume. c) Representation of a local measurement, where the measured volume represents a small portion of the total volume. d) A global measurement with a poor spatial resolution, where the total volume is represented by a small number of regions, each of which represents a large portion of the total volume. e) A global measurement, where the total volume is represented by a large number of regions, each of which represents a small portion of the total volume.

When probing morphological or phase changes of an electrode, such as the change of particles in size of µm, or growth of new phase as is the case with Li, a high spatial resolution is required. There are many examples of Li structures being imaged with cryo-TEM, where a cryo-protection system is employed in conjunction with electron microscopy, and spatial resolutions on the order of nm have been achieved.[108,138–140] These studies have been able to identify the formation of 'glassy Li' phases,[139] tortuous structures, suggested mechanisms for the formation of 'dead Li',[108] and even the fine structure of SEI.[140] However, despite the impressive resolutions achieved, the information gathered needs to be put into the context of the entire electrode. How do these changes on the nm level affect what is observed on the µm level, and in turn how are these structures manifesting on the mm level and affecting cell performance? Often compromises have to be made, between the resolution that can be achieved, and the total area that can be measured. Furthermore, the studies that reached nm resolutions were not *operando*, and as such they lack the ability to show the processes and their kinetics.

In an ideal case, measurements that analyse changes during battery cycling would require very high temporal resolutions, i.e., short measurement times, allowing changes within the battery to be continuously probed. *Wood et al.* used optical microscopy, to take 90 images during a 15 minute period, following the evolution of Li dendrites on the sub-micron level during cell cycling.[141] Despite this being an impressive example of a measurement that allows continuous visualisation of Li-metal growth with a high temporal resolution, the 2D nature of the experiment and limited field of view means that crucial details are lost, such as the distribution of Li-metal structures across the electrode surface.

With Raman spectroscopy, measurements can be made in seconds, Paper I and Paper III were able to make Raman measurements that were < 60s. With discharge processes that were > 5 hours, very little change to the cells took place during each Raman measurement. For XTM, the measurement times were also minimised to < 50 s, however in Paper VI the discharge time was 1 hour (Figure 16). Thus, changes to the cell would have happen during the measurement. This shows that the cell discharge rate was already at the limits of what would be compatible with XTM measurements.

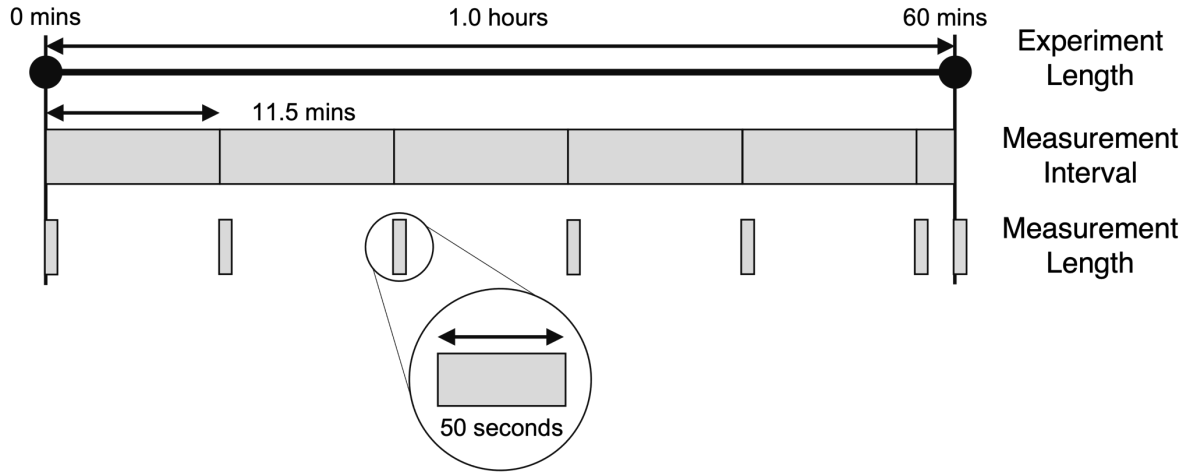

Figure 16 Schematic representing temporal resolution. A comparison between the length of measurement with regards to the overall length of the process to be probed (cell discharge), and the frequency at which measurements are made. This example shows a 1 hour cell discharge, where measurements are taken every 11.5 minutes, and each measurement takes 50 seconds. 6 measurements represented the hour long process. The time over which measurements were taken accounted for 8.3% of the total processes time.

The example of Figure 16, highlights the need to make measurements with high temporal resolutions, an added benefit is that fast measurement times enable more measurements to be taken during cell discharge, allowing the discrete observation of processes. The need for high temporal resolution is a strong motivation for using synchrotron techniques. Conversely, lab-source x-ray techniques (XTM, XRD, SAXS, etc.) are associated with long measurement times (hours) making these techniques unsuitable for *operando* measurements. However, due to their high flux of photons, synchrotrons enable rapid measurements (seconds) and consequently high temporal resolutions, revealing discrete changes to electrode structures.[142]

4 Theory and Experimental

4.1 Electrochemical Methods

4.1.1 Constant Current Cycling

To evaluate the performance of both full and half cells, galvanostatic constant current charge-discharge (CC) measurements are used. Here a current is applied at a given rate (mA), and the voltage response is measured, with voltage limits being applied (E_1 and E_2, Figure 17). These measurements provide information on; capacity by measuring how long the current is sustained before reaching the voltage cut-off limit, rate capability by observing the effect of increased applied current on the capacity, and coulombic efficiency. After prolonged galvanostatic cycling, comparisons can be made between cycles to determine capacity decay or changes in cell polarisation.

In galvanostatic measurements, data is typically reported showing voltage as a function of time or capacity, Figure 17. This way of displaying voltage means we can evaluate the cell regarding capacity and time. Still, it also gives us insights into phase changes resulting from the cell's electrochemical processes. Figure 17 shows a 2-step voltage profile during the discharge process. This indicates that there are at least two main electrochemical processes during the discharge reaction of this cell (in the case of Li-S).

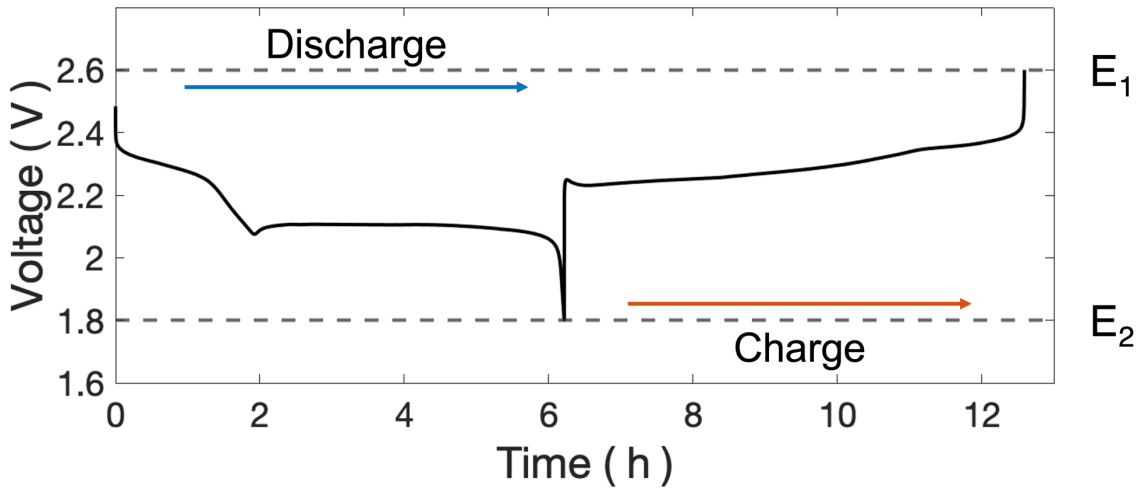

Figure 17 Example of galvanostatic voltage profile of a Li-S cell.

4.1.2 Stripping/Plating Experiments

Constant current measurements can also be used to estimate the stability of electrolytes against lithium electrodes. By applying a constant current density to a symmetric Li-Li cell, we drive the lithium stripping and deposition processes, much as we would have in our full Li-metal based cell. During this process, the voltage response can be measured, the overvoltage. This overvoltage represents the driving force of the oxidation/reduction process (stripping/deposition respectively) of Li/Li^+. Thus, a higher overvoltage means a higher interfacial resistance on the lithium in a given electrolyte. This effect is illustrated in Figure 18. During the long-term cycling, the drop or rise of overvoltage is also used to evaluate the interface stability between Li and electrolyte.

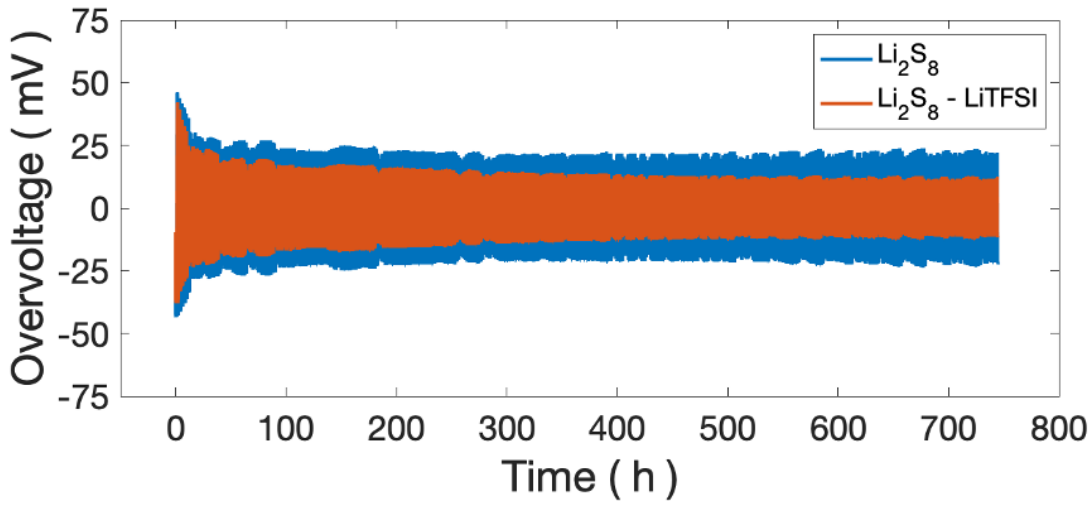

Figure 18 Example of a stripping/deposition measurement used to evaluate two different catholyte solutions.

4.1.3 Cyclic Voltammetry

Cyclic voltammetry is used for electrochemical analysis. It is a potentiodynamic measurement where the potential is controlled, and the current response is measured. The cell voltage is swept between two potential limits (E_1 and E_2), as shown in Figure 19 and the current response is recorded.

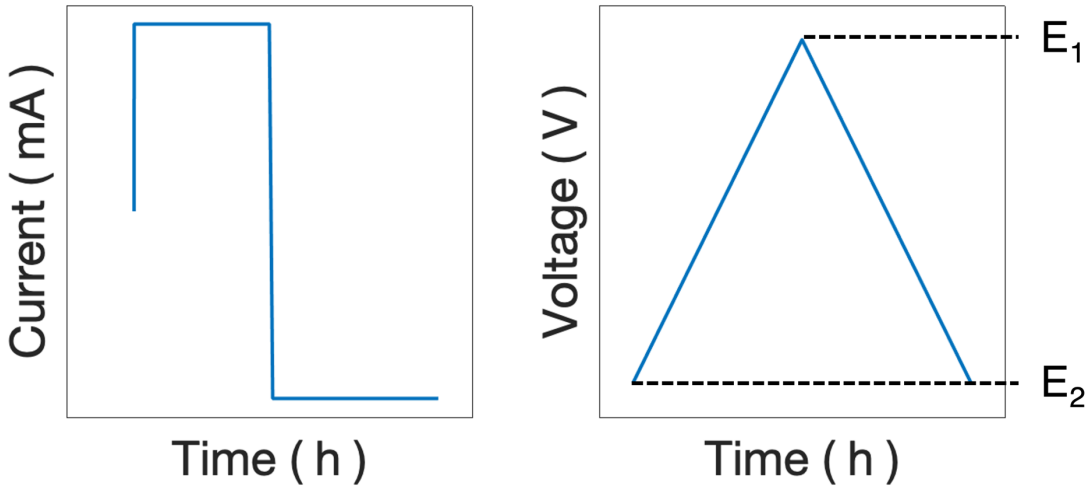

Figure 19 Schematics showing current and potential control in galvanostatic discharge/charge (left) and potentiodynamic cyclic voltammetry (right).

Typically, cyclic voltammetry reveals redox processes that occur within a system, and as such, it can reveal the reduction potentials at which chemical conversions or intercalation occurs. Data from cyclic voltammetry has current, or current density, plotted as a function of voltage, hence giving a cyclic plot showing successive cycles.

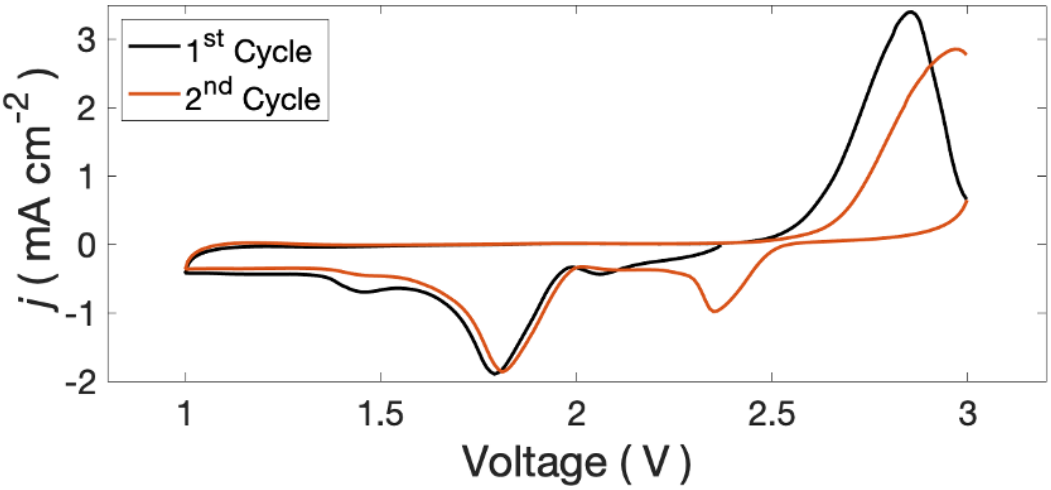

Figure 20 Example of a cyclic voltammogram for a catholyte Li-S system, showing the reduction peaks representing the conversion of S_8 to Li_2S_n (~2.4V) and subsequent conversion to short Li_2S_n chains (~1.8V).

4.2 Physical Characterisation

4.2.1 Raman spectroscopy

Raman spectroscopy is a valuable tool for identifying vibrational modes in materials. First discovered by C.V. Raman in 1928,[143] it is the inelastic scattering of light by matter, showing that there has been a change in energy between incoming and outgoing photons, equivalent to the energy of a vibrational mode.

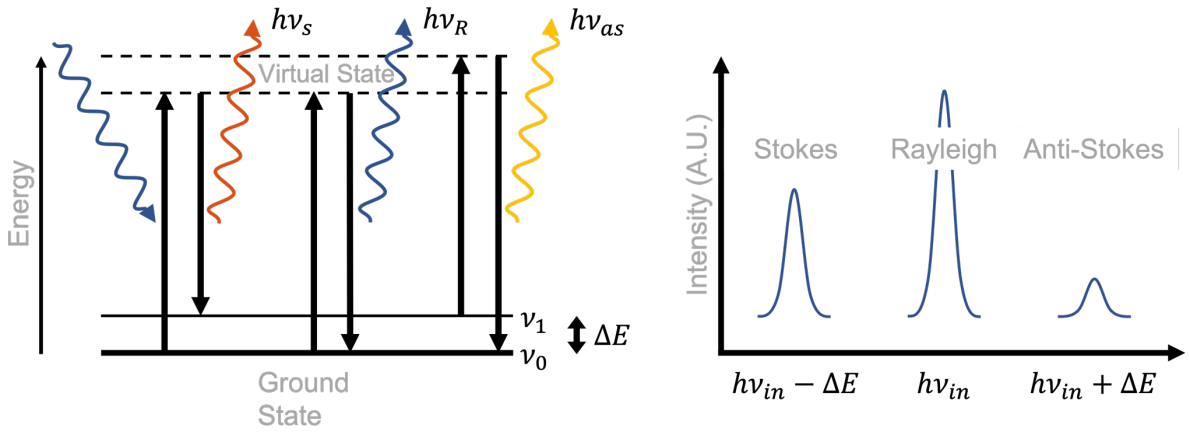

Figure 21 Jablonski Diagram of the Raman Scattering process and related appearance of a spectrum.

In Raman spectroscopy, monochromatic light, frequency υ_L, impinges on a sample. If the energy of this light is lower than the energy needed to change electronic states, then the molecule will be excited to a 'virtual state'. When the molecule decays from the virtual state, a photon will be emitted with an energy $h\upsilon_{in} \pm \Delta E$ with ΔE being the difference in energy between the ground and excited vibrational states, h Plank's constant, and υ_{in} the frequency of incident light. Through this process, we can have three different scattering cases, as seen in Figure 21. The first is Raleigh scattering, where the light is elastically scattered, i.e., the emitted photon has the same energy as the incident photon. The second type of scattering is known as Stokes scattering. Stokes scattering is inelastic scattering where the molecule starts in a ground vibrational state and ends in an excited vibrational state. The energy of the emitted photon is shown by equation (27). This corresponds to light shifted to a lower frequency compared to the frequency of the incident light.

$$h\upsilon_s = h\upsilon_{in} - \Delta E \tag{27}$$

The third type of scattering is anti-Stokes scattering. Here the molecule starts in an excited vibrational state and ends in the ground state. The energy of the emitted photon is shown by equation (28), this corresponds to light shifted to a higher frequency compared to the frequency of the incident light.

$$h\upsilon_{as} = h\upsilon_{in} + \Delta E \tag{28}$$

In both Stokes and anti-Stokes scattering, the ΔE is due to the vibration's energy in the investigated material. In a bond, the frequency of the vibration is dependent on the mass of the atoms as defined by the reduced mass:

$$\mu = \frac{m_1 m_2}{m_1 + m_2} \tag{29}$$

Once we know the reduced mass and the bond force constant (bond strength) of a given molecule, we can calculate the vibrational frequency:

$$\nu = \frac{1}{2\pi}\sqrt{\frac{k}{\mu}} \tag{30}$$

Vibrations can be symmetric and anti-symmetric, depending on the motions of the atoms involved in the vibration. Moreover, vibrations are divided into stretching (vibration in the same direction of a chemical bond), bending (oscillation that implies a change of angle between two atomic bonds), rocking (oscillation that means a difference of angle between a group of atoms), wagging (change in angle of the plane of a group of atoms), twisting (change in angle of the planes of two groups of atoms). For a vibrational mode to be Raman active, there needs to be a change in polarizability as the molecule vibrates, described by:

$$\mu_{ind} = \alpha E \tag{31}$$

Here, μ_{ind} is the induced dipole, α is the polarizability of the molecule, and E is the electric field; we need this polarizability to generate time-dependent dipole moment, which is crucial to the Raman effect. For a complete description of Raman spectroscopy, please see the text by *Larkin*.[144]

Operando Raman Spectroscopy

Combined with a commercially available cell from EL-CELL, *operando* Raman measurements were made using a confocal experimental configuration. In confocal measurements, scattered photons are only collected from the focal plane, meaning that specific points as a function of depth in the cell can be probed (e.g., electrolyte or the surface of materials in the cell).

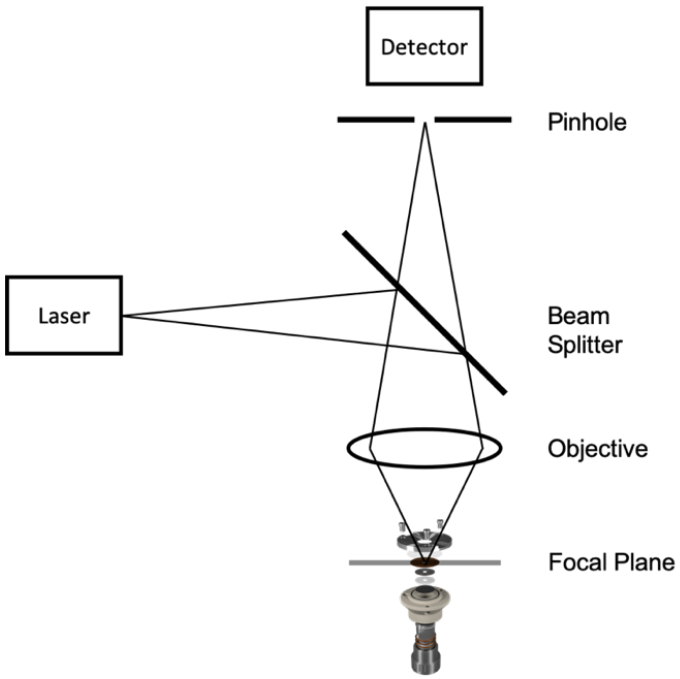

Figure 22 Schematic of confocal Raman experimental setup.

Using the cell shown in Figure 23, it is possible to collect Raman spectra during battery cycling, i.e., *operando* Raman experiments. Raman spectroscopy is particularly well suited to perform *operando* measurements on batteries due to its non-destructive nature allowing data acquisition over multiple cycles, and the speed of acquisition makes it compatible with applicable discharge/charge rates, with acquisition times < 60 s. The spot size of the incident laser when using an x50 objective is ϕ = 2.4 μm, demonstrating the small region Raman spectroscopy probes. Previous studies have used Raman spectroscopy to probe polysulfide speciation, used similarly designed cells with long discharge and measurement times.[114,127]

The cell used in this thesis work allows cyclic voltammetry or constant current charge/discharge experiments to be performed in conjunction with Raman. Figure 23 shows the design and components arrangement of the cell as used in Papers I and III.

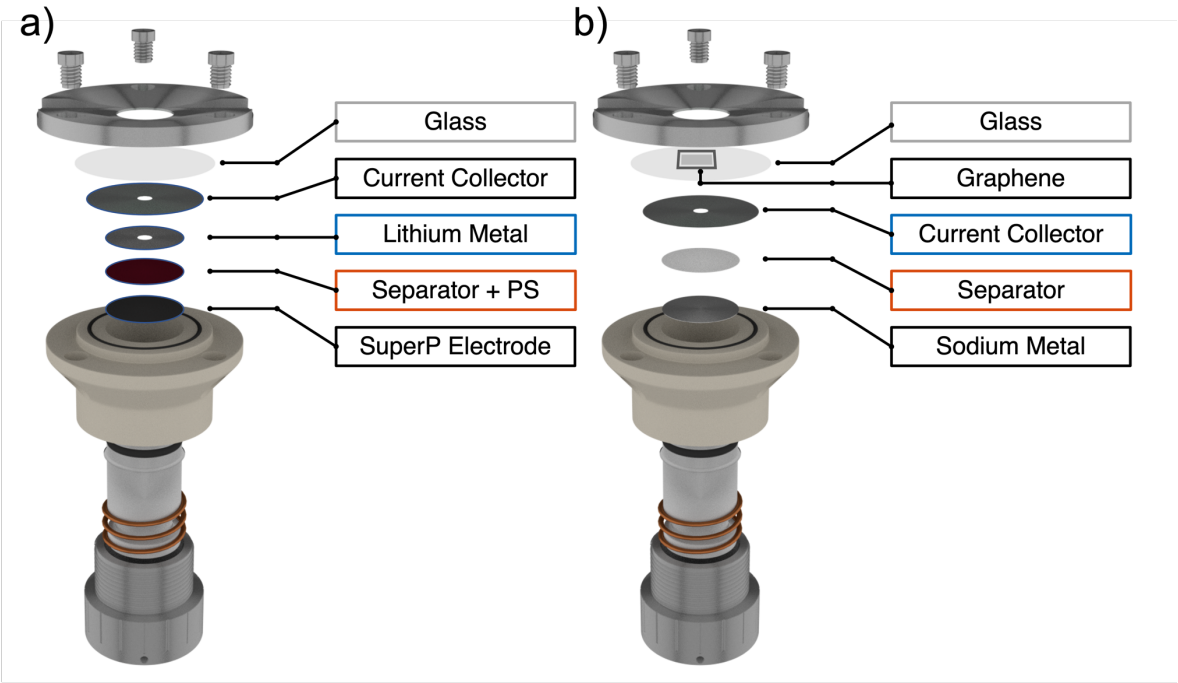

Figure 23 Design and electrode format in the cell used for *operando* Raman measurements. From the bottom up a) SuperP electrode, glass fibre separator with catholyte, lithium metal, nickel foil current collector, glass window. b) sodium metal, separator with electrolyte, nickel foil current collector, graphene coated on a glass window.

Operando measurements are often accompanied by trade-offs that affect performing measurements on a dynamic system. Usually, the cell used has a higher internal resistance, which affects the voltages seen for a given process. The cell has to be designed in such a way that the materials being probed are close to the optical window, meaning that usually, only one component of the cell can be analysed in a given measurement. In terms of measurements, spectra must be recorded rapidly to accurately represent the cell chemistry at a given point during cell discharge/charge. In addition, the laser wavelength and intensity must be carefully selected to suppress fluorescent background effects and not heat cell components. These aspects are often in competition with trying to obtain an acceptable signal to noise ratio and will vary from system to system.

4.2.2 X-ray Tomographic Microscopy

Computed X-ray Tomography (CT) has been used since the 1970s. Today it is a standard tool for medical diagnosis, where it produces 'cuts' (tomograms), detailed images that allow clear differentiation of tissue, air, fluid, and bone in 3-dimensions. Due to the revolution of diagnosis and treatment that the implementation of CT introduced, Allan Cormack and Godfrey Hounsfield received the 1979 Nobel Prize in physiology and medicine.[145] Today, computed tomography is used in a highly diverse range of fields, from medicine to archaeology, quality control and pharmaceuticals.

X-ray Tomographic Microscopy (XTM) is an incredibly powerful tool that has been used in multiple studies to monitor changes to electrode microstructures in a range of battery chemistries, from Li-ion,[146] to Li-S,[116,122] and even Li-air.[147] It relies on the absorption of x-rays by matter, with phases composed of different elements differing in how much they absorb, providing 'absorption contrast'. Therefore, different phases in a sample can be identified in 3-dimensions. In batteries, these phases can include particles making up the electrode microstructure. In the example of Li-ion batteries, individual SnO particles have been imaged to track the formation of cracks and the subsequent mechanical degradation.[146] On larger scales, entire electrodes of cylindrical cells can be imaged, proving unique insights into the heterogeneity of Li insertion and the degradation mechanisms on the cell level.[7]

Computed tomography has now been applied at synchrotron X-ray sources,[148,149] which bring inherent benefits of high flux beams, whose energies can be easily tuned and monochromated, an important feature needed to provide optimum imaging of a given system. However, one of the most important features of a synchrotron x-ray source is that the beam is highly parallelised, allowing the effective imaging of cell components and interfaces, even ones close to the surface of highly attenuating materials, such as metals.

XTM, just like radiography, relies on the attenuation of x-rays by matter, how much the intensity of an incoming x-ray beam is attenuated depending on the composition of a given material. The attenuation of x-rays through a given medium is described by Beer-Lamberts law:[150]

$$I(d) = I_0 e^{-\mu d} \tag{32}$$

where I is the measured x-ray intensity, I_0 is the initial x-ray intensity, μ the absorption coefficient, and d the sample diameter. Attenuation is a combination of absorption and Compton scattering,[151] with the photoelectric absorption coefficient being the dominant process and described by the following equation:

$$\mu = \frac{\rho Z^4}{AE^3} \tag{33}$$

where ρ is the density, Z is the atomic number, $A\ the\ atomic\ mass$, and E the x-ray energy. Equation (33) shows that each element will absorb x-rays by varying amounts. Leveraging this property allows different elemental phases in a sample to be distinguished, as demonstrated in Figure 24.

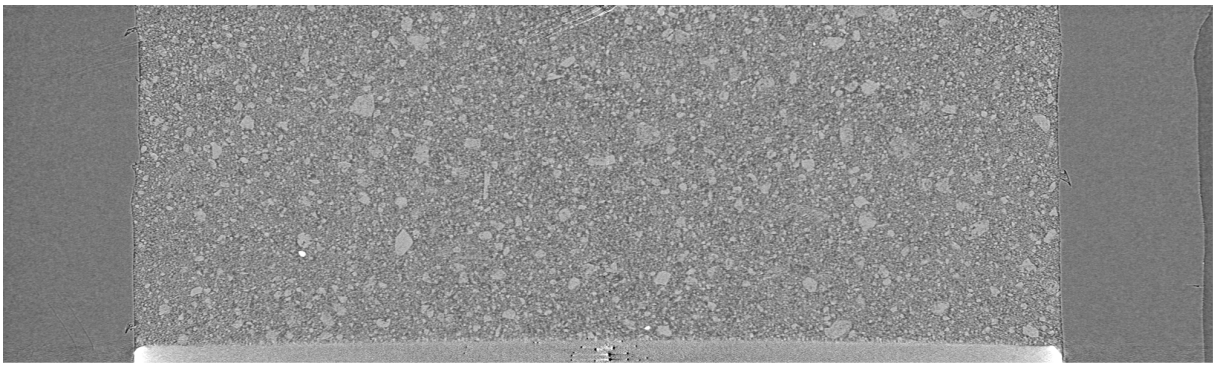

Figure 24 A slice through a tomogram of a solid electrolyte cell, with bright and dark structures representing different phases in the material with varying electron densities.

Figure 25 shows a typical set up for an XTM experiment. After penetrating the sample, attenuated x-rays arrive at the detector and produce a projection which is a 2D image that shows the transmission of x-rays. The regions with higher x-ray transmission will appear lighter in the projection, and the regions with more x-ray absorption will be darker.

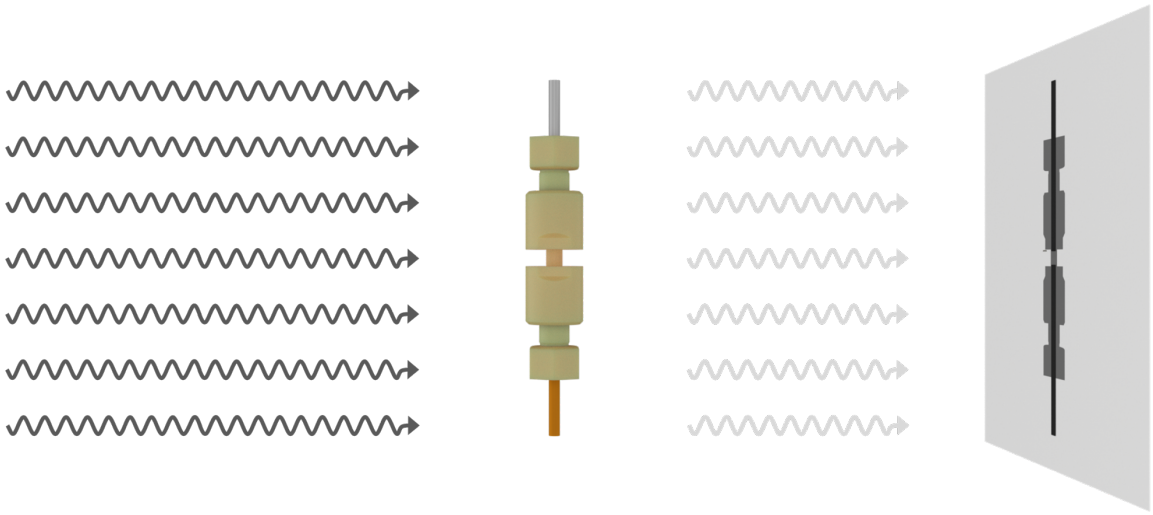

Figure 25 XT set up. In-coming x-rays (I_0, black), attenuated by a sample to produce transmitted x-rays (I, grey). On the right is the projection. Light elements that make up the plastic casing appear as grey, and heavier elements that make up the stainless steel and copper pins appear as black.

In the case of XTM, where spatial resolutions of ~1 µm can be achieved, there are a few more steps in the process before the projection is acquired. First, the attenuated x-rays pass through a scintillator, converting the x-rays into visible light, which is then magnified by an objective before being measured by a CCD detector. The detector comprises an array of pixels, with each pixel having a length of 6.5 µm. Applying an x20 objective means that each pixel on the detector represents a 0.0325 µm x 0.325 µm region of the sample (Figure 26). The detector area represents the total area of a sample that can be measured, the field of view (FOV). Taking the example of a detector that is 2560 pixels in width and 2160 pixels in height, if the x20 objective is used to produce a pixel size of 0.325 µm, then the FOV would be ϕ = 832 µm (832 µm x 702 µm).

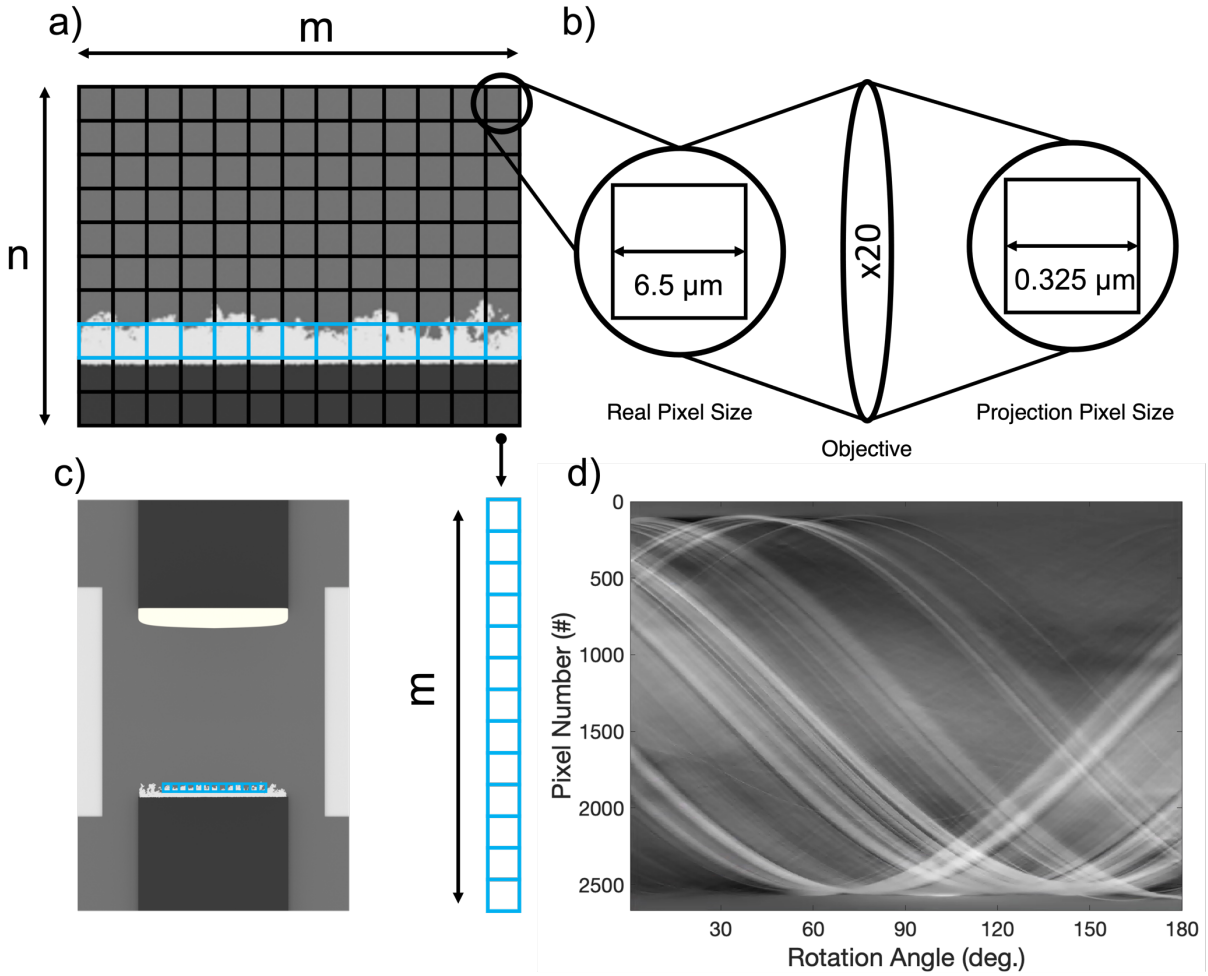

Figure 26 a) Schematic of a CCD detector pixel array, b) relationship between real pixel size and projected pixel size, c) example projection of cell with a row of CCD detector pixels marked d) demonstration of a row of pixels forming a sinogram.

Where XT indeed differs from radiography is in the methodology used to create 3-dimensional datasets. The sample is rotated from 0 - 180°, and at a given rotation step, a projection is measured. With 1000 projections being taken, an angular step of 0.18° per projections is required. As the sample is rotated, the transmission of x-rays recorded in each projection to form the Radon transform, a series of line profiles collected from all angles, otherwise known as a sinogram. A sinogram is produced for each row of pixels on the detector, i.e., for the 2560 x 2160 pixel detector, 2160 sinograms would be produced, each with dimensions of 2560 pixels and 180 degrees (Figure 26).

Once the sinograms have been acquired, tomograms are reconstructed from them. In XTM, a standard reconstruction method is Filtered Back Projection (FBP),[152] which can be split into two aspects. The first step in this process is filtering. Intensity profiles from the sinograms are Fast Fourier Transformed, converting them to the frequency domain. All the 1D line profiles collected over many angles build up a sample representation in a 2D Fourier domain. However, a bias is created for low frequencies, resulting in the reconstructed image looking blurred and unsharp (Figure 27). It has been shown that an edge enhancing filter can suppress the low frequencies and sharpen the image.[152] The second step is back projection, the process where an image is created by taking the filtered line profiles to reconstruct the original system under investigation.

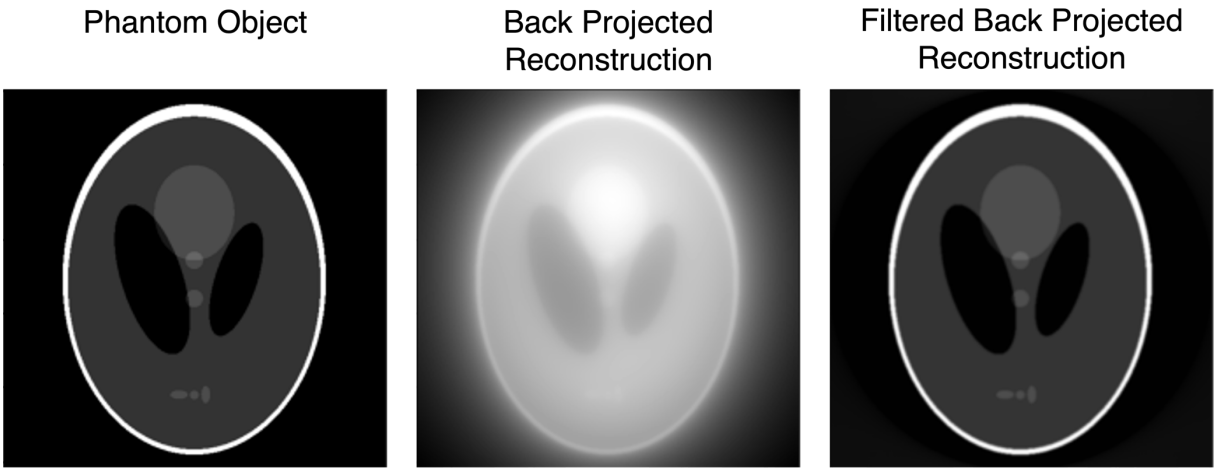

Figure 27 An example of a Shepp-Logan phantom image, the back-projected reconstruction of the phantom image with no filtering, and the back-projected reconstruction with filtering.

Once the tomograms have been reconstructed, each represents a single pixel thick ‘slice’ of the sample. Combining all the slices provides a discretised representation of the 3D volume, with the original sample now represented by voxels, volumetric pixels. Though FBP is a versatile method widely used at XTM beamlines, alternative methods exist that can further refine reconstruction results at the expense of computational power.[153]

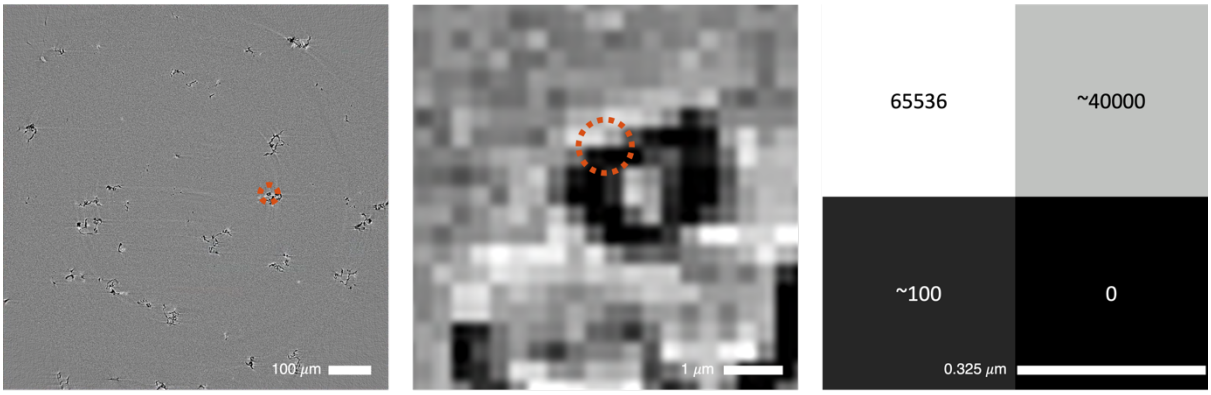

Figure 28 A tomogram from the sample. Each subsequent image shows a zoomed-in region from the previous image. The figure demonstrates how each image is an array of greyscale voxels. Each voxel holds a numerical value that is proportional to the x-ray absorption within that voxel.

Each voxel has a greyscale intensity, and this greyscale intensity represents the absorption of x-rays in that voxel, and as such, provides information on the local differences in electron density in a sample, so-called absorption contrast. Higher intensity voxels represent higher absorption and vice versa. By selecting specific greyscale values, individual phases can be isolated in the tomograms, a process known as segmentation. Once segmentation has been performed on a given phase, it can be analysed, providing quantitative volumetric data.

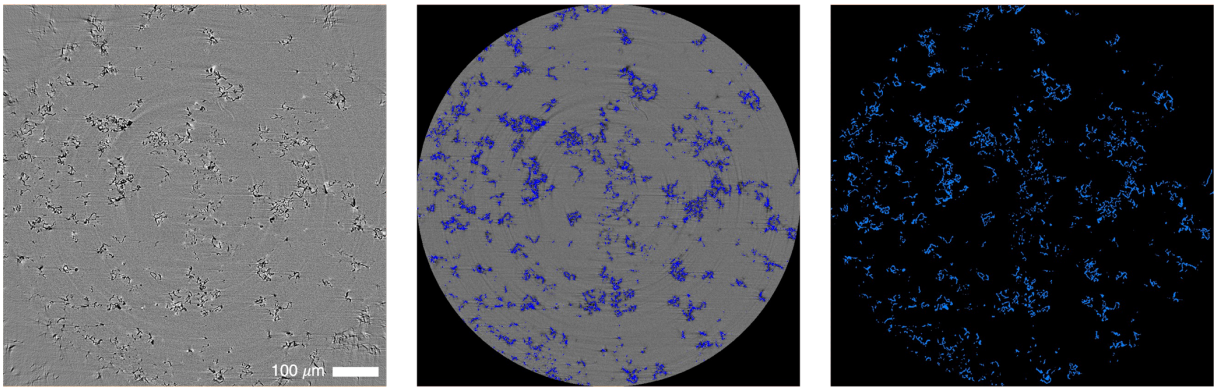

Figure 29 Segmentation process of tomographic data. Left, the original tomogram. Middle, pixels with a specific greyscale value. Right, binary image showing the segmented data.

Often in XTM, absorption contrast is not sensitive enough to differentiate phases. However, the sensitivity can be enhanced using in-line propagation phases contrast.[151] As x-rays pass through a sample, they are not only absorbed but also refracted, with the interaction being described by the complex refractive index n:

$$n = 1 - \delta + i\beta \tag{34}$$

where δ is the refractive index decrement, and β the absorption index. Thus as x-rays pass through the sample, the propagating wave with a phase shift will interfere with waves that have not been shifted, leading to fluctuations in intensity.[151] Such enhancement and phase contrast can be obtained during the reconstruction process utilising algorithms to produce so-called paganin reconstructions.[154] Phase-contrast imaging can be useful when materials within a sample have similar attenuation coefficients, giving poor absorption contrast, or in samples that may be rapidly degraded by the x-ray beam[151], making this Paganin phase retrieval a useful tool to complement absorption data.

When employing XTM, the overall workflow for making measurements and generating a full 3D image is usually:

- Measurement, projections are acquired, and the data is converted to sinograms.
- Reconstruction, tomograms are created from the reconstruction of sinograms.
- Segmentation, tomograms are then segmented to separate individual phases.
- Analysis, once a phase has been segmented, multiple forms of analysis can be performed, including calculating the volume, surface area, etc.

Operando X-ray Tomographic Microscopy Cells

The XTM measurements in this thesis utilise two types of cells, a glass capillary cell and a polyether ether ketone (PEEK) cell. Both had their inherent benefits and flaws. Crucial characteristics of the XTM cells are that they can effectively seal the internal environment to prevent the ingress of water and oxygen. They have low x-ray attenuation, but most importantly, the material must be homogenous to enable high-resolution XTM experiments. The materials used for the cell must have chemical stability against cell components such as lithium metal and electrolyte. Finally, cells should have a good electrochemical performance to ensure that cell performance is relevant within the battery materials research field.

The glass capillary cell used was 0.7 mm in diameter. The entire electrode could fit within the FOV of the XTM measurements, enabling global tomography and quantitative analysis on the electrode structure, such as correlative analysis with electrochemical data. The glass itself was x-ray transparent, meaning it caused minimal x-ray attenuation but also transparent to visible light, allowing optical analysis of the electrolyte during cell cycling. Disadvantages of the cell were that it was very delicate, resulting in a complex assembly procedure. In addition, the cell design resulted in a large electrolyte volume which may impact the electrochemical performance.

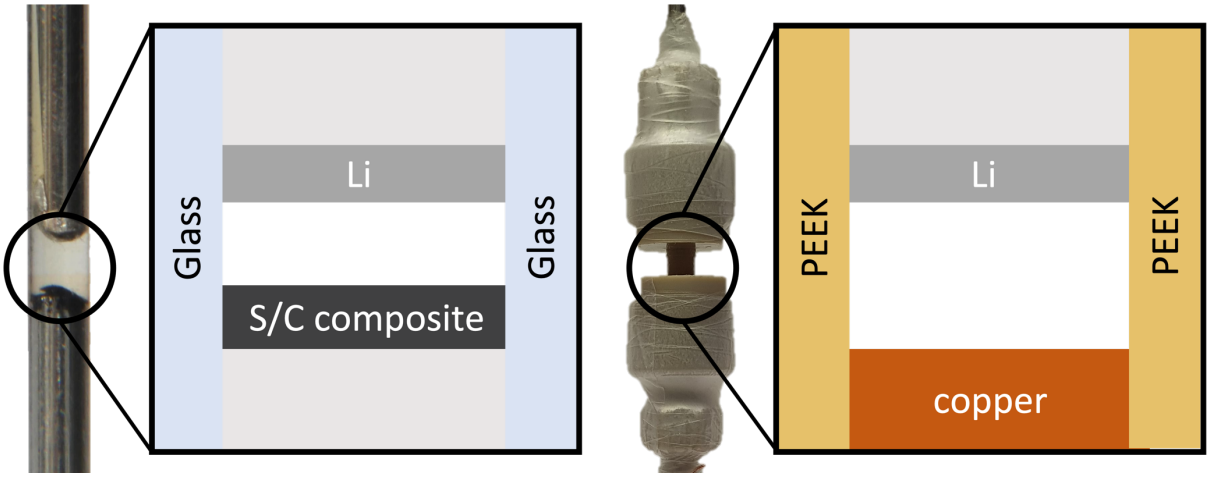

Figure 30 Cells used for XTM measurements (not to scale) in Papers IV and VII. The glass capillary cell is shown on the left, and the PEEK cell is shown on the right.

The second cell used was a cell made from PEEK. This cell came with the benefits of reliable sealing and a relatively simpler assembly procedure. However, it had a larger diameter of 1.58

mm, meaning that not all of the electrode area sat within the FOV, making quantitative analysis of the electrode challenging.

An essential consideration for both cells was that they had small diameters (0.7 mm and 1. 58 mm respectively), with the materials to be imaged within 100-200 µm of the electrode surface. To perform quantitative analysis on these materials, their entire depth would need to be imaged, allowing the identification of changes at the electrode surface. This was of particular importance in the case of the Li-plating experiment. Synchrotron sources can accommodate such experiments, as the parallel beam geometry can traverse the electrode surface with little or no interaction with highly attenuating materials, such as Cu. This would not be the case with a cone-beam geometry since the region with a few micrometres of the electrode surface would suffer from high interference. The absorption contrast would be reduced, rendering investigations of surface processes near impossible.

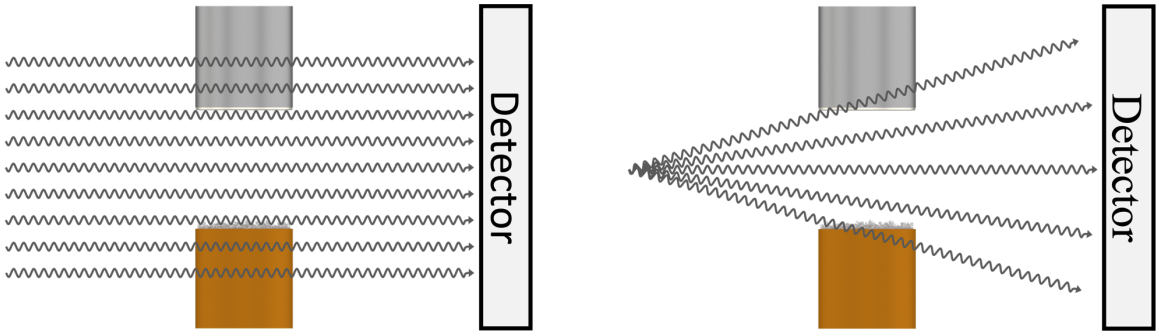

Figure 31 Demonstration of the importance of a parallel beam geometry. When imaging materials that sit close to the surface of highly attenuating materials, in this case, Cu, a conical beam would not pass through the material. This would lead to the region close to the materials surface experiencing a high degree of interference.

5 Results and Discussion

5.1 Intercalation of Na^+ in 'Janus' Graphene

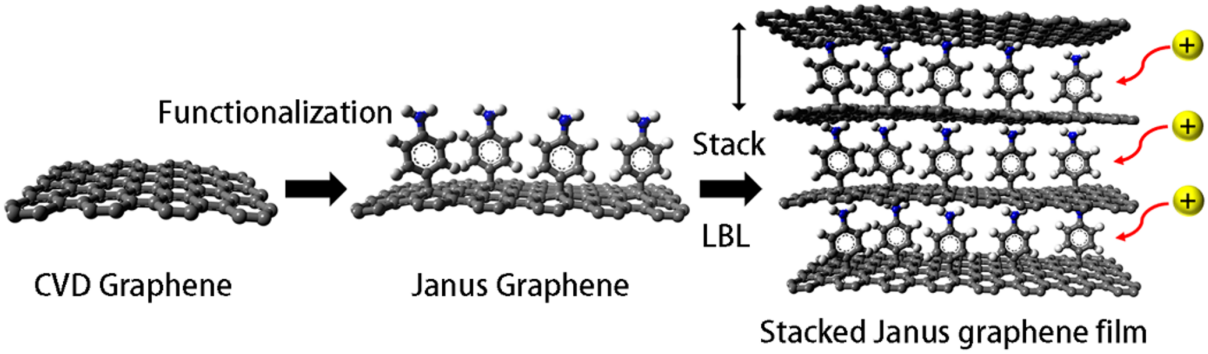

Figure 32 Schematic showing the one-sided functionalisation process resulting in the stacked Janus graphene film. Figure 1 from Paper I reproduced under Creative Commons Licence.

In this work, CVD graphene was functionalised with amino-benzene on one side to form what is known as 'Janus' graphene (AB-graphene).[51] This Janus graphene was then stacked to create the Janus graphene film, a novel methodology for tailoring the properties of graphitic structures (Figure 32). In this case, tailoring the material to store Na^+ efficiently. With the novelty of this material comes a lack of understanding of its energy storage mechanism.

To confirm whether the energy storage mechanism was the intercalation of Na^+ in the Janus graphene layers, Raman spectroscopy was used to monitor the characteristic G-band of graphene sheets. The G-band represents the in-plane vibrations of sp^2 bonded carbons in the graphene sheets. Previous studies have shown the sensitivity of the G-band in graphite to Li^+ intercalation,[155] whereby the wavenumber of the observed peak increases in the initial stages of intercalation, and then the band splits, reflecting multiple phases forming at later stages of intercalation.

Using Raman spectroscopy to probe the G-band of the Janus graphene, a similar shift in wavenumber is observed as the cell voltage decreases (Figure 33a). However, as opposed to previous studies with Li, no splitting of the G-band was observed. This suggests there was intercalation into a single stage and that intercalation proceeded simultaneously in all graphene sheets.

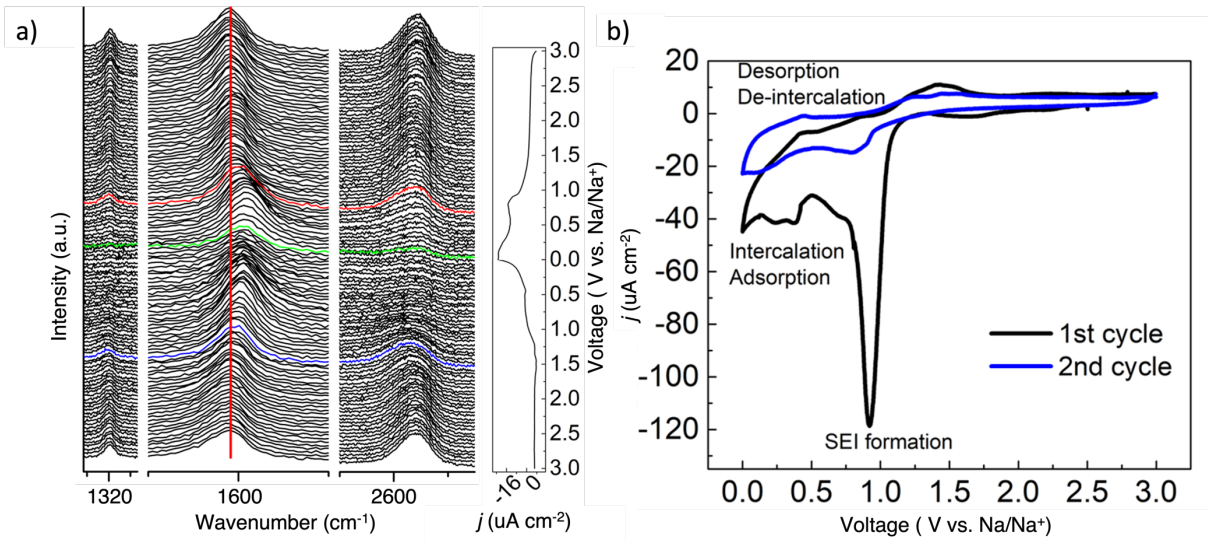

Figure 33 a) *Operando* Raman spectra acquired during a complete intercalation/deintercalation cycle of Na^+ in AB graphene; the red spectrum was measured at ca. 0.6 V, green spectrum at 0.05, and blue spectrum at ca. 1.5 V. The solid red line marks the position of the G-band b) CV curves measured during the first two cycles of Na^+ intercalation in AB graphene with a scan rate of 0.042 mV/s. Figure 5 from Paper I reproduced under Creative Commons Licence.

Raman spectroscopy is also used to determine the reversibility of the intercalation process, Figure 33b. In the 1st cycle, a sizeable cathodic peak can be observed at 1 V in the CV taken during the Raman experiment. This peak is not observed in subsequent cycles, and it is associated with the formation of an SEI.[156] Figure 33, shows an increase in wavenumber of the G-band during intercalation of the first cycle. However, after deintercalation, the original peak position value is not found. This suggests the formation of the SEI interacts with the sp^2 carbon vibrations, slightly shifting the G-band. The intercalation appears to be completely reversible in subsequent cycles, with the G-band returning to its pre-intercalation position after intercalation and deintercalation for cycles 2, 3, and 4.

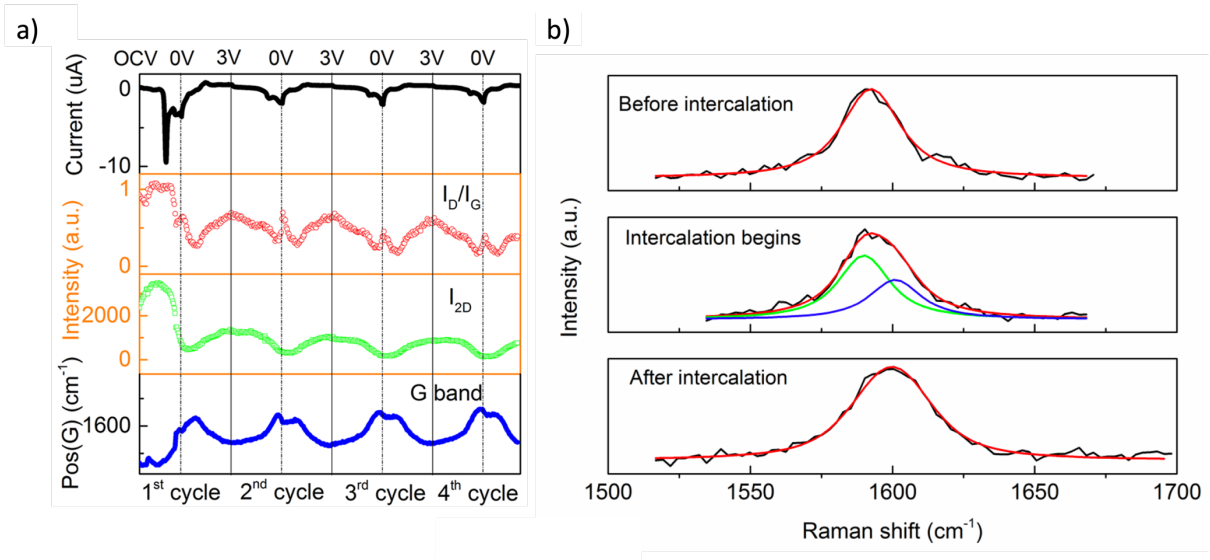

Figure 34 a) Change of parameters during cycling: from top to bottom, the measured current, I_D/I_G ratio, the intensity of 2D band (I_{2D}), and position of G band. b) Raman spectra of G-band during Na^+ intercalation in NB-graphene with associated fits. Figure 5 from Paper I reproduced under Creative Commons Licence.

To confirm the presence of the amino benzene groups were critical to the intercalation of Na^+, the process was compared between highly ordered pyrolytic graphite (HOPG), unfunctionalised CVD graphene, AB functionalised graphene, as well as with Li^+. An apparent increase in wavenumber is observed for all three materials when Li^+ is intercalated, in line with previously reported results for graphite.[155] However, when the experiments were repeated with Na^+, an increase in the G-band wavenumber was only observed for the AB-graphene.

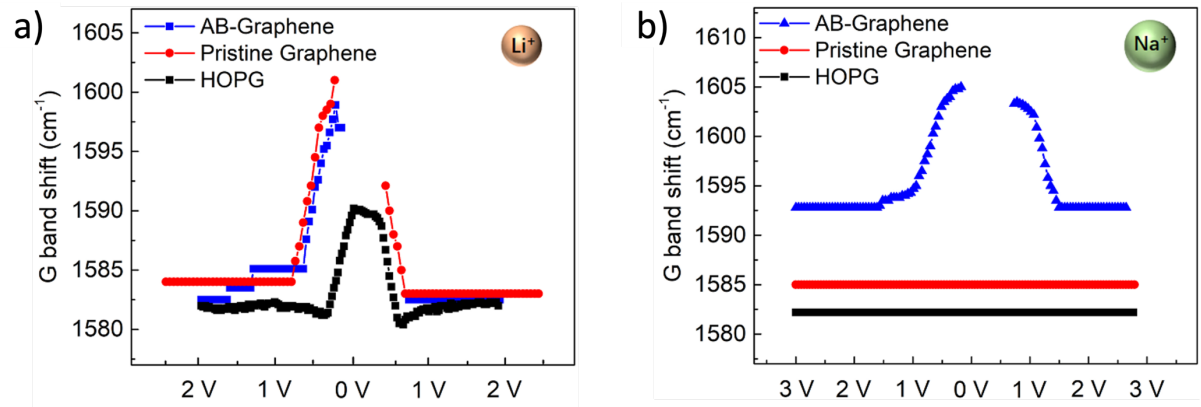

Figure 35 Comparison of Li^+ and Na^+ intercalation in different materials. a) Shift of the G-band position during Li^+ intercalation in highly ordered pyrolytic graphite (HOPG), graphene, and AB graphene. b) Shift of G-band position during Na^+ intercalation, Figure 4 from Paper I reproduced under Creative Commons Licence.

The combination of the novel ‘Janus’ graphene material and *operando* Raman spectroscopy have shown that graphitic structures can be tailored in a bottom up approach to improve the interaction with graphene. The interaction between graphene and Na^+ can then be confirmed via Raman spectroscopy. The material was capable of forming the $NaC_{6.9}$ compound, but further tuning of the interaction could create higher capacity materials.

Raman spectroscopy was a useful tool in this experiment for confirming the intercalation process and its reversibility. Figure 23b shows the cell configuration for this experiment. The graphene could be readily measured since it was deposited directly on the glass window. However, this configuration induced a large cell polarisation. The experiment was also spatially limited, with the region being probed was only a few μm^2, in comparison to the dimensions of the electrode (mm^2).

5.2 Dissolution, Migration, and Precipitation Processes in Semi-Liquid Li-Sulfur Cells

Lithium sulfur cells using liquid electrolytes rely on the dissolution and precipitation of lithium polysulfide species. To achieve high active materials utilisation, and good kinetics of sulfur conversion, polysulfide conversion must take place in the liquid state. However, the formation of soluble polysulfide species will result in them diffusing out of the cathode structure and through the entirety of the bulk electrolyte, leading to active material loss and capacity decay. One approach to tackle the dissolution of the active material is the application of a catholytes. Catholytes are an approach where the active material is dissolved directly in the electrolyte, their use has been shown to stabilise the Li-metal interface,[85] buffer the dissolution of sulfur in the cathode,[84] and increase the energy content of cell by introducing additional sulfur, raising the effective sulfur loading.

In Paper I, a catholyte was applied to a nanostructured CMK-3 and sulfur composite cathode. The use of the catholyte buffers the dissolution of sulfur as shown by the coulombic efficiency of 99% and retention of 80% capacity after 500 cycles as demonstrated in Figure 36a.

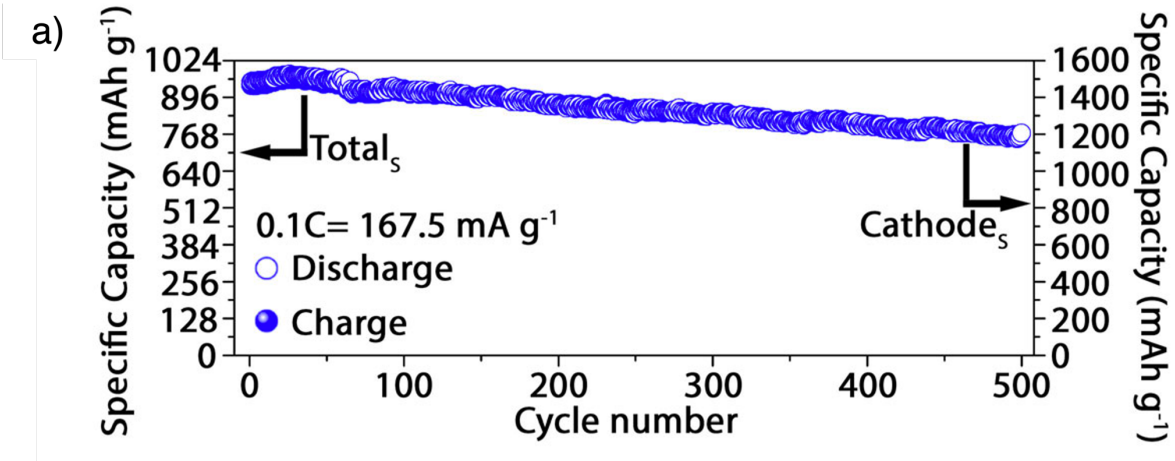

Figure 36 a) Prolonged cycling performance of the CMK3/S electrode in Li–S cells using DOL/DME–0.4M $LiNO_3$–0.5M Li_2S_8 electrolyte at a current rate of 0.1 C=167.5 mA g^{-1}. Figure 4 from Paper II, reproduced with John Wiley and Sons permission.

Not only can catholytes be used as an electrolyte to buffer sulfur dissolution, but they can also be used with sulfur-free cathodes. Previously this combination has achieved stable cycling over

multiple cycles.[92] Figure 37a shows discharge capacities from galvanostatic cycling of Li-S cells with the two catholytes, with and without Li-salt (LiTFSI).

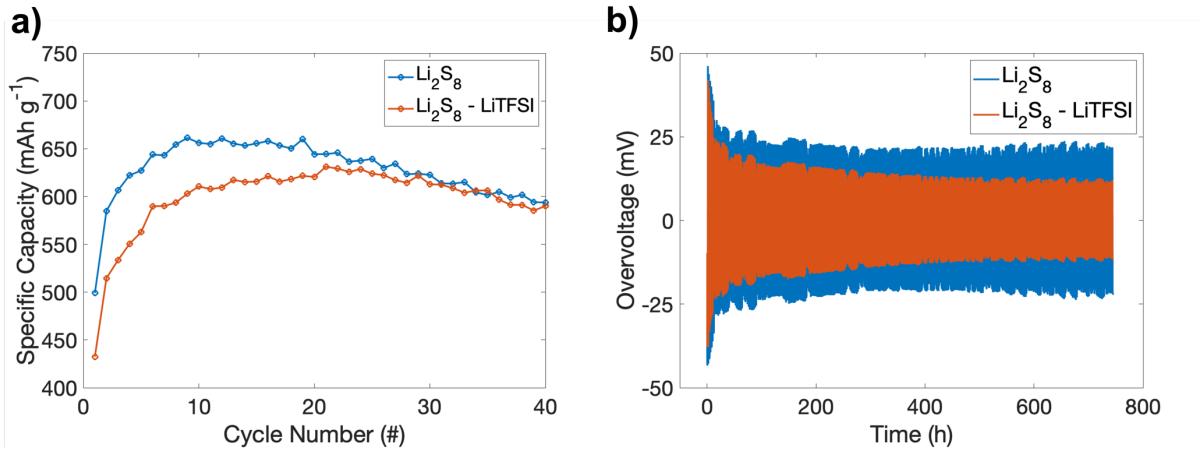

Figure 37 a) Comparison of discharge capacities for both catholytes. b) Li plating/stripping experiment in symmetric Li/Li cells (0.1 mA cm^{-2}) for both catholytes.

The cell using the Li_2S_8 catholyte shows a higher discharge capacity compared to the cell with the Li_2S_8-LiTFSI catholyte (Figure 37b), i.e., the active material utilisation is higher. Even with the active material, sulfur, dissolved in the electrolyte, the cell's operation relies on the effective diffusion of polysulfide species to and from the cathode to utilise all active material in the catholyte.

Operando Raman spectroscopy is a tool capable of providing chemical information on changes in the catholyte. With such information the sulfur speciation in the catholyte can be monitored during cell cycling, providing information on the chemical pathways of discharge, while also providing information on the migration and mobility these same species.

In Paper III *operando* Raman spectroscopy was used to compare sulfur speciation in the two catholytes to gain insight into the varying performance of the two systems. Raman spectra were collected from a small close to the Li-metal anode surface, thus monitoring species that had diffused from the cathode to the anode during cycling. Figure 38a shows the Raman bands for the Li_2S_8 catholyte. Two Raman bands were monitored, 372 cm^{-1} assigned to long chain polysulfide species (S_8^{2-}), and 535 cm^{-1}assigned to the tri-sulfur radical (S_3^{*-}). Here the band corresponding to long-chain polysulfides increases during the final stages of the 1st charge and reaches a maximum during the 2.4 V plateau of the 2nd discharge, showing a significant delay

in observing the species at the anode compared to their formation in the cathode. In the case of the Li_2S_8-LiTFSI catholyte, the maximum of the band corresponding to long chain species occurs even further into the 2nd discharge, close to the end of the 2.4 V plateau. Suggesting a slower conversion or diffusion of species. The slower diffusion would agree with a lower mobility of the polysulfide species due to increased catholyte viscosity presented in Paper III.

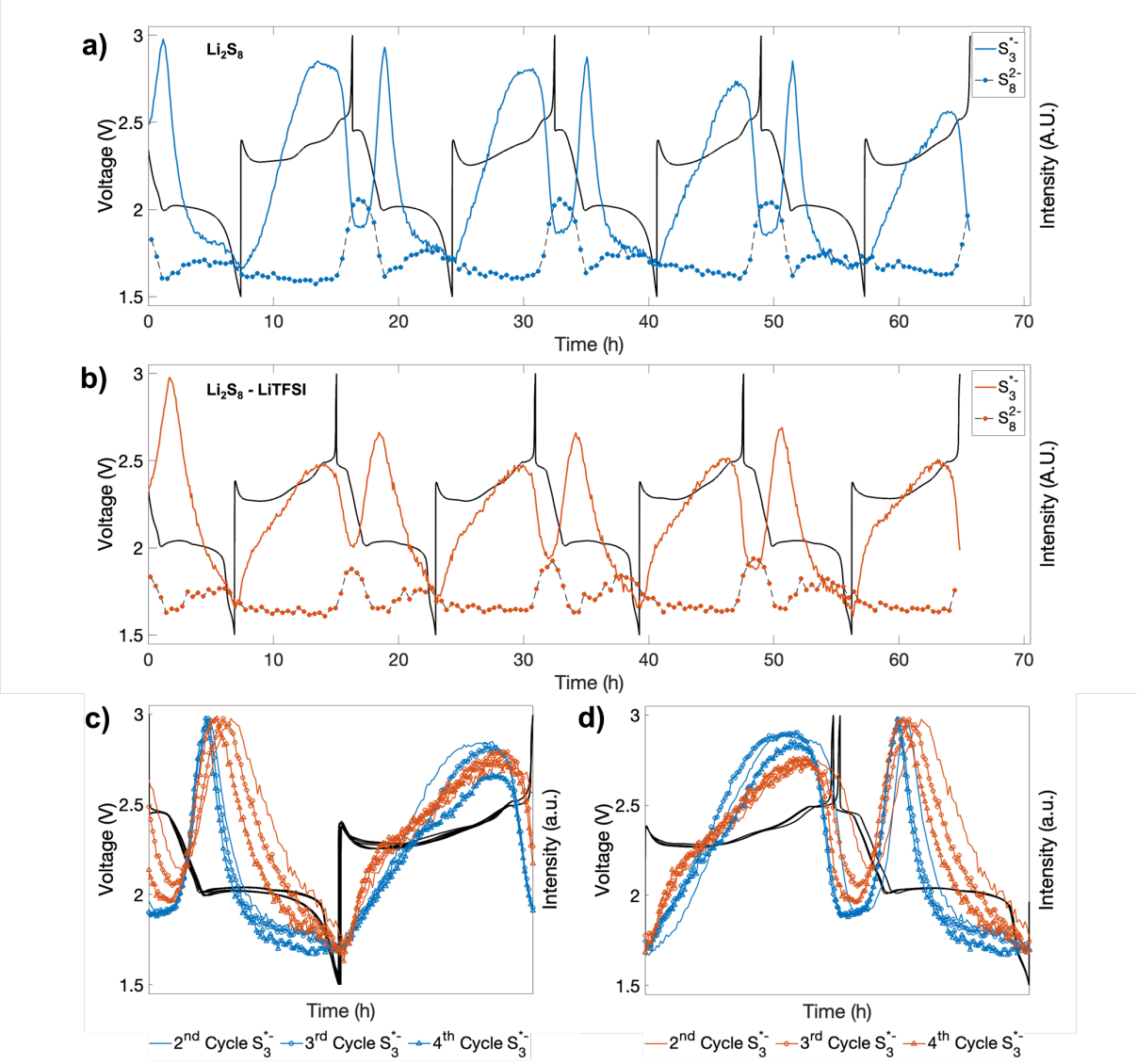

Figure 38 Intensity of 372 cm^{-1} (S_8^{2-}) and 535 cm^{-1} (S_3^{*-}) bands and voltage profiles over 4 cycles for the a) Li_SS_8 catholyte (blue) and b) Li_2S_8-LiTFSI catholyte (orange). Intensities of the S_3^{*-} band and voltage profiles of each cycle overlaid and normalised to the maximum discharge and charge times for the Li_SS_8 catholyte (blue) and Li_2S_8-LiTFSI catholyte (orange) with c) a discharge/charge alternance and d) a charge/discharge alternance.

The evolution of the intensity of the S_3^{*-} band intensity and the corresponding voltage profiles are overlaid and normalised to the charge/discharge times to directly compare the two cells' behaviour across multiple cycles (Figure 38c and d). The Li_2S_8 catholyte (Figure 38c) shows the S_3^{*-} band intensity maximum seen during discharge for the 2nd, 3rd, and 4th cycles appears at the same depth of discharge, and the intensity increase starts at the same depth of discharge. However, for the Li_2S_8-LiTFSI catholyte, the intensity maxima are observed progressively earlier in the discharge. Figure 38d shows the same analysis but with a charge/discharge alternance. This delay in the maxima positions seen in the Li_2S_8-LiTFSI catholyte, and their subsequent shift, suggests that polysulfide mobility in the electrolyte changes with each cycle. Thus, the difference in the position of the maxima between the two catholytes directly reflects the migration of polysulfides. It can be surmised that the higher mobility of polysulfide species is directly related to cell performance, consequent of more efficient polysulfide conversion at the cathode.

Operando Raman spectroscopy proved to be a valuable tool in determining sulfur speciation in a catholyte. However, it was limited by only monitoring species observed at the anode, and only investigating conversions of the soluble polysulfide species. Raman spectroscopy was a well suited to *operando* measurements as spectra were collected in < 60 s, and were acquired frequently, providing detail changes during cell cycling. A future experiment would see this same method applied to cells with a higher C-rate (C/10, or C/5), however challenges with cell resistivity would need to be addressed.

Despite the information on speciation and migration provided by Raman spectroscopy, the cell performance of Li-S cells still relies on the dissolution of sulfur species and precipitation of Li_2S at the cathode. To investigate these processes, XTM was employed to monitor the dissolution and precipitation processes across the entire C/S cathode. The capillary cell presented in Paper IV had a diameter that could place the cathode within the field of view of the XTM measurements, a 'global' tomography measurement. With all sulfur in the cathode measured by XTM, direct correlation was made between the segmented sulfur phase and the electrochemical measurements made.

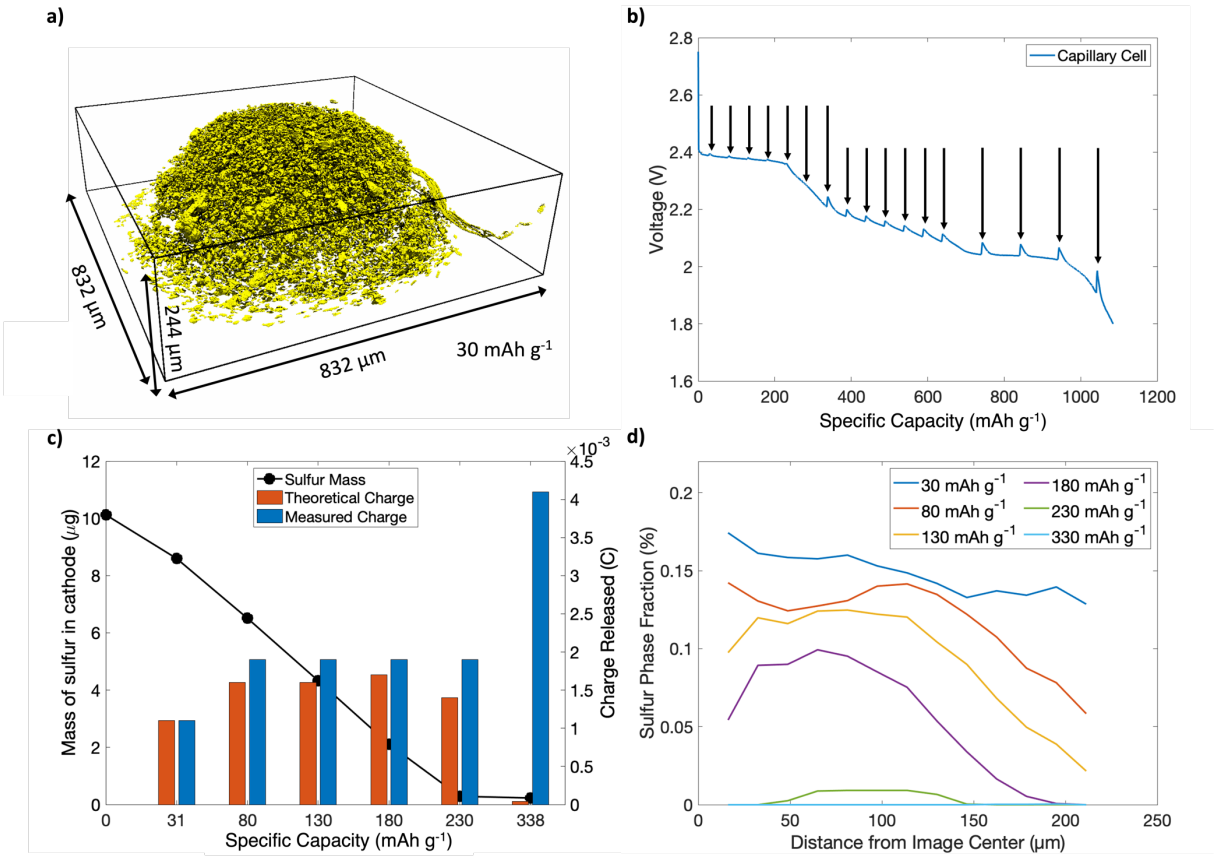

Figure 39 a) Volume renderings of cathode sulfur b) Voltage profile of the Li-S cell discharge with the points marked where XTM measurements were made. c) Total sulfur mass in the cathode as a function of the specific capacity, determined from volume renderings of elemental sulfur (black) and theoretical charge released, calculated from the conversion of elemental sulfur in the cathode determined from the volume renderings (orange) to Li_2S_8 and the actual measured charge between tomograms from the cycling experiment (blue). d) Radial distribution of sulfur within the cathode at different depths of discharge.

Using XTM, all sulfur present in the pristine C/S cathode was imaged and segmented (Figure 39a), allowing a quantitative correlation between the sulfur dissolution and electrochemical performance of the cell during cycling (Figure 39b). Figure 39c shows the total sulfur mass in the electrode, determined from the volume renderings, and directly compares the theoretical charge originating from the conversion of S_8 to Li_2S_8 (blue), based on the tomography data, to the actual charge released by the cell (orange). Between 80 and 230 mAh g^{-1}, more charge is released compared to what is predicted based on the conversion of $S_8 \rightarrow Li_2S_8$ (22). This extra charge observed in the first plateau provides direct evidence that the conversion of long-chain

polysulfide species to shorter chain polysulfides and the conversion of elemental sulfur coincides.

To comment on the impact of sulfur conversion kinetics caused by the simultaneous sulfur dissolution and further polysulfide conversion, Figure 39d shows the radial sulfur phase fraction from a single 2d cut of the cathode, plotted as a function of discharge. This analysis shows that as the discharge progresses, sulfur particles far away from the electrode centre experience a higher dissolution rate, demonstrated by the pronounced drop of the sulfur phase fraction profiles with increasing distance from the centre of the electrode. This behaviour can be rationalised by considering that the electrochemical reaction rate is dependent on the local polysulfide concentration and Li^+ flux to, and in, the electrode. From the surface of the electrode, dissolved polysulfides can diffuse out to the bulk electrolyte, driven by the polysulfide concentration gradient, keeping the local polysulfide concentration relatively low, allowing further polysulfide dissolution. Similarly, the flux of Li^+ from the bulk electrolyte to the cathode ensures that the conversion reactions can be sustained. The local polysulfide concentration will be higher in the centre of the electrode since their diffusion is limited by a longer and less effective diffusion pathway through the carbon-binder matrix. There will also be a lower local chemical concentration gradient and a lower diffusivity due to increased electrolyte viscosity arising from the increased local polysulfide concentration, slowing down sulfur dissolution in the centre of the cathode. This can be seen as a local buffering effect, similar to the effect previously discussed in Paper II in connection to catholytes.

This concept of polysulfide saturation of the electrolyte confirms what is observed with *operando* Raman spectroscopy measurements. The increased polysulfide concentration within the cathode structure increases the electrolyte viscosity, reducing the mobility of species in solution. The results from the Raman spectroscopy demonstrates the catholyte with the lower viscosity has higher mobility of species, with polysulfides diffusing from the anode to cathode, and consequently, improved cell performance.

However, for Li-S cell discharge, the sulfur dissolution and subsequent polysulfide mobility only account for part of the discharge mechanism. XTM was further applied to observe the final stages of Li-S cell discharge and the precipitation of insoluble short chain polysulfide species (Li_2S_2 and Li_2S) and the end of discharge.

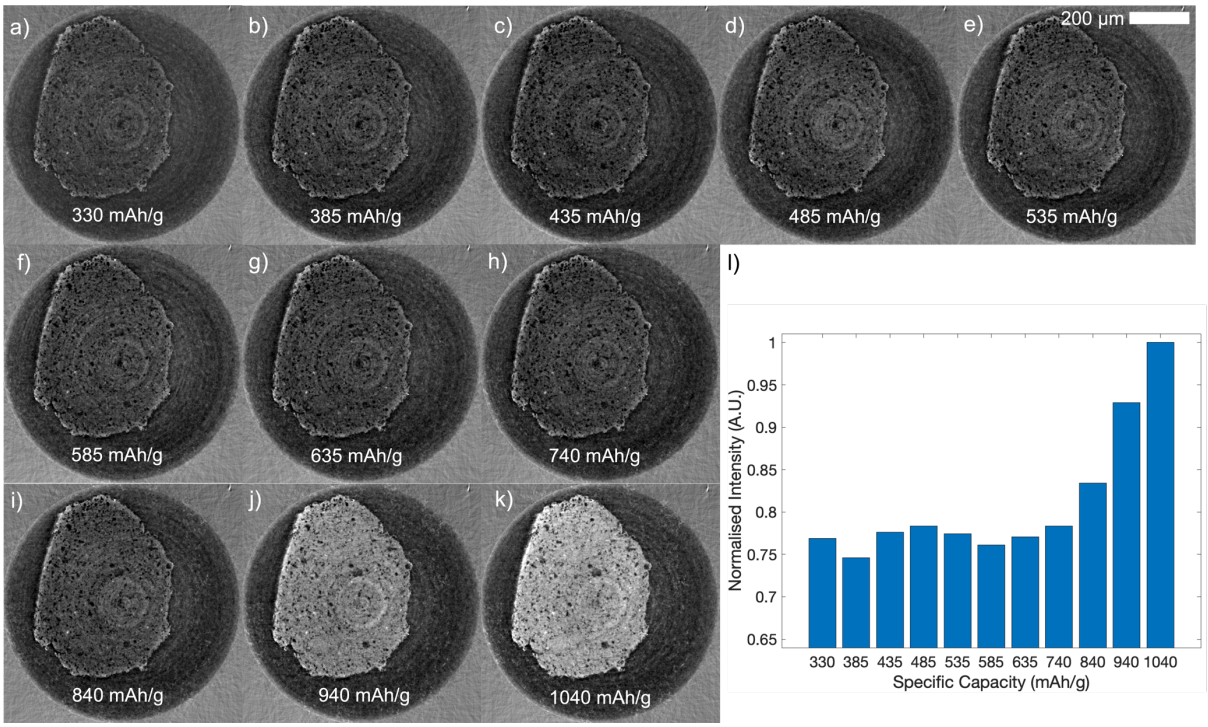

Figure 40 a-k) Tomographic slices of the cathode in the operando cell during discharge (330 to 1040 mAh g^{-1}). l) Average normalised cathode intensity, as a function of depth of discharge.

To observe the presence of precipitated Li_2S in the cathode structure, the slices in Figure 40 have been reconstructed using the Paganin method to obtain phase contrast data.[154] An apparent increase in grayscale intensity is observed after 740 mAh g^{-1} (Figure 40i), linked to the deposition of Li_2S. This deposition is quantified in Figure 40l, which shows that Li_2S is continuously deposited throughout the 2.1 V plateau. However, individual Li_2S particles cannot be resolved and segmented, which suggests that they are smaller than measurement resolution (~1 µm). in the experiment.[62] The deposition of small particles leads to a uniform coverage of the cathode's surfaces, forming a continuous Li_2S layer. Since Li_2S is an electrical insulator, this layer cannot act as a surface for electron transfer with remaining polysulfides dissolved in the electrolyte, effectively blocking the surface and further polysulfide conversion.

The experiment presented in Paper IV was a showed a novel application of both XTM and optical analysis of the electrolyte colour, a multimodal experiment to monitor the multiphase discharge.[137] Future experiments could improve on this methodology by attempting a Raman XTM set up to gain both physical and chemical information simultaneously. Additionally, attention should be paid to the cell design, improving the E/S ratio, and considering engineering a cell that can apply uniform pressure to cell components.[137]

5.3 Lithium Deposition Mechanisms and the Role of the Electrolyte

Li-metal is considered an ideal anode material for high specific energy batteries due to its high theoretical specific capacity (3862 mAh g^{-1}) and low reduction potential (-3.04 V vs. SHE.). However, its implementation in batteries is hindered due to uncontrolled growth of during plating, forming porous, mossy, and dendritic Li-metal structures. The growth of such structures has been mitigate through the use of interlayers,[157] surface modification,[158] and the careful tuning of electrolyte compositions.[85]

Papers II, III, and IV all use $LiNO_3$ as an electrolyte additive to promote the growth of a stable SEI on the Li-metal anode surface. Without $LiNO_3$ cells typical exhibit the polysulfide shuttle mechanisms characterised by extended charge without cell polarisation reaching the cut-off voltage. It is key that a stable SEI is formed on the Li-metal, not only to form a protective layer that supresses the polysulfide shuttle, but to enable stable stripping and plating. However, $LiNO_3$ is known to be a sacrificial additive that is consumed during cell cycling, and once it is consumed the cell will fail.[78] An alternative to $LiNO_3$ is the application of ionic liquid based electrolytes which have been shown to form stable SEIs.[85]

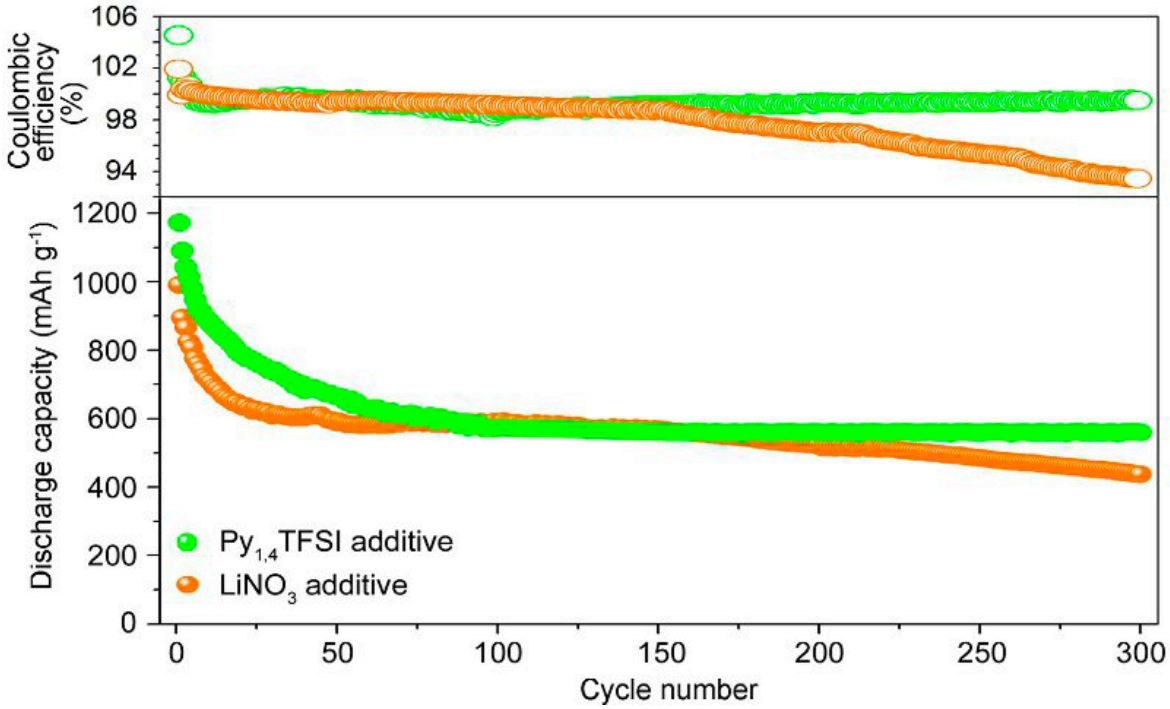

Figure 41 Prolonged cycling and coulombic efficiency comparison over 300 cycles. Cycling rate C/30 = 56 mA g^{-1}; voltage cut-off: 1.4 – 2.8 V for the $Py_{14}TFSI$ cell and 1.8 – 2.8 V for the $LiNO_3$ cell. Figure 5 from Paper V, reproduced with permission from John Wiley and Sons.

Figure 41 shows the cycling performance of a cell when the ionic liquid $Py_{14}TFSI$ is used as an additive to a DOL/DME and LiTFSI electrolyte. The cell maintains a high coulombic efficiency and discharge capacity up to 300 cycles, suggesting that a stable SEI was formed, and reversible stripping/plating of Li-metal occurred. The cell containing $LiNO_3$ sees a significant drop in capacity and coulombic efficiency from cycle 150, suggesting that the SEI on the Li-metal starts to fail, with the consequence of poor Li-metal stripping/ plating. XPS analysis showed the addition of ionic liquid reduces the content of CF_3 in the SEI, while simultaneously increasing C-C content suggesting the SEI formed was polymeric in nature.

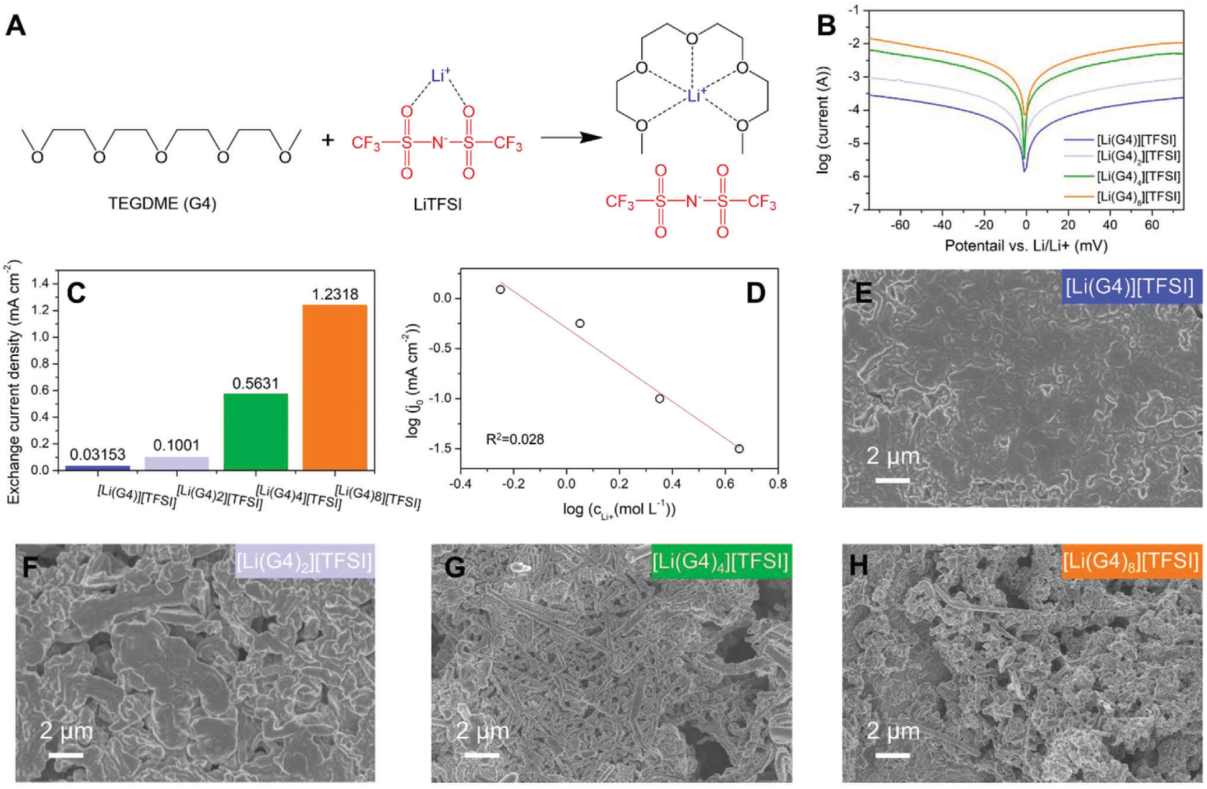

Figure 42 a) Chemical structures of TEGDME (G4), LiTFSI, and the $[Li(G4)]^+[TFSI]^-$ solvate complex. b) Tafel curves for Li electrodes in different electrolytes and c) Corresponding exchange current densities derived from Tafel curves. d) The Relationship between the concentration of Li^+ and the exchange current density. SEM images of Li anodes cycled in the electrolytes e) [Li(G4)][TFSI], f) $[Li(G4)_2][TFSI]$, g) $[Li(G4)_4][TFSI]$, and h) $[Li(G4)_8][TFSI]$. Li anodes were retrieved from Li-Li symmetric cells cycled at 0.5 mA cm^{-2} for 50 cycles. Figure 2 from Paper VI, reproduced under Creative Commons Licence.

To further explore the interaction between electrolyte and Li-metal, a series electrolyte that were a mixture of LiTFSI and TEGDME in various ratios (1:1, 1:2, 1:4, 1:8, Figure 42a) were investigated. The electrolyte with the highest salt content, the 1:1 composition is in fact known as a solvated ionic liquid. It has been shown that at this composition the solvent and the Li^+ form a stable complex acting as an effective cation. It is also this solvate ionic liquid that shows the most stable stripping/plating behaviour. Figure 42e-h shows SEM images of the deposited Li-metal in the various electrolytes. The deposition in the 1:1 ratio electrolyte seems to be the most homogenous, suggesting the key to stable stripping/plating is the formation of a dense Li layer.

To further investigate the Li deposition behaviour for different electrolytes at different salt concentrations, phase field modelling was applied. It showed that electrolytes with a low exchange current density had a more even local current density, and promoted Li nuclei with larger radii, resulting in structures with a low aspect ratio which in turn maintained an even electric field and continued homogenous plating of Li-metal.

The combined use of phase field modelling and SEM in this work presents a valuable insight into the factors controlling the morphology of deposited Li. However, where the phase field modelling provides insights into both the final morphology of Li deposits as well as the evolution of the deposits during further deposition. In contrast the SEM images provided *ex situ* analysis, it images the Li-metal surface thus information on the porosity of the Li-metal and connectivity of structures cannot be revealed. To directly follow Li-metal deposition as it happens and obtain 3D data on similar length scales as those in phase filed modelling, XTM is placed as an ideal complimentary technique, with a comparable resolution and field of view. XTM measurements used in Paper VII were acquired in 50 seconds, with a resolution of ~1 μm, and field of view ϕ = 832 μm. Short measurements times enabled accurate imaging of Li-metal structures during cell operation, with the large field of view capturing a large portion of the electrode area.

Figure 43, displays results of an XTM experiment imaging the growth of Li on Cu in an electrolyte composed of 1 M LiTFSI in DOL/DME with μm resolution. The results show the Li-metal grows to form highly tortuous structures, similar to structures observed in Figure 42h which were characterised by a high exchange current density. After plating Li-metal on Cu at 0.5 mA cm^{-2} for 1 hour, structures are seen to grow to 60 μm in height. After stripping, this

high structure is observed to be relatively unchanged (marked by the green circles, Figure 43d), suggesting it has become electrochemically inactive, forming dead Li. Thus, we see the formation of these highly tortuous need-like structures resulting in poor coulombic efficiency.

The current density of the plating process was further increased to 1.0 mA cm^{-2}, with the increased current density additional plated Li-metal morphologies were observed. Mossy Li forms (yellow dashed box, Figure 43e) in addition to the previously observed tortuous needle-like Li structure. The formation of the mossy Li-metal structure appears to coincide with a kink observed in the voltage profile around 20 minutes into plating (Figure 43b), suggesting the formation of these two structures is associated with different overpotentials.

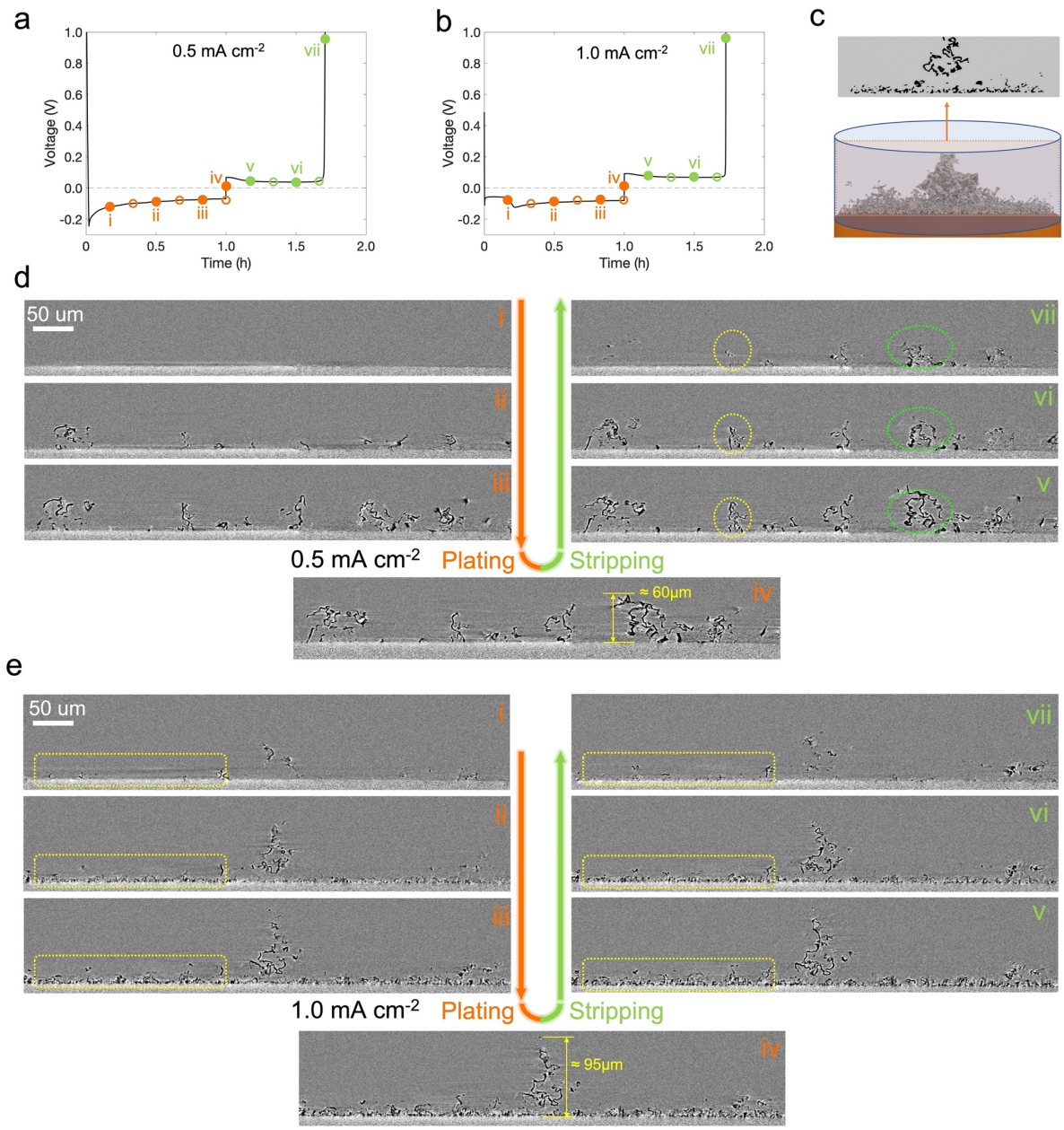

Figure 43 Operando XTM during plating and stripping in the Li-Cu cell at different current densities. Voltage profiles of galvanostatic plating/stripping during operando XTM (a) at 0.5 mA cm^{-2} for the first cycle and (b). at 1.0 mA cm^{-2} in the second cycle. Dots and circles indicate where X-ray tomograms were taken. c) Schematic diagram for the extraction of vertical slices from reconstructed 3D tomographic datasets. d) Reconstructed vertical slices during the first cycle (0.5 mA cm^{-2}). Structures with dark colour are identified as metallic Li and grey background is the liquid electrolyte (1 M LiTFSI in DOL/DME). Representative structures of active and inactive deposited Li are marked by yellow and green dashed circles, respectively. d) Reconstructed vertical slices during the second cycle (1.0 mA cm^{-2}). Region of deposited Li with a small and mossy microstructure is marked by the yellow dashed boxes.

Not only does Figure 43e present mossy and needle-like Li-metal growth, but a Li-metal structure is also observed which reaches 95µm in height. However, the tomograms presented only show the growth of the structure in 2D, a key benefit of XTM is the microstructure evolution can be observed in 3D. Figure 44 presents a 3D rendering of the needle-like dendrite observed in Figure 43e. The growth of the dendrite structure is promoted by the growth of a needle-like structure that combines with the mossy Li-metal structure, creating an integrated foundation that is mechanically stable promoting further growth of the dendrite without structural collapse.

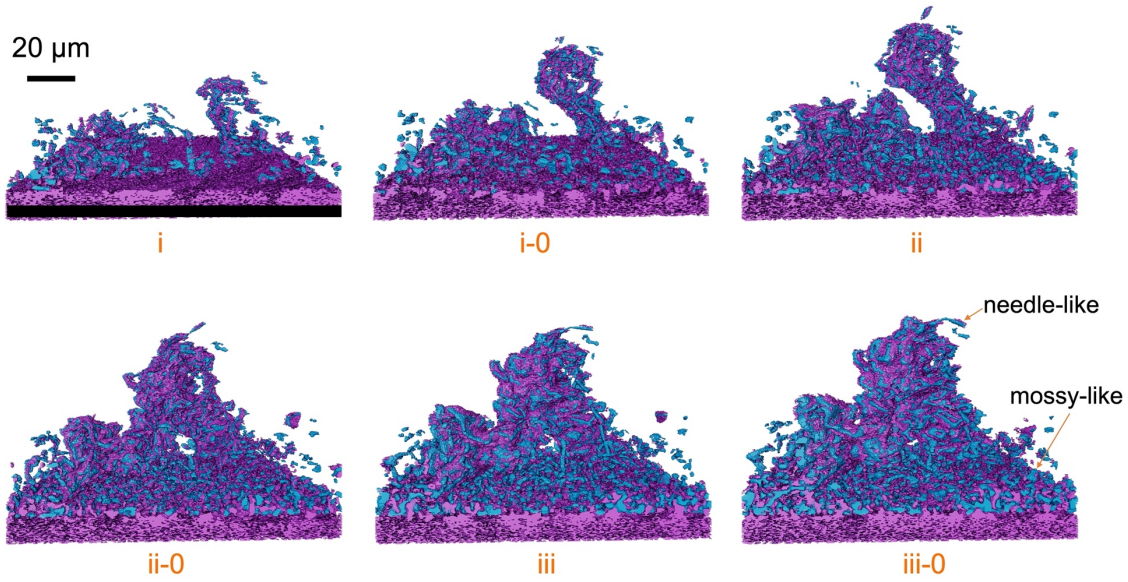

Figure 44 Evolution of Li microstructure formed by the integration of different Li dendrites. The renderings are extracted from tomograms taken during the plating at 1.0 mA cm^{-1} for 10 min (i), 20 min (i-0), 30 min (ii),40 min (ii-0), 50 min (iii), 1 hour (iii-0). The deposited Li is shown in blue and the phases with heavier elements are shown in purple, including the Cu substrate.

The renderings in Figure 44 demonstrate two segmented phases, the first phase assigned as Li-metal (blue) and the second phase observed and assigned as heavier elements (purple). With the second phase consisting of heavier elements and being highly integrated into the Li-metal structure, this phase could be the SEI. If this phase is an SEI, it is observed to be inhomogeneous, with many regions of bare Li-metal observed. Of course, the lack of segmented SEI could be a limitation in resolution. However, this observed inhomogeneity of the SEI would be closely related to growth of tortuous Li-metal structures.

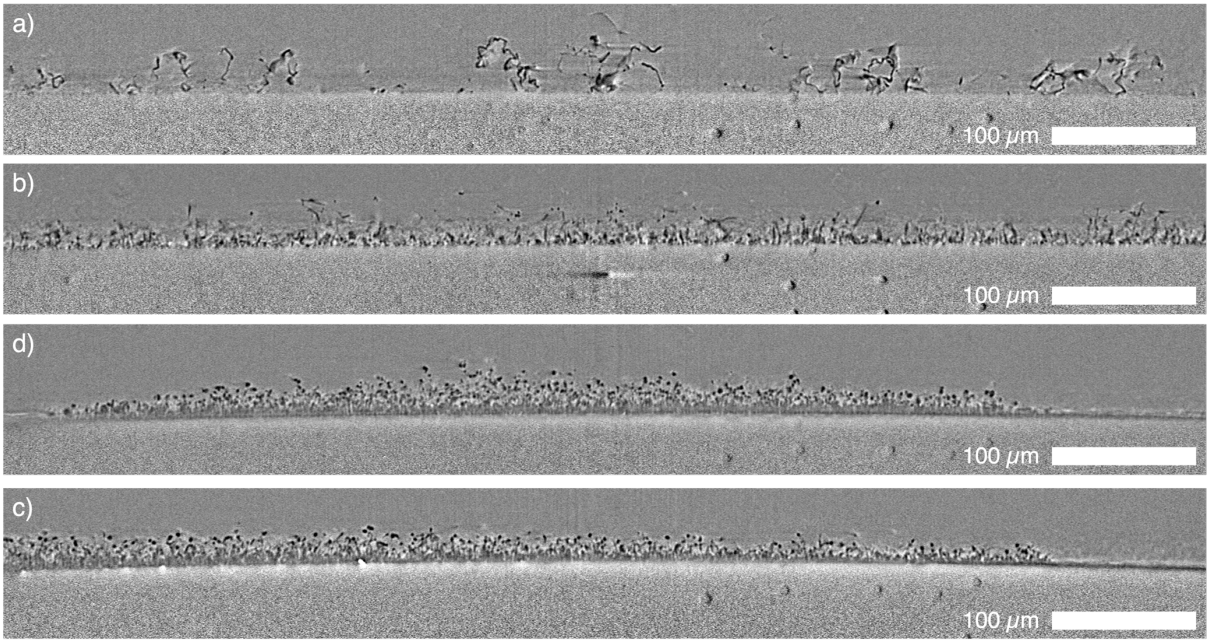

Figure 45 Vertical tomograms taken from Li-Cu cells a) 1 M LiTFSI in 1,2-dimethoxyethane and 1,3-dioxolane (1:1v) after deposition of 0.5 mAh cm^{-2} , b) 1 M LiTFSI, 0.25 M $LiNO_3$ in 1,2-dimethoxyethane and 1,3-dioxolane (1:1v) 1.0 mAh cm^{-2}, c) $Pyr_{1,4}$ FSI, LiFSI (1:0.2 molar ratio) 1.5 mAh cm^{-2}, d) $Pyr_{1,4}$ FSI, LiFSI, HFE (1:0.2:0.5 molar ratio) 1.5 mAh cm^{-2}.

Paper V has shown that cells using electrolytes based on LiTFSI and DOL/DME can be characterised with unstable stripping/plating processes, and poor coulombic efficiency in Li-S full cells. However, this poor coulombic efficiency was addressed through the use of $LiNO_3$ additives and ionic liquids. Figure 45b shows the morphology of plated Li when 0.25 M of $LiNO_3$ was added to the electrolyte. A more homogenous Li phase grows across the entirety of the Cu electrode and does not exceed 40 µm in height. Thus, the dominate morphology is mossy Li, with no needle-like dendrites formed. This mossy Li growth can be associated with stable cycling, and good coulombic efficiencies.

Improving upon morphologies formed with $LiNO_3$ are the morphologies formed when using ionic liquid electrolytes. Figure 41 already showed that ionic liquids can promote stable stripping/plating. Figure 45c shows the Li morphology formed in an ionic liquid electrolyte. The morphologies formed can be characterised as dense, with a homogenous sub-structure formed. Figure 45d shows the same electrolyte diluted with highly fluorinated ether, an electrolyte with lower viscosity. In this electrolyte the Li-metal growth appears to be even more homogenous across the Cu surface, and with a dense substructure formed. Both ionic liquid

electrolytes initially seem to have a mossy Li structure at the surface, however it appears more ordered than the mossy structures seen for the DOL/DME based electrolytes. The morphology of the Li deposited in the ionic liquid can be characterised as globular, thus suggesting a different mechanism of Li nucleation, and implication on the dynamics and reversibility of a cell using this electrolyte.

From the SEM images shown in Figure 42e-h, a dense Li-metal growth can be associated with stable stripping and deposition. XTM data presented in Figure 45c and d are able to go further than the SEM images showing the substructure of the deposited Li-metal, despite the surface structure appearing to be mossy in nature, the substructure formed is dense and homogenous. Despite providing such detailed images, the resolution of the measurement should be considered, only structures on the µm level will be resolved, as such any porosity that is smaller 1 µm will remain undetected. However, when combining the 1 µm resolution with the extended FOV (ϕ = 832 µm), the XTM measurements presented give a unique insight to the Li-metal stripping/plating process. The fast measurements times of the *operando* experiment meant measurements could be made regularly throughout the plating process, enabling correlative analysis with the acquired electrochemical data. With the plating process have a continuous rate, defined by the applied current, a measurement time of 50 seconds was suitable.

6 Conclusions and Outlooks

Many investigations made on Next Generation Battery technologies, including the ones presented in this thesis, target fundamental processes. Looking at processes that are difficult to isolate and observe in a commercial full cells. Investigating fundamental processes is of huge importance, as by increasing our understanding we drive forward new technologies, but such investigations may not provide answers to all practical questions.

To continue such fundamental investigations, pairing experimental methodologies with computational techniques would provide deeper understandings of novel systems, while improving and validating the experimental techniques used. The phase field modelling technique in Paper III provided invaluable insights to the growth process of Li-metal, and could guide the interpretation of the observations from XTM experiments, such as the ones presented in Paper VII. However, the spatial resolution of XTM partly limits the parallels that can be drawn. Thus, methods that can be used for *in situ* measurements and provide sub-micron resolution imaging would act as a perfect pairing to phase field modelling. Not only would increasing the spatial resolution of measurements be beneficial, but so would improving measurement times. Tomography beamlines have started to make kHz measurements, applying such time to battery research could reveal discrete changes, even at higher discharge and charge rates.

However, methodologies in this thesis could be applied in a more practical sense. The use of investigative techniques that are able to provide real-time insights into batteries with realistic configurations and cell designs would be truly exciting. E.g., using high loading electrodes in full cell configurations, reasonable electrolyte volumes, and the application of uniform pressure to cell components. With high resolution imaging of electrode materials over long-term cycling times, one could directly gain key insights to degradation mechanisms over time, from sub μm to mm length scales, and link such information to electrochemical performance. Furthermore, cell designs that provide realistic cycling environments would provide valuable insights.

Both lab and synchrotron techniques are ever pushing forward what is possible in terms of measurement sensitivity, spatial resolutions, and temporal resolutions. By continuing to apply these advancements in measurements to Next Generation Batteries we will continue to provide novel insights to these systems.

7 Acknowledgements

In 2016 I made my first trip to Sweden, to Chalmers University, and to KMF, as the division was known back then. In the five years that have passed since, I have had the pleasure of meeting so many incredible people from a wide range of backgrounds, all of whom have added to the enjoyment of my time here.

First and foremost, I want to thank my supervisor Aleksandar Matic, who first agreed to host me for my master's thesis back in 2016. Who knew back then you would be stuck with me for so long. You have been a brilliant supervisor who has provided me with many opportunities, connected me with fantastic researchers, filling my time as a doctoral student to the brim with knowledge. I can only hope some of it stuck.

To the many members of the division formally known as Kondenserande Materiens Fysik here at Chalmers (now Materialfysik) who I have known over the years, you have all played a part in this journey, and I thank you for the help and guidance I have received over these years. Now, if I don't mention Filippa Lundin I will be in trouble. Filippa was a project assistant at the same time I arrived for my master's thesis, and then started her doctoral studies around the same time as me, and we have both been on this path together. I have truly valued your friendship over these years, and I wish you all the best with these last months of your studies. I must also thank Shizhao, who has been my partner in crime as we have planned and performed synchrotron experiments. Including making arduous trips by train to Switzerland and the south of France, all in the purpose of delivering our 'precious' samples in one piece. We were not always successful.

To my friends both here in Sweden, and back home in the UK, I thank you for being there during both the ups and the downs. Whether it be with a simple phone call or finding the time to make the journey here to visit this wonderful city. Most importantly, to my family, thank you for encouraging me through all my decisions and for your unwavering support during my time here in Sweden.

Finally, I would like to thank the Swedish Energy Agency for funding and supporting the work I have carried out over the course of my doctoral studies.

8 References

[1] Volkswagen AG, Hydrogen or battery? A clear case, until further notice, (2019). https://www.volkswagenag.com/en/news/stories/2019/08/hydrogen-or-battery--that-is-the-question.html# (accessed August 5, 2021).

[2] A. Yoshino, The birth of the lithium-ion battery, Angew. Chemie - Int. Ed. 51 (2012) 5798–5800. https://doi.org/10.1002/anie.201105006.

[3] B. Scrosati, J. Garche, Lithium batteries: Status, prospects and future, J. Power Sources. 195 (2010) 2419–2430. https://doi.org/10.1016/j.jpowsour.2009.11.048.

[4] M.S. Ziegler, J.E. Trancik, Re-examining rates of lithium-ion battery technology improvement and cost decline, Energy Environ. Sci. 14 (2021) 1635–1651. https://doi.org/10.1039/d0ee02681f.

[5] F. Wu, J. Maier, Y. Yu, Guidelines and trends for next-generation rechargeable lithium and lithium-ion batteries, Chem. Soc. Rev. 49 (2020) 1569–1614. https://doi.org/10.1039/c7cs00863e.

[6] A. Celeste, L. Silvestri, M. Agostini, M. Sadd, S. Palumbo, J.K. Panda, A. Matic, V. Pellegrini, S. Brutti, Enhancement of Functional Properties of Liquid Electrolytes for Lithium-Ion Batteries by Addition of Pyrrolidinium-Based Ionic Liquids with Long Alkyl-Chains, Batter. Supercaps. 3 (2020) 1059–1068. https://doi.org/10.1002/batt.202000070.

[7] R.F. Ziesche, T. Arlt, D.P. Finegan, T.M.M. Heenan, A. Tengattini, D. Baum, N. Kardjilov, H. Markötter, I. Manke, W. Kockelmann, D.J.L. Brett, P.R. Shearing, 4D imaging of lithium-batteries using correlative neutron and X-ray tomography with a virtual unrolling technique, Nat. Commun. 11 (2020) 1–11. https://doi.org/10.1038/s41467-019-13943-3.

[8] A. Volta, On the Electricity excited by the mere Contact of conducting Substances of different kinds, Philos. Trans. R. Soc. (1800). https://doi.org/10.1098/rstl.1800.0018.

[9] A.J. Bard, L.R. Faulkner, Electrochemical Methods, John Wiley & Sons, Inc., 2001.

[10] Y. Liu, X. Xu, M. Sadd, O.O. Kapitanova, V.A. Krivchenko, J. Ban, J. Wang, X. Jiao, Z. Song, J. Song, S. Xiong, A. Matic, Insight into the Critical Role of Exchange Current Density on Electrodeposition Behavior of Lithium Metal, Adv. Sci. 2003301 (2021) 1–11. https://doi.org/10.1002/advs.202003301.

[11] Batteries Europe ETIP, Batteries Europe: Strategic Research Agenda for 2020, Eur. Technol. Inov. Platf. ENER-2018- (2015) 9–75.

[12] O. Ramström, The Nobel Prize in Chemistry 2019 - Scientific background, R. Swedish Acad. Sci. 50005 (2019) 0–13. https://www.nobelprize.org/prizes/chemistry/2019/advanced-information/.

[13] A. Manthiram, A reflection on lithium-ion battery cathode chemistry, Nat. Commun. 11 (2020) 1–9. https://doi.org/10.1038/s41467-020-15355-0.

[14] D. Guyornard, J.M. Tarascon, Rocking-Chair or Li thium-Ion Rechargeable Lithium Batteries, Adv. Mater. 6 (1994) 408.

[15] B. Scrosati, Lithium Rocking Chair Batteries: An Old Concept?, J. Electrochem. Soc. 139 (1992) 2776–2781. https://doi.org/10.1149/1.2068978.

[16] M.S. Whittingham, Electrical Energy Storage and Intercalation Chemistry, Science (80-.). 192 (1976) 1126 LP – 1127. https://doi.org/10.1126/science.192.4244.1126.

[17] R. Yazami, P. Touzain, A reversible graphite-lithium negative electrode for electrochemical generators, J. Power Sources. 9 (1983) 365–371. https://doi.org/10.1016/0378-7753(83)87040-2.

[18] Z. Shahan, LG Chem Has Begun Mass Production Of NCM712 Batteries In Poland,

Clean Tech. (2021). https://cleantechnica.com/2020/06/11/lg-chem-began-mass-production-of-ncm712-batteries-in-poland-in-q1/ (accessed November 19, 2021).
[19] The Faraday Institution, High-energy battery technologies, Faraday Rep. (2020) 1–38.
[20] J.B. Goodenough, Y. Kim, Challenges for rechargeable Li batteries, Chem. Mater. 22 (2010) 587–603. https://doi.org/10.1021/cm901452z.
[21] E. Peled, The Electrochemical Behavior of Alkali and Alkaline Earth Metals in Nonaqueous Battery Systems—The Solid Electrolyte Interphase Model, J. Electrochem. Soc. 126 (1979) 2047–2051. https://doi.org/10.1149/1.2128859.
[22] E. Peled, D. Golodnitsky, G. Ardel, Advanced Model for Solid Electrolyte Interphase Electrodes in Liquid and Polymer Electrolytes, J. Electrochem. Soc. 144 (1997) L208–L210. https://doi.org/10.1149/1.1837858.
[23] E. Peled, S. Menkin, Review—SEI: Past, Present and Future, J. Electrochem. Soc. 164 (2017) A1703–A1719. https://doi.org/10.1149/2.1441707jes.
[24] K. Kanamura, H. Tamura, S. Shiraishi, Z. ichiro Takehara, Morphology and chemical compositions of surface films of lithium deposited on a Ni substrate in nonaqueous electrolytes, J. Electroanal. Chem. 394 (1995) 49–62. https://doi.org/10.1016/0022-0728(95)03972-J.
[25] D. Aurbach, Y. Ein-Ely, A. Zaban, The Surface Chemistry of Lithium Electrodes in Alkyl Carbonate Solutions, J. Electrochem. Soc. 141 (1994) L1–L3. https://doi.org/10.1149/1.2054718.
[26] D. Aurbach, M.L. Daroux, P.W. Faguy, E. Yeager, Identification of Surface Films Formed on Lithium in Propylene Carbonate Solutions, J. Electrochem. Soc. 134 (1987) 1611–1620. https://doi.org/10.1149/1.2100722.
[27] E. Irisarri, A. Ponrouch, M.R. Palacin, Review—Hard Carbon Negative Electrode Materials for Sodium-Ion Batteries, J. Electrochem. Soc. 162 (2015) A2476–A2482. https://doi.org/10.1149/2.0091514jes.
[28] W. Luo, J. Wan, B. Ozdemir, W. Bao, Y. Chen, J. Dai, H. Lin, Y. Xu, F. Gu, V. Barone, L. Hu, Potassium Ion Batteries with Graphitic Materials, Nano Lett. 15 (2015) 7671–7677. https://doi.org/10.1021/acs.nanolett.5b03667.
[29] X. Xu, D. Zhou, X. Qin, K. Lin, F. Kang, B. Li, D. Shanmukaraj, T. Rojo, M. Armand, G. Wang, A room-temperature sodium–sulfur battery with high capacity and stable cycling performance, Nat. Commun. 9 (2018) 1–12. https://doi.org/10.1038/s41467-018-06443-3.
[30] A. Bauer, J. Song, S. Vail, W. Pan, J. Barker, Y. Lu, The Scale-up and Commercialization of Nonaqueous Na-Ion Battery Technologies, Adv. Energy Mater. 8 (2018) 1–13. https://doi.org/10.1002/aenm.201702869.
[31] M.D. Slater, D. Kim, E. Lee, C.S. Johnson, Sodium-ion batteries, Adv. Funct. Mater. 23 (2013) 947–958. https://doi.org/10.1002/adfm.201200691.
[32] P.G. Bruce, S.A. Freunberger, L.J. Hardwick, J.M. Tarascon, LigO2 and LigS batteries with high energy storage, Nat. Mater. 11 (2012) 19–29. https://doi.org/10.1038/nmat3191.
[33] X. Ji, L.F. Nazar, Advances in Li-S batteries, J. Mater. Chem. 20 (2010) 9821–9826. https://doi.org/10.1039/b925751a.
[34] A. Manthiram, Y. Fu, Y.S. Su, Challenges and prospects of lithium-sulfur batteries, Acc. Chem. Res. 46 (2013) 1125–1134. https://doi.org/10.1021/ar300179v.
[35] Z. Wen, Y. Hu, X. Wu, J. Han, Z. Gu, Main challenges for high performance NAS battery: Materials and interfaces, Adv. Funct. Mater. 23 (2013) 1005–1018. https://doi.org/10.1002/adfm.201200473.
[36] I. Shterenberg, M. Salama, Y. Gofer, E. Levi, D. Aurbach, The challenge of developing rechargeable magnesium batteries, MRS Bull. 39 (2014) 453–460.

https://doi.org/10.1557/mrs.2014.61.
[37] D. Larcher, J.M. Tarascon, Towards greener and more sustainable batteries for electrical energy storage, Nat. Chem. 7 (2015) 19–29. https://doi.org/10.1038/nchem.2085.
[38] Q. Li, N.J. Bjerrum, Aluminum as anode for energy storage and conversion: A review, J. Power Sources. 110 (2002) 1–10. https://doi.org/10.1016/S0378-7753(01)01014-X.
[39] CATL, CATL Unveils Its Latest Breakthrough Technology by Releasing Its First Generation of Sodium-ion Batteries, (2021). https://www.catl.com/en/news/665.html (accessed November 19, 2021).
[40] N. Tapia-Ruiz, A.R. Armstrong, H. Alptekin, M.A. Amores, H. Au, J. Barker, R. Boston, W.R. Brant, J.M. Brittain, Y. Chen, M. Chhowalla, Y.S. Choi, S.I.R. Costa, M.C. Ribadeneyra, S.A. Cussen, E.J. Cussen, W.I.F. David, A. V. Desai, S.A.M. Dickson, E.I. Eweka, J.D. Forero-Saboya, C.P. Grey, J.M. Griffin, P. Gross, X. Hua, J.T.S. Irvine, P. Johansson, M.O. Jones, M. Karlsmo, E. Kendrick, E. Kim, O. V. Kolosov, Z. Li, S.F.L. Mertens, R. Mogensen, L. Monconduit, R.E. Morris, A.J. Naylor, S. Nikman, C.A. O'Keefe, D.M.C. Ould, R.G. Palgrave, P. Poizot, A. Ponrouch, S. Renault, E.M. Reynolds, A. Rudola, R. Sayers, D.O. Scanlon, S. Sen, V.R. Seymour, B. Silván, M.T. Sougrati, L. Stievano, G.S. Stone, C.I. Thomas, M.M. Titirici, J. Tong, T.J. Wood, D.S. Wright, R. Younesi, 2021 roadmap for sodium-ion batteries, JPhys Energy. 3 (2021). https://doi.org/10.1088/2515-7655/ac01ef.
[41] Y. Fang, D. Luan, X.W. Lou, Recent Advances on Mixed Metal Sulfides for Advanced Sodium-Ion Batteries, Adv. Mater. 32 (2020). https://doi.org/10.1002/adma.202002976.
[42] M.S. Islam, C.A.J. Fisher, Lithium and sodium battery cathode materials: Computational insights into voltage, diffusion and nanostructural properties, Chem. Soc. Rev. 43 (2014) 185–204. https://doi.org/10.1039/c3cs60199d.
[43] G. Wang, F. Wang, P. Zhang, J. Zhang, T. Zhang, K. Müllen, X. Feng, Polarity-Switchable Symmetric Graphite Batteries with High Energy and High Power Densities, Adv. Mater. 30 (2018). https://doi.org/10.1002/adma.201802949.
[44] J. Zhao, X. Zou, Y. Zhu, Y. Xu, C. Wang, Electrochemical Intercalation of Potassium into Graphite, Adv. Funct. Mater. 26 (2016) 8103–8110. https://doi.org/10.1002/adfm.201602248.
[45] B. Jache, P. Adelhelm, Use of Graphite as a Highly Reversible Electrode with Superior Cycle Life for Sodium-Ion Batteries by Making Use of Co-Intercalation Phenomena, Angew. Chemie. 126 (2014) 10333–10337. https://doi.org/10.1002/ange.201403734.
[46] Y. Wen, K. He, Y. Zhu, F. Han, Y. Xu, I. Matsuda, Y. Ishii, J. Cumings, C. Wang, Expanded graphite as superior anode for sodium-ion batteries, Nat. Commun. 5 (2014) 1–10. https://doi.org/10.1038/ncomms5033.
[47] H. Kim, J. Hong, Y.U. Park, J. Kim, I. Hwang, K. Kang, Sodium storage behavior in natural graphite using ether-based electrolyte systems, Adv. Funct. Mater. 25 (2015) 534–541. https://doi.org/10.1002/adfm.201402984.
[48] Y. Liu, B. V. Merinov, W.A. Goddard, Origin of low sodium capacity in graphite and generally weak substrate binding of Na and Mg among alkali and alkaline earth metals, Proc. Natl. Acad. Sci. U. S. A. 113 (2016) 3735–3739. https://doi.org/10.1073/pnas.1602473113.
[49] B. Xiao, T. Rojo, X. Li, Hard Carbon as Sodium-Ion Battery Anodes: Progress and Challenges, ChemSusChem. 12 (2019) 133–144. https://doi.org/10.1002/cssc.201801879.
[50] J. Sun, A. Iakunkov, A.T. Rebrikova, A. V. Talyzin, Exactly matched pore size for the intercalation of electrolyte ions determined using the tunable swelling of graphite oxide

in supercapacitor electrodes, Nanoscale. 10 (2018) 21386–21395. https://doi.org/10.1039/c8nr07469k.
[51] L. Zhang, J. Yu, M. Yang, Q. Xie, H. Peng, Z. Liu, Janus graphene from asymmetric two-dimensional chemistry, Nat. Commun. 4 (2013) 1–7. https://doi.org/10.1038/ncomms2464.
[52] M. Agostini, J.Y. Hwang, H.M. Kim, P. Bruni, S. Brutti, F. Croce, A. Matic, Y.K. Sun, Minimizing the Electrolyte Volume in Li–S Batteries: A Step Forward to High Gravimetric Energy Density, Adv. Energy Mater. 8 (2018) 1–7. https://doi.org/10.1002/aenm.201801560.
[53] M. Agostini, D.H. Lim, M. Sadd, J.Y. Hwang, S. Brutti, J.W. Heo, J.H. Ahn, Y.K. Sun, A. Matic, Rational Design of Low Cost and High Energy Lithium Batteries through Tailored Fluorine-free Electrolyte and Nanostructured S/C Composite, ChemSusChem. 11 (2018) 2981–2986. https://doi.org/10.1002/cssc.201801017.
[54] M. Agostini, M. Sadd, S. Xiong, C. Cavallo, J. Heo, J.H. Ahn, A. Matic, Designing a safe electrolyte enabling long-life Li/S batteries, ChemSusChem. 12 (2019) 1–10. https://doi.org/10.1002/cssc.201901770.
[55] Thomas Jefferson National Accelerator Facility, The Element Sulfur, (2020). http://education.jlab.org/itselemental/ele016.html (accessed July 8, 2020).
[56] U.S. Geological Survey, Sulfur, 2020.
[57] S.S. Zhang, Liquid electrolyte lithium/sulfur battery: Fundamental chemistry, problems, and solutions, J. Power Sources. 231 (2013) 153–162. https://doi.org/10.1016/j.jpowsour.2012.12.102.
[58] M. Wild, L. O'Neill, T. Zhang, R. Purkayastha, G. Minton, M. Marinescu, G.J. Offer, Lithium sulfur batteries, a mechanistic review, Energy Environ. Sci. 8 (2015) 3477–3494. https://doi.org/10.1039/c5ee01388g.
[59] T. Danner, A. Latz, On the influence of nucleation and growth of S8 and Li2S in lithium-sulfur batteries, Electrochim. Acta. 322 (2019). https://doi.org/10.1016/j.electacta.2019.134719.
[60] A. Vizintin, L. Chabanne, E. Tchernychova, I. Arčon, L. Stievano, G. Aquilanti, M. Antonietti, T.P. Fellinger, R. Dominko, The mechanism of Li2S activation in lithium-sulfur batteries: Can we avoid the polysulfide formation?, J. Power Sources. 344 (2017) 208–217. https://doi.org/10.1016/j.jpowsour.2017.01.112.
[61] F.Y. Fan, W.C. Carter, Y.M. Chiang, Mechanism and Kinetics of Li2S Precipitation in Lithium-Sulfur Batteries, Adv. Mater. 27 (2015) 5203–5209. https://doi.org/10.1002/adma.201501559.
[62] S. Drvarič Talian, G. Kapun, J. Moškon, A. Vizintin, A. Randon-Vitanova, R. Dominko, M. Gaberšček, Which Process Limits the Operation of a Li-S System?, Chem. Mater. (2019). https://doi.org/10.1021/acs.chemmater.9b03255.
[63] S. Xiong, K. Xie, Y. Diao, X. Hong, Characterization of the solid electrolyte interphase on lithium anode for preventing the shuttle mechanism in lithium-sulfur batteries, J. Power Sources. 246 (2014) 840–845. https://doi.org/10.1016/j.jpowsour.2013.08.041.
[64] R. Kumar, J. Liu, J.Y. Hwang, Y.K. Sun, Recent research trends in Li-S batteries, J. Mater. Chem. A. 6 (2018) 11582–11605. https://doi.org/10.1039/c8ta01483c.
[65] J. He, L. Luo, Y. Chen, A. Manthiram, Yolk–Shelled C@Fe3O4 Nanoboxes as Efficient Sulfur Hosts for High-Performance Lithium–Sulfur Batteries, Adv. Mater. 29 (2017) 1–5. https://doi.org/10.1002/adma.201702707.
[66] B. Zhang, X. Qin, G.R. Li, X.P. Gao, Enhancement of long stability of sulfur cathode by encapsulating sulfur into micropores of carbon spheres, Energy Environ. Sci. 3 (2010) 1531–1537. https://doi.org/10.1039/c002639e.
[67] H. Wang, Y. Yang, Y. Liang, J.T. Robinson, Y. Li, A. Jackson, Y. Cui, H. Dai,

Graphene-wrapped sulfur particles as a rechargeable lithium-sulfur battery cathode material with high capacity and cycling stability, Nano Lett. 11 (2011) 2644–2647. https://doi.org/10.1021/nl200658a.
[68] Z.W. Seh, W. Li, J.J. Cha, G. Zheng, Y. Yang, M.T. McDowell, P.C. Hsu, Y. Cui, Sulphur-TiO 2 yolk-shell nanoarchitecture with internal void space for long-cycle lithium-sulphur batteries, Nat. Commun. 4 (2013). https://doi.org/10.1038/ncomms2327.
[69] X. Yu, J. Joseph, A. Manthiram, Polymer lithium-sulfur batteries with a Nafion membrane and an advanced sulfur electrode, J. Mater. Chem. A. 3 (2015) 15683–15691. https://doi.org/10.1039/c5ta04289e.
[70] Y.S. Su, A. Manthiram, Lithium-sulphur batteries with a microporous carbon paper as a bifunctional interlayer, Nat. Commun. 3 (2012) 1–6. https://doi.org/10.1038/ncomms2163.
[71] Q. Pang, A. Shyamsunder, B. Narayanan, C.Y. Kwok, L.A. Curtiss, L.F. Nazar, Tuning the electrolyte network structure to invoke quasi-solid state sulfur conversion and suppress lithium dendrite formation in Li–S batteries, Nat. Energy. 3 (2018) 783–791. https://doi.org/10.1038/s41560-018-0214-0.
[72] Y. Aihara, S. Ito, R. Omoda, T. Yamada, S. Fujiki, T. Watanabe, Y. Park, S. Doo, The electrochemical characteristics and applicability of an amorphous sulfide-based solid ion conductor for the next-generation solid-state lithium secondary batteries, Front. Energy Res. 4 (2016) 1–8. https://doi.org/10.3389/fenrg.2016.00018.
[73] T. Yamada, S. Ito, R. Omoda, T. Watanabe, Y. Aihara, M. Agostini, U. Ulissi, J. Hassoun, B. Scrosati, All Solid-State Lithium–Sulfur Battery Using a Glass-Type P 2 S 5 –Li 2 S Electrolyte: Benefits on Anode Kinetics , J. Electrochem. Soc. 162 (2015) A646–A651. https://doi.org/10.1149/2.0441504jes.
[74] J.C. Bachman, S. Muy, A. Grimaud, H.H. Chang, N. Pour, S.F. Lux, O. Paschos, F. Maglia, S. Lupart, P. Lamp, L. Giordano, Y. Shao-Horn, Inorganic Solid-State Electrolytes for Lithium Batteries: Mechanisms and Properties Governing Ion Conduction, Chem. Rev. 116 (2016) 140–162. https://doi.org/10.1021/acs.chemrev.5b00563.
[75] A. Manthiram, X. Yu, S. Wang, Lithium battery chemistries enabled by solid-state electrolytes, Nat. Rev. Mater. 2 (2017) 1–16. https://doi.org/10.1038/natrevmats.2016.103.
[76] M.J. Lacey, A. Yalamanchili, J. Maibach, C. Tengstedt, K. Edström, D. Brandell, The Li-S battery: An investigation of redox shuttle and self-discharge behaviour with LiNO3-containing electrolytes, RSC Adv. 6 (2016) 3632–3641. https://doi.org/10.1039/c5ra23635e.
[77] S.S. Zhang, A new finding on the role of LiNO3 in lithium-sulfur battery, J. Power Sources. 322 (2016) 99–105. https://doi.org/10.1016/j.jpowsour.2016.05.009.
[78] A. Jozwiuk, B.B. Berkes, T. Weiß, H. Sommer, J. Janek, T. Brezesinski, The critical role of lithium nitrate in the gas evolution of lithium-sulfur batteries, Energy Environ. Sci. 9 (2016) 2603–2608. https://doi.org/10.1039/c6ee00789a.
[79] D. Bresser, S. Passerini, B. Scrosati, Recent progress and remaining challenges in sulfur-based lithium secondary batteries - a review, Chem. Commun. 49 (2013) 10545–10562. https://doi.org/10.1039/c3cc46131a.
[80] Danuta Herbert and Juliusz Ulam, US Patent 3043896, 3043896, 1962.
[81] X. Ji, K.T. Lee, L.F. Nazar, A highly ordered nanostructured carbon-sulphur cathode for lithium-sulphur batteries, Nat. Mater. 8 (2009) 500–506. https://doi.org/10.1038/nmat2460.
[82] C. Cavallo, M. Agostini, J.P. Genders, M.E. Abdelhamid, A. Matic, A free-standing

reduced graphene oxide aerogel as supporting electrode in a fluorine-free Li2S8 catholyte Li-S battery, J. Power Sources. 416 (2019) 111–117. https://doi.org/10.1016/j.jpowsour.2019.01.081.
[83] J. Scheers, S. Fantini, P. Johansson, A review of electrolytes for lithium-sulphur batteries, J. Power Sources. 255 (2014) 204–218. https://doi.org/10.1016/j.jpowsour.2014.01.023.
[84] M. Agostini, S. Xiong, A. Matic, J. Hassoun, Polysulfide-containing Glyme-based Electrolytes for Lithium Sulfur Battery, Chem. Mater. 27 (2015) 4604–4611. https://doi.org/10.1021/acs.chemmater.5b00896.
[85] S. Xiong, K. Xie, E. Blomberg, P. Jacobsson, A. Matic, Analysis of the solid electrolyte interphase formed with an ionic liquid electrolyte for lithium-sulfur batteries, J. Power Sources. 252 (2014) 150–155. https://doi.org/10.1016/j.jpowsour.2013.11.119.
[86] X. Yu, A. Manthiram, Electrode-Electrolyte Interfaces in Lithium-Sulfur Batteries with Liquid or Inorganic Solid Electrolytes, Acc. Chem. Res. 50 (2017) 2653–2660. https://doi.org/10.1021/acs.accounts.7b00460.
[87] J. Park, K. Ueno, N. Tachikawa, K. Dokko, M. Watanabe, Ionic Liquid Electrolytes for Lithium − Sulfur Batteries, (2013).
[88] Y.G. Lee, S. Fujiki, C. Jung, N. Suzuki, N. Yashiro, R. Omoda, D.S. Ko, T. Shiratsuchi, T. Sugimoto, S. Ryu, J.H. Ku, T. Watanabe, Y. Park, Y. Aihara, D. Im, I.T. Han, High-energy long-cycling all-solid-state lithium metal batteries enabled by silver–carbon composite anodes, Nat. Energy. 5 (2020) 299–308. https://doi.org/10.1038/s41560-020-0575-z.
[89] Q. Zou, Y.C. Lu, Solvent-Dictated Lithium Sulfur Redox Reactions: An Operando UV-vis Spectroscopic Study, J. Phys. Chem. Lett. 7 (2016) 1518–1525. https://doi.org/10.1021/acs.jpclett.6b00228.
[90] H. Shin, M. Baek, A. Gupta, K. Char, A. Manthiram, J.W. Choi, Recent Progress in High Donor Electrolytes for Lithium–Sulfur Batteries, Adv. Energy Mater. 10 (2020) 1–21. https://doi.org/10.1002/aenm.202001456.
[91] K. Dokko, N. Tachikawa, K. Yamauchi, M. Tsuchiya, A. Yamazaki, E. Takashima, J.-W. Park, K. Ueno, S. Seki, N. Serizawa, M. Watanabe, Solvate Ionic Liquid Electrolyte for Li–S Batteries, J. Electrochem. Soc. 160 (2013) A1304–A1310. https://doi.org/10.1149/2.111308jes.
[92] D.H. Lim, M. Agostini, F. Nitze, J. Manuel, J.H. Ahn, A. Matic, Route to sustainable lithium-sulfur batteries with high practical capacity through a fluorine free polysulfide catholyte and self-standing Carbon Nanofiber membranes, Sci. Rep. 7 (2017) 1–9. https://doi.org/10.1038/s41598-017-06593-2.
[93] M. Agostini, D.J. Lee, B. Scrosati, Y.K. Sun, J. Hassoun, Characteristics of Li2S8-tetraglyme catholyte in a semi-liquid lithium-sulfur battery, J. Power Sources. 265 (2014) 14–19. https://doi.org/10.1016/j.jpowsour.2014.04.074.
[94] J. He, G. Hartmann, M. Lee, G.S. Hwang, Y. Chen, A. Manthiram, Freestanding 1T MoS 2 /graphene heterostructures as a highly efficient electrocatalyst for lithium polysulfides in Li-S batteries, Energy Environ. Sci. 12 (2019) 344–350. https://doi.org/10.1039/c8ee03252a.
[95] Q. Pang, D. Kundu, L.F. Nazar, A graphene-like metallic cathode host for long-life and high-loading lithium-sulfur batteries, Mater. Horizons. 3 (2016) 130–136. https://doi.org/10.1039/c5mh00246j.
[96] S.H. Chung, L. Luo, A. Manthiram, TiS2-Polysulfide Hybrid Cathode with High Sulfur Loading and Low Electrolyte Consumption for Lithium-Sulfur Batteries, ACS Energy Lett. 3 (2018) 568–573. https://doi.org/10.1021/acsenergylett.7b01321.

[97] S.H. Chung, A. Manthiram, Rational Design of Statically and Dynamically Stable Lithium–Sulfur Batteries with High Sulfur Loading and Low Electrolyte/Sulfur Ratio, Adv. Mater. 30 (2018) 1–9. https://doi.org/10.1002/adma.201705951.
[98] D. Lin, Y. Liu, Y. Cui, Reviving the lithium metal anode for high-energy batteries, Nat. Nanotechnol. 12 (2017) 194–206. https://doi.org/10.1038/nnano.2017.16.
[99] P. Biswal, S. Stalin, A. Kludze, S. Choudhury, L.A. Archer, Nucleation and Early Stage Growth of Li Electrodeposits, Nano Lett. 19 (2019) 8191–8200. https://doi.org/10.1021/acs.nanolett.9b03548.
[100] M.S. Whittingham, Lithium batteries and cathode materials, Chem. Rev. 104 (2004) 4271–4301. https://doi.org/10.1021/cr020731c.
[101] K. BRANDT, Historical development of secondary lithium batteries, Solid State Ionics. 69 (1994) 173–183. https://doi.org/10.1016/0167-2738(94)90408-1.
[102] P. Personnettaz, S. Landgraf, M. Nimtz, N. Weber, T. Weier, Mass transport induced asymmetry in charge/discharge behavior of liquid metal batteries, Electrochem. Commun. 105 (2019) 106496. https://doi.org/10.1016/j.elecom.2019.106496.
[103] C. Monroe, J. Newman, Dendrite Growth in Lithium/Polymer Systems, J. Electrochem. Soc. 150 (2003) A1377. https://doi.org/10.1149/1.1606686.
[104] C. Monroe, J. Newman, The Impact of Elastic Deformation on Deposition Kinetics at Lithium/Polymer Interfaces, J. Electrochem. Soc. 152 (2005) A396. https://doi.org/10.1149/1.1850854.
[105] D. Aurbach, E. Pollak, R. Elazari, G. Salitra, C.S. Kelley, J. Affinito, On the Surface Chemical Aspects of Very High Energy Density, Rechargeable Li–Sulfur Batteries, J. Electrochem. Soc. 156 (2009) A694. https://doi.org/10.1149/1.3148721.
[106] S. Xiong, K. Xie, Y. Diao, X. Hong, Properties of surface film on lithium anode with LiNO 3 as lithium salt in electrolyte solution for lithium-sulfur batteries, Electrochim. Acta. 83 (2012) 78–86. https://doi.org/10.1016/j.electacta.2012.07.118.
[107] H. Jin, H. Liu, H. Cheng, P. Zhang, M. Wang, The synergistic effect of lithium bis(fluorosulfonyl)imide and lithium nitrate for high-performance lithium metal anode, J. Electroanal. Chem. 874 (2020) 114484. https://doi.org/10.1016/j.jelechem.2020.114484.
[108] C. Fang, J. Li, M. Zhang, Y. Zhang, F. Yang, J.Z. Lee, M.H. Lee, J. Alvarado, M.A. Schroeder, Y. Yang, B. Lu, N. Williams, M. Ceja, L. Yang, M. Cai, J. Gu, K. Xu, X. Wang, Y.S. Meng, Quantifying inactive lithium in lithium metal batteries, Nature. 572 (2019) 511–515. https://doi.org/10.1038/s41586-019-1481-z.
[109] A.J. Sanchez, E. Kazyak, Y. Chen, K.H. Chen, E.R. Pattison, N.P. Dasgupta, Plan-View Operando Video Microscopy of Li Metal Anodes: Identifying the Coupled Relationships among Nucleation, Morphology, and Reversibility, ACS Energy Lett. 5 (2020) 994–1004. https://doi.org/10.1021/acsenergylett.0c00215.
[110] K.H. Chen, K.N. Wood, E. Kazyak, W.S. Lepage, A.L. Davis, A.J. Sanchez, N.P. Dasgupta, Dead lithium: Mass transport effects on voltage, capacity, and failure of lithium metal anodes, J. Mater. Chem. A. 5 (2017) 11671–11681. https://doi.org/10.1039/c7ta00371d.
[111] D. Lv, Y. Shao, T. Lozano, W.D. Bennett, G.L. Graff, B. Polzin, J. Zhang, M.H. Engelhard, N.T. Saenz, W.A. Henderson, P. Bhattacharya, J. Liu, J. Xiao, Failure mechanism for fast-charged lithium metal batteries with liquid electrolytes, Adv. Energy Mater. 5 (2015). https://doi.org/10.1002/aenm.201400993.
[112] S. Nanda, A. Gupta, A. Manthiram, Anode-Free Full Cells: A Pathway to High-Energy Density Lithium-Metal Batteries, Adv. Energy Mater. 11 (2021) 1–18. https://doi.org/10.1002/aenm.202000804.
[113] J. Chen, J. Xiang, X. Chen, L. Yuan, Z. Li, Y. Huang, Li2S-based anode-free full

batteries with modified Cu current collector, Energy Storage Mater. 30 (2020) 179–186. https://doi.org/10.1016/j.ensm.2020.05.009.
[114] W. Zhu, A. Paolella, C.S. Kim, D. Liu, Z. Feng, C. Gagnon, J. Trottier, A. Vijh, A. Guerfi, A. Mauger, C.M. Julien, M. Armand, K. Zaghib, Investigation of the reaction mechanism of lithium sulfur batteries in different electrolyte systems by: In situ Raman spectroscopy and in situ X-ray diffraction, Sustain. Energy Fuels. 1 (2017) 737–747. https://doi.org/10.1039/c6se00104a.
[115] D.A. Shapiro, Y.S. Yu, T. Tyliszczak, J. Cabana, R. Celestre, W. Chao, K. Kaznatcheev, A.L.D. Kilcoyne, F. Maia, S. Marchesini, Y.S. Meng, T. Warwick, L.L. Yang, H.A. Padmore, Chemical composition mapping with nanometre resolution by soft X-ray microscopy, Nat. Photonics. 8 (2014) 765–769. https://doi.org/10.1038/nphoton.2014.207.
[116] C. Tan, T.M.M. Heenan, R.F. Ziesche, S.R. Daemi, J. Hack, M. Maier, S. Marathe, C. Rau, D.J.L. Brett, P.R. Shearing, Four-Dimensional Studies of Morphology Evolution in Lithium-Sulfur Batteries, ACS Appl. Energy Mater. 1 (2018) 5090–5100. https://doi.org/10.1021/acsaem.8b01148.
[117] O.O. Taiwo, M. Loveridge, S.D. Beattie, D.P. Finegan, R. Bhagat, D.J.L. Brett, P.R. Shearing, Investigation of cycling-induced microstructural degradation in silicon-based electrodes in lithium-ion batteries using X-ray nanotomography, Electrochim. Acta. 253 (2017) 85–92. https://doi.org/10.1016/j.electacta.2017.08.161.
[118] S.H. Yu, X. Huang, K. Schwarz, R. Huang, T.A. Arias, J.D. Brock, H.D. Abruña, Direct visualization of sulfur cathodes: New insights into Li-S batteries via operando X-ray based methods, Energy Environ. Sci. 11 (2018) 202–210. https://doi.org/10.1039/c7ee02874a.
[119] C. Tan, M.D.R. Kok, S.R. Daemi, D.J.L. Brett, P.R. Shearing, Three-dimensional image based modelling of transport parameters in lithium-sulfur batteries, Phys. Chem. Chem. Phys. 21 (2019) 4145–4154. https://doi.org/10.1039/c8cp04763d.
[120] F. Sun, K. Dong, M. Osenberg, A. Hilger, S. Risse, Y. Lu, P.H. Kamm, M. Klaus, H. Markötter, F. García-Moreno, T. Arlt, I. Manke, Visualizing the morphological and compositional evolution of the interface of InLi-anode thio-LISION electrolyte in an all-solid-state Li-S cell by: In operando synchrotron X-ray tomography and energy dispersive diffraction, J. Mater. Chem. A. 6 (2018) 22489–22496. https://doi.org/10.1039/c8ta08821g.
[121] L. Zielke, C. Barchasz, S. Walu, F. Alloin, J.C. Leprêtre, A. Spettl, V. Schmidt, A. Hilger, I. Manke, J. Banhart, R. Zengerle, S. Thiele, Degradation of Li/S battery electrodes on 3D current collectors studied using x-ray phase contrast tomography, Sci. Rep. 5 (2015) 1–12. https://doi.org/10.1038/srep10921.
[122] F. Sun, M. Osenberg, K. Dong, D. Zhou, A. Hilger, C.J. Jafta, S. Risse, Y. Lu, H. Markötter, I. Manke, Correlating Morphological Evolution of Li Electrodes with Degrading Electrochemical Performance of Li/LiCoO2 and Li/S Battery Systems: Investigated by Synchrotron X-ray Phase Contrast Tomography, ACS Energy Lett. 3 (2018) 356–365. https://doi.org/10.1021/acsenergylett.7b01254.
[123] A. Yermukhambetova, C. Tan, S.R. Daemi, Z. Bakenov, J.A. Darr, D.J.L. Brett, P.R. Shearing, Exploring 3D microstructural evolution in Li-Sulfur battery electrodes using in-situ X-ray tomography, Sci. Rep. 6 (2016) 1–9. https://doi.org/10.1038/srep35291.
[124] J. Nelson, S. Misra, Y. Yang, A. Jackson, Y. Liu, H. Wang, H. Dai, J.C. Andrews, Y. Cui, M.F. Toney, In operando X-ray diffraction and transmission X-ray microscopy of lithium sulfur batteries, J. Am. Chem. Soc. 134 (2012) 6337–6343. https://doi.org/10.1021/ja2121926.
[125] J.-T. Yeon, J.-Y. Jang, J.-G. Han, J. Cho, K.T. Lee, N.-S. Choi, Raman Spectroscopic

and X-ray Diffraction Studies of Sulfur Composite Electrodes during Discharge and Charge, J. Electrochem. Soc. 159 (2012) A1308–A1314. https://doi.org/10.1149/2.080208jes.
[126] S. Walus, C. Barchasz, J.F. Colin, J.F. Martin, E. Elkaïm, J.C. Leprêtre, F. Alloin, New insight into the working mechanism of lithium–sulfur batteries: In situ and operando X-ray diffraction characterization, Chem. Commun. 49 (2013) 7899–7901. https://doi.org/10.1039/c3cc43766c.
[127] J. Hannauer, J. Scheers, J. Fullenwarth, B. Fraisse, L. Stievano, P. Johansson, The Quest for Polysulfides in Lithium-Sulfur Battery Electrolytes: An Operando Confocal Raman Spectroscopy Study, ChemPhysChem. 16 (2015) 2755–2759. https://doi.org/10.1002/cphc.201500448.
[128] M. Hagen, P. Schiffels, M. Hammer, S. Dörfler, J. Tübke, M.J. Hoffmann, H. Althues, S. Kaskel, In-Situ Raman Investigation of Polysulfide Formation in Li-S Cells, J. Electrochem. Soc. 160 (2013) A1205–A1214. https://doi.org/10.1149/2.045308jes.
[129] H.L. Wu, L.A. Huff, A.A. Gewirth, In situ raman spectroscopy of sulfur speciation in lithium-sulfur batteries, ACS Appl. Mater. Interfaces. 7 (2015) 1709–1719. https://doi.org/10.1021/am5072942.
[130] R. Bouchal, A. Boulaoued, P. Johansson, Monitoring Polysulfide Solubility and Diffusion in Fluorinated Ether-Based Electrolytes by Operando Raman Spectroscopy, Batter. Supercaps. 3 (2020) 397–401. https://doi.org/10.1002/batt.201900188.
[131] D. Blanchard, M. Slagter, In operando Raman and optical study of lithium polysulfides dissolution in lithium–sulfur cells with carrageenan binder, JPhys Energy. 3 (2021). https://doi.org/10.1088/2515-7655/ac0b37.
[132] M.U.M. Patel, R. Demir-Cakan, M. Morcrette, J.M. Tarascon, M. Gaberscek, R. Dominko, Li-S battery analyzed by UV/vis in operando mode, ChemSusChem. 6 (2013) 1177–1181. https://doi.org/10.1002/cssc.201300142.
[133] N.A. Cañas, D.N. Fronczek, N. Wagner, A. Latz, K.A. Friedrich, Experimental and theoretical analysis of products and reaction intermediates of lithium-sulfur batteries, J. Phys. Chem. C. 118 (2014) 12106–12114. https://doi.org/10.1021/jp5013208.
[134] M. Cuisinier, P.E. Cabelguen, S. Evers, G. He, M. Kolbeck, A. Garsuch, T. Bolin, M. Balasubramanian, L.F. Nazar, Sulfur speciation in Li-S batteries determined by operando X-ray absorption spectroscopy, J. Phys. Chem. Lett. 4 (2013) 3227–3232. https://doi.org/10.1021/jz401763d.
[135] Q. Wang, J. Zheng, E. Walter, H. Pan, D. Lv, P. Zuo, H. Chen, Z.D. Deng, B.Y. Liaw, X. Yu, X. Yang, J.-G. Zhang, J. Liu, J. Xiao, Direct Observation of Sulfur Radicals as Reaction Media in Lithium Sulfur Batteries, J. Electrochem. Soc. 162 (2015) A474–A478. https://doi.org/10.1149/2.0851503jes.
[136] S.S. Zhang, Improved cyclability of liquid electrolyte lithium/sulfur batteries by optimizing electrolyte/sulfur ratio, Energies. 5 (2012) 5190–5197. https://doi.org/10.3390/en5125190.
[137] D. Atkins, E. Capria, K. Edström, T. Famprikis, A. Grimaud, Q. Jacquet, M. Johnson, A. Matic, P. Norby, H. Reichert, J.-P. Rueff, C. Villevieille, M. Wagemaker, S. Lyonnard, Accelerating battery characterization using neutron & synchrotron techniques: towards a multi-modal and multiscale standardized experimental workflow, Adv. Energ. Mater. Submitt. (2021) 2102694. https://doi.org/10.1002/aenm.202102694.
[138] X. Wang, M. Zhang, J. Alvarado, S. Wang, M. Sina, B. Lu, J. Bouwer, W. Xu, J. Xiao, J.G. Zhang, J. Liu, Y.S. Meng, New Insights on the Structure of Electrochemically Deposited Lithium Metal and Its Solid Electrolyte Interphases via Cryogenic TEM, Nano Lett. 17 (2017) 7606–7612. https://doi.org/10.1021/acs.nanolett.7b03606.

[139] X. Wang, G. Pawar, Y. Li, X. Ren, M. Zhang, B. Lu, A. Banerjee, P. Liu, E.J. Dufek, J.G. Zhang, J. Xiao, J. Liu, Y.S. Meng, B. Liaw, Glassy Li metal anode for high-performance rechargeable Li batteries, Nat. Mater. 19 (2020) 1339–1345. https://doi.org/10.1038/s41563-020-0729-1.
[140] Y. Li, Y. Li, A. Pei, K. Yan, Y. Sun, C.L. Wu, L.M. Joubert, R. Chin, A.L. Koh, Y. Yu, J. Perrino, B. Butz, S. Chu, Y. Cui, Atomic structure of sensitive battery materials and interfaces revealed by cryo–electron microscopy, Science (80-.). 358 (2017) 506–510. https://doi.org/10.1126/science.aam6014.
[141] K.N. Wood, E. Kazyak, A.F. Chadwick, K.H. Chen, J.G. Zhang, K. Thornton, N.P. Dasgupta, Dendrites and pits: Untangling the complex behavior of lithium metal anodes through operando video microscopy, ACS Cent. Sci. 2 (2016) 790–801. https://doi.org/10.1021/acscentsci.6b00260.
[142] J. Tan, D. Liu, X. Xu, L. Mai, In situ/operando characterization techniques for rechargeable lithium-sulfur batteries: A review, Nanoscale. 9 (2017) 19001–19016. https://doi.org/10.1039/c7nr06819k.
[143] C. V. Raman, K.S. Krishnan, A new type of secondary radiation [11], Nature. 121 (1928) 501–502. https://doi.org/10.1038/121501c0.
[144] P. Larkin, Infrared and Raman Spectroscopy: Principles and Spectral Interpretation, Elsilvier, Amsterdam, 2011.
[145] NobelPrize.org, The Nobel Prize in Physiology or Medicine 1979, Nobel Prize Outreach AB. (2021). https://www.nobelprize.org/prizes/medicine/1979/summary/ (accessed December 3, 2021).
[146] M. Ebner, F. Marone, M. Stampanoni, V. Wood, Visualization and quantification of electrochemical and mechanical degradation in li ion batteries, Science (80-.). 342 (2013) 716–720. https://doi.org/10.1126/science.1241882.
[147] F. Sun, R. Gao, D. Zhou, M. Osenberg, K. Dong, N. Kardjilov, A. Hilger, H. Markötter, P.M. Bieker, X. Liu, I. Manke, Revealing Hidden Facts of Li Anode in Cycled Lithium-Oxygen Batteries through X-ray and Neutron Tomography, ACS Energy Lett. 4 (2019) 306–316. https://doi.org/10.1021/acsenergylett.8b02242.
[148] M. Stampanoni, G. Borchert, P. Wyss, R. Abela, B. Patterson, S. Hunt, D. Vermeulen, P. Rüegsegger, High resolution X-ray detector for synchrotron-based microtomography, Nucl. Instruments Methods Phys. Res. Sect. A Accel. Spectrometers, Detect. Assoc. Equip. 491 (2002) 291–301. https://doi.org/10.1016/S0168-9002(02)01167-1.
[149] P.C.J. Donoghue, S. Bengtson, X.P. Dong, N.J. Gostling, T. Huldtgren, J.A. Cunningham, C. Yin, Z. Yue, F. Peng, M. Stampanoni, Synchrotron X-ray tomographic microscopy of fossil embryos, Nature. 442 (2006) 680–683. https://doi.org/10.1038/nature04890.
[150] L. Grodzins, Optimum energies for x-ray transmission tomography of small samples. Applications of synchrotron radiation to computerized tomography I, Nucl. Instruments Methods Phys. Res. 206 (1983) 541–545. https://doi.org/10.1016/0167-5087(83)90393-9.
[151] P. Wilmott, An Introduction to Synchrotron Radiation: Techniques and Applications, Wiley Blackwell, 2011. https://doi.org/10.1002/9781119970958.
[152] R. Schofield, L. King, U. Tayal, I. Castellano, J. Stirrup, F. Pontana, J. Earls, E. Nicol, Image reconstruction: Part 1 – understanding filtered back projection, noise and image acquisition, J. Cardiovasc. Comput. Tomogr. 14 (2020) 219–225. https://doi.org/10.1016/j.jcct.2019.04.008.
[153] F. Marone, M. Stampanoni, Regridding reconstruction algorithm for real-time tomographic imaging, J. Synchrotron Radiat. 19 (2012) 1029–1037.

https://doi.org/10.1107/S0909049512032864.
[154] D. Paganin, S.C. Mayo, T.E. Gureyev, P.R. Miller, S.W. Wilkins, Simultaneous phase and amplitude extraction from a single defocused image of a homogeneous object, J. Microsc. 206 (2002) 33–40. https://doi.org/10.1046/j.1365-2818.2002.01010.x.
[155] S. Migge, G. Sandmann, D. Rahner, H. Dietz, W. Plieth, Studying lithium intercalation into graphite particles via in situ Raman spectroscopy and confocal microscopy, J. Solid State Electrochem. 9 (2005) 132–137. https://doi.org/10.1007/s10008-004-0563-4.
[156] A. Ramos, I. Cameán, N. Cuesta, C. Antuña, A.B. García, Expanded graphitic materials prepared from micro- and nanometric precursors as anodes for sodium-ion batteries, Electrochim. Acta. 187 (2016) 496–507. https://doi.org/10.1016/j.electacta.2015.11.078.
[157] S. Xiong, Y. Liu, P. Jankowski, Q. Liu, F. Nitze, K. Xie, J. Song, A. Matic, Design of a Multifunctional Interlayer for NASCION-Based Solid-State Li Metal Batteries, Adv. Funct. Mater. 30 (2020). https://doi.org/10.1002/adfm.202001444.
[158] M.H. Ryou, Y.M. Lee, Y. Lee, M. Winter, P. Bieker, Mechanical surface modification of lithium metal: Towards improved Li metal anode performance by directed Li plating, Adv. Funct. Mater. 25 (2015) 834–841. https://doi.org/10.1002/adfm.201402953.